MICROSTRUCTURE AND SUPERELASTIC RESPONSE OF IRON-BASED SHAPE MEMORY ALLOYS

A Dissertation

by

LI-WEI TSENG

Submitted to the Office of Graduate and Professional Studies of
Texas A&M University
in partial fulfillment of the requirements for the degree of

DOCTOR OF PHILOSOPHY

Chair of Committee,	Ibrahim Karaman
Committee Members,	Tahir Cagin
	Karl. T. Hartwig
	Xinghang Zhang
Head of Department,	Andreas Polycarpou

May 2015

Major Subject: Mechanical Engineering

ABSTRACT

$Fe_{43.5}Mn_{34}Al_{15}Ni_{7.5}$ shape memory alloys have attracted attention as potential superelasticity alloys in server environments, capable of exhibiting good superelastic behavior with up to 5% recoverable strain over a wide temperature range from -196°C to 240°C. The objective of this work is to investigate the effects of martensite variants, aging heat treatment, crystal orientations and grain size on the superelastic properties.

Although the theoretical transformation strain of single crystal with the <100> orientation in tension (26.5%) is higher than it is in compression (10.5%), the compression sample shows a better recoverable strain than that in the tension sample from the experimental results. The differences in reversibility and the shape of the stress-strain curves under tension and compression are attributed to the lower number of martensite variants activated under tension as compared to compression.

The effect of aging has profound influences on the size and volume fraction of precipitates, transformation temperatures, stress-temperature phase diagram, recoverable strain and stress hysteresis. Increasing the aging times improves the superelastic strain in compression and decreases it in tension. The reason for these is related to the selection of martensite variants.

The crystal orientations affect the superelastic properties such as the stress-temperature phase diagram and transformation strain. The differences in the slope of the stress-temperature curves and critical stress in different orientation are attributed to the

transformation strain and resolved shear stress factors, respectively. Aging heat treatment decreases the orientation effect on slope of stress-temperature curve.

The sheet is brittle (high hardness values) after being hot-rolled which causes to appear after the cold-rolled experiment. The hot-rolled sheet was annealing at 900°C for 1 hour to obtain two phases (bcc+fcc) and ductility (small hardness values). Therefore, cold-rolling of the annealing sheet is practical up to 76%. The large grain size can be obtained by repetition of the heat treatment. Increasing the grain sizes improves the superelastic strain due to reduction of grain boundary constraints.

DEDICATION

To my parents and sister who have given tremendous support and encouragement at all times

ACKNOWLEDGEMENTS

I would first like to express my respect and gratitude to my graduate advisor Prof. Ibrahim Karaman for his support and giving me the chance to pursue a doctoral degree. During my Ph.D. education, he has been a role model for me with his unparalleled discipline, perseverance and hard work in every aspect of life and his great enthusiasm for research. His incredible vision with research gave me the necessary direction for my research. Moreover, he has provided the best equipment in the lab for us to complete all the experimental works.

I would also like to thank Prof. Tahir Cagin, Prof. Karl. T. Hartwig and Prof. Xinghang Zhang for serving in my committee and offering their valuable suggestions for my study.

I would like to thank Prof. Yuriy Chumlyakov for creating the iron-based single crystals for my research and giving me suggestions and knowledgement during the discussions. Dr. Zhipping Luo and Dr. Shujuan Wang are acknowledged for their great jobs in taking the transmission electron microscope images and diffraction pattern of FeMnAlNi samples. Dr. Ray Guilemette helped me on the microstructural analysis of the FeMnAlNi samples. Prof. Geroge B. Thompson and his student Billy Chad Hornbuckle are acknowledged for their atom probe tomography analysis. Thank you to the turkish visiting professors Prof. Mehmet Kaya and Prof. Eskil Murat for helping me in the heat treatment experiment and thermomechanical processing.

I would like to thank all the colleagues I worked with together, who made my stay in College Station a memorable one: Ji Ma, James A. Monroe, Ebubekir Dogan, Nick Bruno, Nick Barta, Hande Ozcan, Hu Liangfa, Ankush Dilip Kothalkar, Alper Evirgen, Brian E. Franco, Matthew Vaughan, Ceylan Hayrettin, and Taymaz Jo. Special thanks to Dr. Ma for always helping me correct my papers and givinge me valuable suggestions about my dissertation. Hande Ozcan will continue the iron-based wire studies and generate good methods for solving the heat treatment problems and improving the mechanical properties.

Last but not least, I am gratefully thankful to my father, mother and sister, Pao-Ming Tseng, Hai-Fen Chu and Li-Chia Tseng for their continuous support and love. They sacrificed a lot for me during my Ph.D. study. When I felt lonely and frustrated during my Ph.D. study, they encouraged me to overcome the emotional situation and obstacles. Their strong motivation and endless trust are the reason I overcame the challenge. Without their support and encouragement, I would not have successful finished this degree. No words can fully express my gratitude for my parents and my sister.

Finally, thank you all for above support.

NOMENCLATURE

AC	Air Cooling
AHT	Annealing Heat Treatment
APT	Atom Probe Tomography
BSE	Backscattered Electron
CVP	Correspondent Variant Pair
EBSD	Electron Backscatter Diffraction
EDM	Electrical Discharge Machining
GP	Gain Boundary Allotriomorphs
HV	Vickers Hardness
IP	Intragranular Phase
LEAP	Local Electrode Atom Probe
MTS	Material Test System
ND	Normal Direction
OM	Optical Microscopy
PHT	Precipitation Heat Treatment
RD	Rolling Direction
SAED	Selected-Area Electron Diffraction
SHT	Solution Heat Treatment
SE	Superelasticity
SEM	Scanning Electron Microscopy

SMAs	Shape Memory Alloys
SME	Shape Memory Effect
SQUID	Superconducting Quantum Interference Device
TD	Transverse Direction
TEM	Transmission Electron Microscopy
WDS	Wavelength-Dispersive Spectroscopy
WS	Widmanstatten Side Plates
XRD	X-Ray Diffraction

TABLE OF CONTENTS

Page

CHAPTER

CHAPTER

LIST OF FIGURES

Page

LIST OF TABLES

Page

CHAPTER I

INTRODUCTION

This chapter introduces the need and motivation for the development of iron-based shape memory alloys (SMAs) to be used in industrial applications. $Fe_{43.5}Mn_{34}Al_{15}Ni_{7.5}$ shape memory alloys have attracted attention as potential superelasticity alloys capable of operating at a wide temperature range from -196°C to 240°C. Since the new alloys were discovered in 2011, there have not been any studies of the effects of martensite morphology, aging heat treatment and orientation on superelasticity. At the end of this chapter, the present studies are outlined to meet the objectives.

1.1 Motivation

One unique chrarcteristic of the shape memory alloys (SMAs) is the thermoelastic martensitic phase transformation. The martensitic transformation is the diffusionless solid to solid phase transformation [1]. The shape memory effect (SME) and superelasticity (SE) are the result of martensitic transformation. The shape memory effect is when the material is deformed, it could recover to its original shape after heating the material above the transformation temperature. The superelasticity is an isothermal phenomenon where the material is deformed during loading and can recover its predeformed shape after unloading [1-3]. Both shape memory effect and superelasticity allow the SMAs to recover a large amount of strains after deformation. NiTi-based SMAs were discovered in the 1960s [4] and Frederick Wang and William

Buehler discovered the shape memory effect and superelasticity in 1963 [4,5]. Since the discovery of the superelastic properties in NiTi SMAs, NiTi SMAs have been used in different industrial fields such as aerospace, civil engineering and automotive industries due to their excellent 7% recoverable strain in tension. However, the material cost and processing cost are expensive and difficult in cold work [1,15]. The drawbacks of NiTi SMAs have impeded their uses in further industrial applications. Because of the low material cost, high ductility and better workability in comparison with those of the NiTi alloys, iron-based SMAs have attracted attentions and many researchers have been made to achieve the superelasticity in iron-based alloys system.

Iron-based SMAs have been studied since the 1970s. The alloys such as FePt [16], FePd [17], FeNiCoTi [18] and FeMnSi [19-21] exhibit only shape memory behavior. Unfortunately, most iron-based SMAs exhibit poor superelastic behavior or small recoverable strain due to their non-thermoelastic martensitic transformation (FeMnAl [22]) and large temperature and stress hysteresis (FeMnSi [19] and FeNiCoTi [23]). In 2010 and 2011, Tanaka and Omori et al [24-25] succeeded in obtaining the large superelastic strain in a pair of newly discoveried iron-based SMAs: $Fe_{40.95}Ni_{28}Co_{17}Al_{11.5}Ta_{2.5}B_{0.05}$ and $Fe_{43.5}Mn_{34}Al_{15}Ni_{7.5}$. The former SMA shows 13.5% superelastic strain and high strength of over 1 GPa [24] while the latter shows 5% superelastic strain [25]. The most interesting characteristic of $Fe_{43.5}Mn_{34}Al_{15}Ni_{7.5}$ SMAs is that they possess the small temperature dependence of the critical stress in a wide temperautre range. For $Fe_{43.5}Mn_{34}Al_{15}Ni_{7.5}$ polycrystalline aged at 200°C for 24 hours, the slope of the stress-temperature curve is about 0.53 Mpa/°C over a large temperature

range from -196°C to 240°C [25]. This means the material is able to have the superealsticity in a wide temperature range. This property is attractive for automobile and aerospace, which require the SMAs operation at large temperature range from -100°C to 150°C [25]. In contrast to FeMnAlNi SMAs, the slope of the stress-temperature curve in conventional NiTi SMAs is about 6MPa/°C and results in limiting their use in the temperature window from -20°C to 80°C [1,25].

This study is first focused on the FeMnAlNi single crystals, which have the strong advantage that the deformation mechanisms is related to one specific orientation without considering effect of orientations and grain size in polycrystals. The second study is focused on grain size effect in the polycrystals.

The motivation and background for the single crystal and polycrystals studies are listed as follows:

1. In iron-based SMAs such as FeNiCoTi and FeNiCoAlTaB, the maximum theoretical transformation strain is in the [100] orientation in both tension and compression [23,24]. Tanaka et al. [24] reported that the FeNiCoAlTaB polycrystals with the strong texture in the [100] orientation show the perfect superelasticity at room temperature. In FeMnAlNi SMAs, the highest theoretical transformation strain is in the [100] orientation under both tension (26.5%) and compression (10.5%). Therefore, it is important to study the [100] orientation to understand the superelastic properties in FeMnAlNi SMAs. Since the transformation strain values in tension is almost two times than in compression,

the [100] orientation should show pronounced tension-compression asymmetry in the superelastic responses.

2. In the SMAs, it has been proven that the precipitation is likely not only limited to strengthen the austenite matrix but also a very powerful tool for altering the physical and mechanical properties. In NiTi SMAs, the precipitates are influenced by transformation strain, stress and thermal hysteresis, tension-compression asymmetry, superelastic strain, recoverability, martensite morphology, the composition of the matrix, transformation temperature and hardness [26-36]. In the iron-based SMAs, the precipitates also serve important roles in the superelastic and shape memory properties. Studies on FeNiCoTi SMAs by Sehitoglu *et al*. [37,38] show that increasing aging times reduces the transformation temperature, enlarges temperature hysteresis and increases the recoverable strain in both the superelastic and shape memory experiments. Furthermore, Ma *et al*. [39,40] investigated the effect of aging heat treatment on superelasticity in the FeNiCoAlTa single crystal and reported that increasing the aging times, which increased the size of precipitates but not the volume fraction, increased transformation temperature and intensified the tension-compression asymmetry. Despite the important influences of precipitates on the microstructure and superelastic characteristics, there has been no previous study on this topic in $Fe_{43.5}Mn_{34}Al_{15}Ni_{7.5}$ single crystals. It is expected that aging heat treatment will alter the microstructure (precipitate size and volume fraction), transformation temperature and superelasticity of FeMnAlNi alloys.

3. Crystallographic texture is one of the important factors to influence the superelastic response of the SMAs. Studies on NiTi single crystals by Gall et al. [41-44] showed that the superelasticity of NiTi SMAs was dependent on the applied stress state and crystallographic orientations. The [100] orientation demonstrated the smaller transformation strain and higher critical stress than those in the [111] orientation in tension test. The [111] orientation in tension test is characterized as soft direction due to having a large transformation strain and low critical stress. However, the superelastic responses were reversed under the compression test, i.e. the large transformation strain and low critical stress were in the [100] orientation instead of [111] orientation [41-44]. Moreover, aged NiTi single crystals show a decrease in the orientation dependence of the stress-temperature slope and critical stress for stress-induced martensitic transformation [45-47]. Therefore, it is important to characterize the FeMnAlNi single crystals in different orientations to understand the orientation dependence of the stress-temperature phase diagram, critical stress and transformation strain. This understanding will be beneficial for prediction of the superelastic behavior in the texture polycrystals.
4. The superelastic behavior in polycrystals is influenced by grain size. In NiTi SMAs, Saburi *et al.* [48] reported that small grain size improves the superelastic behavior because grain boundaries assist the back transformation. Ti-50.5%Ni alloys show the full recoverable strain in superelastic tension test with the 50μm grain size. When the grain size increases to 1 mm, the recoverable strain

decreases, 85% recovery. In 2013, Aslan Ahadi et al [49,50] investigated the effect of grain size in the nanostructure polycrystalline of NiTi SMAs. They reported that reduction of grain size decreases the superelastic recoverable strain, critical stress and the slope of stress-temperature curve. The reason is that large grain size provides more interfacial energy and leads to the reversible martensitic transformation and breakdown of the stress-temperature slope [49].

In Cu-based SMAs, superelastic behavior is strongly influenced by the grain size or grain size relative to the thickness of the sheet or wire [51-53]. Kainuman et al [54,55] and Sutou et al [56-58] investigated the effect of grain size on the CuAlMn alloy sheet and reported that the excellent recoverable strain, ductility and low critical stress can be obtained by controlling the grain size. An addition of a small amount of B or Co into the alloys is used for the grain size refinement. The huge grains are achieved by repetition of the heat treatment cyclic and followed by air cooling to the room temperature. The superelastic characteristics such as stress hysteresis, critical stress and superelastic strain and fracture stress were strongly influenced by grain size. Large grain size decreases the critical stress and improves the ductility and superelastic strain.

Stian et al [59] studied the superelasticity and fatigue in the oligocrystals CuAlNi and CuZnAl shape memory alloy wires. An o oligocrystals structure is defined as the total surface area of wire is greater than the total grain boundary areas, which is also called bamboo structure. Large recoverable strain with 7% and perfect fatigue life up to 10000 cycles can obtain in the bamboo type microwire. The

reason is the large grain size decreases the numbers of small grains or triple junctions, which causes the premature fracture.

In iron-based SMAs, FeNiCoAlTaB polycrystals show over 13% recoverable strain with the large grain size, about 400μm [24]. In FeMnAlN polycrystals sheet and wire studies, 5% recoverable strain was obtained in the large grain size about 3.5 mm in polycrystalline sheet [25] and 433μm in the polycrystalline wire [60]. In Omori et al. studies [24], they did not investigate the grain size dependence of superelasticity (stress hysteresis, superelastic strain, critical stress and elongation) in the polycrystals. Therefore, we will investigate the grain size dependence of the stress-strain characteristics of FeMnAlNi polycrystals in tension.

1.2 Objectives

Based on the discussion in section 1.1, the objectives of FeMnAlNi shape memory alloys can summary as follow:

(1) Characterization of the superelasticity and precipitate structure in $Fe_{43.5}Mn_{34}Al_{15}Ni_{7.5}$ oriented [100] single crystal aged at 200°C under both tension and compression.

This study is focused on the [100] orientation due to having the maximum transformation strain in both tension and compression. It is imperative to study the single crystalline properties in order to understand the superelastic response along the [100] orientation and reveal the tension-compression asymmetry and limitations of the present alloy in terms of transformation strain so as to provide further insights for polycrystalline studies. We have conducted a thermo-mechanical experiment under both tension and compression. A detailed electron microscopy investigation was performed to find out the precipitate and martensite structures and the governing mechanisms responsible for the differences in the stress-strain responses of tension and compression samples. The present study also aims at better understanding the characteristics of stress-temperature phase diagrams and determining the maximum recoverable strain levels in precipitation hardened FeMnAlNi single crystals.

(2) Investigate the effect of aging on the microstructure and superelasticity in $Fe_{43.5}Mn_{34}Al_{15}Ni_{7.5}$ oriented [100] single crystals under both tension and compression

The objective of this study will aim to present in detail about the effect of aging on the size, composition and volume fraction of precipitates and in turn, the effect of precipitate size and volume fraction on the transformation temperature, superelastic characteristics such as stress hysteresis, superelastic strain, critical stress for stress-induced martensitic transformation, and stress-temperature slope. Electron microscopy and atom probe tomography investigation was performed to find out the size, volume fraction and composition of precipitates. This study also aims to find the good aging temperature and times for showing superelasticity at room temperature in both tension and compression.

(3) Investigate the orientation dependence on the stress-temperature phase diagram and recoverable strain in $Fe_{43.5}Mn_{34}Al_{15}Ni_{7.5}$ single crystals under both tension and compression

In this work, the different crystallographic orientations are chosen to compare the different positions in the stereographic triangle: [100], [111] and [123] orientations. The superelastic characteristics of $Fe_{43.5}Mn_{34}Al_{15}Ni_{7.5}$ single crystal in the [100] and [111] orientations are expected to be drastically different under compression and tension because the maximum transformation strains different significantly for the soft [100] orientation compared to the hard [111] orientation. The [123] orientation is selected due to multiple variant activate. This purpose of this study is to better understanding the orientation dependence of transformation strain and critical stress, the stress-temperature phase diagram.

(4) Investigate the effect of microstructure on the superelasticity in textured $Fe_{43.5}Mn_{34}Al_{15}Ni_{7.5}$ polycrystals under tension.

The current work investigates the influence of grain size on superelastic properties. The different grain size can obtain by conducted heat treatments. The purpose of this investigation is to understand the evolution of grain size on superelastic properties such as superelastic strain, elongation and critical stress.

As a result, the outline dissertation is as follows:

Chapter II: The background of martensitic transformation and iron-based SMAs literature review.

Chapter III: Experimental methods to meet each part of the studies.

Chapter IV: Investigate the crystal structure of precipitates and superelastic response in $Fe_{43.5}Mn_{34}Al_{15}Ni_{7.5}$ single crystals oriented along the [100] direction in both tension and compression. The main study is to link the martensite morphology and tension-compression asymmetry in the superelasticity.

Chapter V: Examine the effect of aging heat treatment (precipitation) on the microstructure (precipitate size, volume fraction and composition), transformation temperatures and superelasticity in $Fe_{43.5}Mn_{34}Al_{15}Ni_{7.5}$ single crystals oriented along the [100] orientation under both tension and compression.

Chapter VI: Investigate the effects of orientations ([100], [123] and [111]) on the superelasticity of $Fe_{43.5}Mn_{34}Al_{15}Ni_{7.5}$ single crystals under both compression and tension test. The main study examines the orientation dependence of the stress-temperature phase diagram and superelastic strain.

Chapter VII: Investigate the effect of microstructure (grain size) on superelasticity such as critical stress, stress hysteresis, recoverable strain, fracture stress and elongation in $Fe_{43.5}Mn_{34}Al_{15}Ni_{7.5}$ polycrystals sheet in tension test at room temperature. The chapter contains two part of work. First part of the work is the thermomechanical processing (hot-rolled and cold rolled) on the sheet. The second part of study investigates the thermomechanical heat treatment on the microstructure of polycrystals to link the relation between the microstructure (grain size) and mechanical properties (superelasticity).

Chapter VIII: Conclusions.

CHAPTER II

BACKGROUND

This chapter provides the thermodynamic background of the martensitic transformation and literature review of iron-based SMAs to the reader.

2.1 Thermodynamic Background of Martensitic Transformation

Since the superelasticity is related to thermoelastic martensitic transformations, the basic concept about thermoelastic martensitic transformation is introduced in this section before going into details about superelasticity. L. Kaufman and M. Cohen [61] were first observed the thermodynamic behaviors of martensitic transformation in AuCd and Fe-Ni alloys, shown in Figure 2.1. Kurdjumov et al. [62] were classified thermodynamic behaviors of martensitic transformation into two categories, thermoelastic and non-thermoelastic. In Figure 2.1, the transformation hysteresis or temperature hysteresis is about 15 K in the AuCd alloy. The small temperature hysteresis means the small driving force is required to the initial martensitic transformation and the interface between the austenite and martensite is mobile during the heating and cooling. As a result, the martensitic transformation is crystallographically reversible and frictional energy is low. This type of the thermodynamic behavior is called thermoelastic martensitic transformation. On the other hand, the large temperature hysteresis about 400K in FeNi alloys indicates large driving forces are required to overcome the immobile interface between the austenite and martensite. As a consequence, the large

friction energy between austenite and martensite interface causes the reverse transformation is irreversible [63,64]. This martensitic transformation is non-thermoelastic.

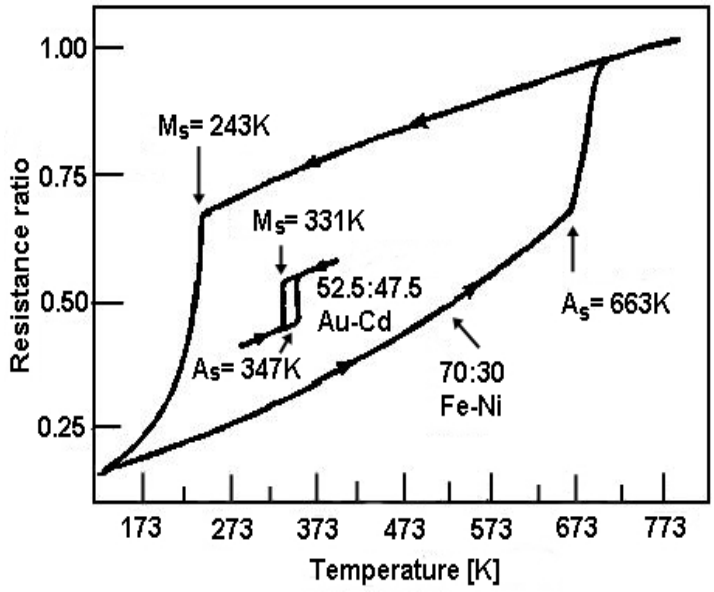

Figure 2.1 Electrical resistance change of Au–Cd and Fe–Ni alloys as a function of temperature during the heating and cooling cycle. The loops illustrate the temperature hysteresis of the martensitic transformation for the thermoelastic and non-thermoelastic, respectively [62].

In the thermodynamic aspect, the free energy curves of both austenite and martensite phases as a function of temperature are shown in Figure 2.2. G^m, G^p , T_0 and $\Delta G^{p\to m} = G^m - G^p$ are defined as Gibbs free energy of martensite phase, Gibbs free energy of parent phase, thermodynamic equilibrium temperature between martensite and parent phases and the driving force for the nucleation of martensite, respectively. A Gibbs free energy change of a system during the martensitic transformation was written as follows equation [65]

$$\Delta G = \Delta G_c + \Delta G_{nc} = \Delta G_c + \Delta G_s + \Delta G_e \tag{2.1}$$

where ΔG_c is a chemical free energy difference between parent and martensite phases, ΔG_{nc} is non-chemical energy and ΔG_e is the elastic energy. ΔG_s is a surface energy between the austenite and martensite phases. In general, the martensitic transformation will occur when $\Delta G_{nc} \geq G_c$. ΔT_s is the supercooling required to nucleate the martensite during the forward transformation, and superheating is required for reverse transformation. When the Gibbs energy of austenite and martensite phases is equal ($T_0^{\text{Austenite/Martensite}}$), the Curie temperature is approximately to $T_0^{\text{Austenite/Martensite}} \approx \left(T_{Ms} + T_{Af}\right)/2$.

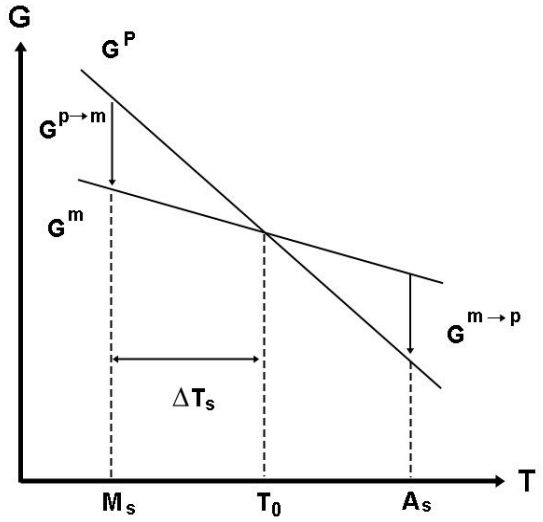

Figure 2.2 Schematic representation of free energy curves for both austenite and martensite phases, and the relation between the austenite start temperature and martensite start temperature [1].

2.2 Stress-Induced Martensitic Transformation and Superelastic Properties

The superelasticity is based on the stress-induced martensitic transformation during loading and the reverse transformation back to austenite upon unloading under constant temperature. The definition of superelastic characteristics such as σ_c, $\Delta\sigma$, ε_{irrec}, ε_{SE}, ε_e and $\varepsilon_{applied\ strain}$ was shown in the Figure 2.3. σ_c was the critical stress for stress-induced martensitic transformation and determined by the 0.2% strain offset method. $\Delta\sigma$ was the stress hysteresis and calculated as the difference between the loading and unloading lines. ε_{rec}, ε_{SE}, ε_e, ε_{irrec} and $\varepsilon_{applied}$ represent the recoverable strain, superelastic strain, elastic strain, irrecoverable strain and applied strain, respectively. $\varepsilon_{applied} = \varepsilon_{irrec} + \varepsilon_{SE} + \varepsilon_e$ and $\varepsilon_{rec} = \varepsilon_{SE} + \varepsilon_e$.

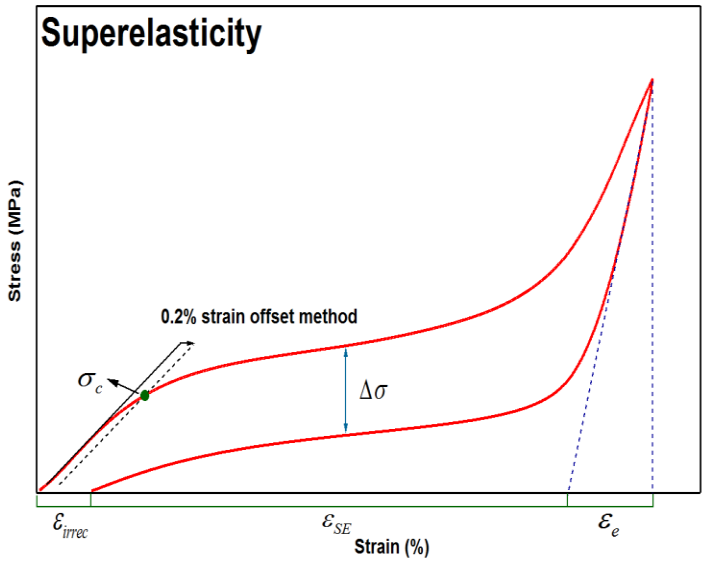

Fig. 2.3 Schematic illustration of the critical stress (σ_c), stress hysteresis ($\Delta\sigma$), irrecoverable strain (ε_{irrec}), superelastic strain (ε_{SE}) and elastic strain (ε_e) in superelastic test [2].

The required conditions for superelasticity and shape memory effect are demonstrated in Figure 2.4 [71]. In figure 2.4, a straight red line with positive slope represents the critical stress to stress induced martensitic transformation. The positive slope means the critical stress increases with increasing the test temperature. The straight back line with the negative slope represents the critical stress for slip. The relationship between temperature and critical stress appears to be linear which follow the Clausius-Clapeyron (CC) relation [72]. The relation is written as follow equation

$$\frac{d\sigma_c}{dT} = -\frac{\Delta S}{\varepsilon . \mathrm{V}_m} \qquad (2.2)$$

Where σ_c is the critical stress for stress-induced the martensitic transformation. T is the temperature, $d\sigma_c/dT$ denotes the slope of critical stress-temperature curve or Clausius-Clapeyron (CC) slope, the ΔS is the change of molar entropy associated with the forward transformation from the parent phase to martensite phase, ε is the transformation strain and V_m is the molar volume.

The test temperature are conducted relative to the A_f is important. When the test temperature is increased, the critical stress for stress induced martensitic transformation is also increased. The reason is that the austenite phase is more stable in higher temperature and thus the larger difference between A_f and test temperature, the large driving force is required to initial the stress induced martensitic transformation. When the deformation at temperature above the M_d temperature or the critical stress for stress induced martensitic transformation is higher than the critical stress for slip, the slip will occur first before critical stress for stress induced martensitic transformation. As a result,

the plastic deformation or dislocations will generate and suppress the superelasticity, which cause the large irrecoverable strain after unloading. If the stress is applied at temperature region between A_s and A_f, the martensite stay in the sample after deformation and can be recovered by heating the sample to the temperature above A_f, this behavior is called the shape memory effect.

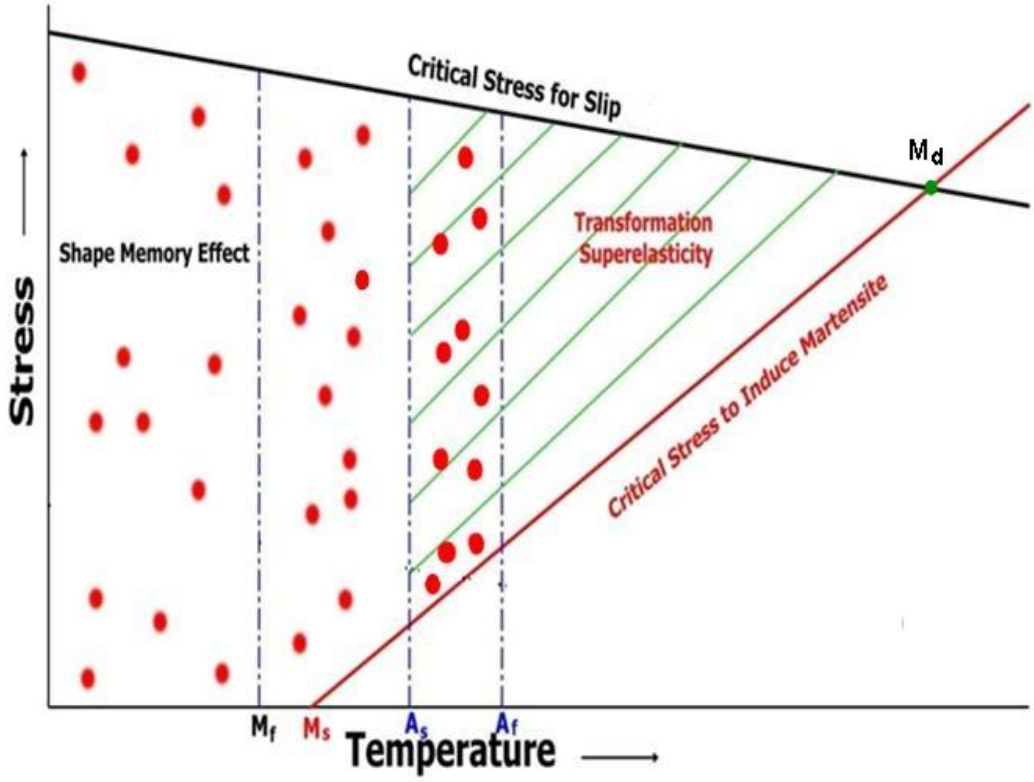

Figure 2.4 Schematic stress-temperature diagram representating the regions of superelasticity and shape memory effect [71].

2.3 Iron-Based Shape Memory Alloys Literature Review

This section will be summarized the crystal structure of austenite, martensite and precipitates for the iron-based SMAs. The literature review will focus on the development of the FeNiCoAlTaB (Fe-Ni based alloy system) [24] and FeMnAlNi (Fe-Mn based alloy system) [25].

2.3.1 Martensitic Transformation and Precipitate Structure

In Iron-based SMAs, the martensitic transformation generally can be divided into three groups according to their austenite and martensite crystal structures. First, the martensitic transformation is from the face-centered cubic (fcc) - austenite phase to hexagonal close-packed (hcp) - martensite phase. The fcc-hcp martensitic transformation can observe in FeMnSi [19-21]. Second, martensitic transformation is between fcc - austenite phase to body-centered tetragonal (bct) or body-centered cubic (bcc) - martensite phase, which can observe in FeNiCo alloy system [64]. Last, there is unusual martensitic transformation system reported in FeMnAl [22], FeMnGa [73] and FeMnAlNi [25] SMAs: they show the martensitic transformation between bcc - austenite phase and fcc - martensite phase.

The precipitates structure in the Fe-Ni based alloy systems (such as $Fe_{55.25}Ni_{28}Co_{12}Ti_{4.75}$ polycrystalline [23], $Fe_{41}Ni_{28}Co_{17}Al_{11.5}Ta_{2.5}$ single crystal [44,74-82], $Fe_{41}Ni_{28}Co_{17}Al_{11.5}Ti_{2.5}$ single crystal [83,84], $Fe_{41}Ni_{28}Co_{17}Al_{11.5}Nb_{2.5}$ single crystal [85,86], $Fe_{40.95}Ni_{28}Co_{17}Al_{11.5}Ta_{2.5}B_{0.05}$ polycrystal [24,87], $Fe_{40.95}Ni_{28}Co_{17}Al_{10.5}Nb_{2.5}B_{0.05}$ polycrystalline [88], and $Fe_{40.95}Ni_{28}Co_{17}Al_{10.5}Ti_{2.5}B_{0.05}$ polycrystalline [89]) is $L1_2$

structure. The chemical composition of precipitates is Ni_3Ti in FeNiCoTi and Ni_3Al in FeNiCoAlTaB [18,24]. In the Fe-Ni based alloy systems, the precipitates are fcc structure for FeMnSi SMAs. For FeMnAlNi alloy, the precipitate is the bcc (B2) structure and composition of precipitate is NiAl [25]. Table 2.1 summaries the crystal structure of austenite, martensite and precipitates in iron-based SMAs.

Table 2.1 Summary of the crystal structure of austenite, martensite and precipitate in iron-based SMAs

Alloys	**Chemical composition (at. %)**	**Crystal structure**		
		Austenite	**Martensite**	**Precipitate**
FeNi	$Fe_{55.25}Ni_{28}Co_{12}Ti_{4.75}$ $Fe_{41}Ni_{28}Co_{17}Al_{11.5}Ta_{2.5}$ $Fe_{41}Ni_{28}Co_{17}Al_{11.5}Ti_{2.5}$ $Fe_{41}Ni_{28}Co_{17}Al_{11.5}Nb_{2.5}$ $Fe_{40.95}Ni_{28}Co_{17}Al_{11.5}Nb_{2.5}B_{0.05}$ $Fe_{40.95}Ni_{28}Co_{17}Al_{11.5}Ta_{2.5}B_{0.05}$ $Fe_{40.95}Ni_{28}Co_{17}Al_{11.5}Ti_{2.5}B_{0.05}$	FCC	BCT	$L1_2$
FeMn	$Fe_{62}Mn_{32}Si_6$	FCC	HCP	FCC
	$Fe_{50}Mn_{22.5}Ga_{27.5}$	BCC	FCC	X
	$Fe_{49}Mn_{36}Al_{15}$			X
	$Fe_{43.5}Mn_{34}Al_{15}Ni_{7.5}$			BCC

2.3.2 Literature Review of $Fe_{40.95}Ni_{28}Co_{17}Al_{11.5}X_{2.5}B_{0.05}$ (X:Ta, Nb, Ti) Alloys Design

In the Fe-Ni-Al ternary alloys, the martensitic transformation is non-thermoelastic and results in no shape memory effect and superelasticity [90,91]. Co was first added to the Fe-Ni-Al alloy in order to strength the austenite matrix [92]. However, the martensitic transformation was still non-thermoelastic in the Fe-Ni-Co-Al quaternary system. Maki et al. [93] reported that the $Fe_{55.25}Ni_{28}Co_{12}Ti_{4.75}$ SMAs become thermoelastic martensitic transformation by replacing the Al to Ti element and

introducing the $L1_2$ precipitates into the austenite matrix by using aging heat treatment at 550°C or 600°C. Koval et al. [94] and Kokorin et al. [95] have studied the effect of aging on shape memory effect in FeNiCoTi SMAs and found that $L1_2$ precipitates strengthen the austenite and the tetragonal martensite and improve the recoverability of shape memory properties. Jost et al. [96,97] found the large temperature hysteresis around 120°C in FeNiCoTi SMAs. Based on their study, the range of aging heat treatment temperature is typically from 550°C to 700°C [94-97]. Sehitoglu et al. [23,37,38] investigated the aging heat treatment on the shape memory and superelastic properties. In their work, the precipitation provides the high strength in the austenite matrix, increases the slip resistance, decreases the thermal hysteresis and improves the recoverable strain in shape memory properties. However, the FeNiCoTi SMAs do not show the good superelastic behavior due to possess large stress hysteresis, hinders the occurrence for superelasticity [23].

In 2010, Tanaka et al. [24] reported the addition of Ta and B into FeNiCoAl alloys changes the martensitic transformation from non-thermoelastic to thermoelastic and resulting in showing superelasticity in $Fe_{40.95}Ni_{28}Co_{17}Al_{11.5}Ta_{2.5}B_{0.05}$ SMAs. The addition of Ta is used to increase the hardness (strength the austenite and tetragonal martensite phase), stabilize the $L1_2$ precipitates and increase the volume fraction of precipitates during the aging heat treatment [24]. Consequently, the $Fe_{41}Ni_{28}Co_{17}Al_{11.5}Ta_{2.5}$ alloy shows the thermoelastic martensitic transformation after precipitation. Ma et al. [39,40] have investigated the microstructure and superelastic responses in $Fe_{41}Ni_{28}Co_{17}Al_{11.5}Ta_{2.5}$ single crystals oriented along the [100] orientation.

The maximum 5% recoverable strain in tension and 4% in compression were obtained in the single crystals aged at 600°C for 90 hours in the superelastic test. The size of $L1_2$ precipitate in 600°C-90 hours aging condition is around 5 nm based on their TEM investigation. The superelastic behavior with 5-7% recoverable strain has also been reported in FeNiCoAlX (X = Ti and Nb) single crystals such as $Fe_{41}Ni_{28}Co_{17}Al_{11.5}Ti_{2.5}$ single crystals with the [100] orientation [83,84] and $Fe_{41}Ni_{28}Co_{17}Al_{11.5}Nb_{2.5}$ [85,86].

Although the $Fe_{41}Ni_{28}Co_{17}Al_{11.5}Ta_{2.5}$ single crystals show the perfect superelasticity, the FeNiCoAlTa polycrystals is extremely brittle due to formation of β precipitates along the grain boundaries during the aging heat treatment [88]. The previous investigation of single crystals (FeNiCoAlTa, FeNiCoAlTi FeNiCoAlNb) was not observed the β precipitates because of no grain boundaries in the single crystals. The addition small amount of B into FeNiCoAlTa alloy can drastically suppress the β precipitates at the grain boundary. Omori et al. [88] investigated the effect of the boron on microstructure and superelasticity in $Fe_{40.95}Ni_{28}Co_{17}Al_{11.5}Nb_{2.5}B_{0.05}$ alloy. The alloys without B show the cellular β precipitates at grain boundaries in 600°C of aging temperature. The mean cell width of β precipitates drastically increases at grain boundaries when the aging times are longer than 60 hours. No cellular β precipitates at grain boundaries is observed when the boron is added into alloy. The boron is used to decreases the grain boundary energy and prevents the formation of β precipitates during the aging. In $Fe_{40.95}Ni_{28}Co_{17}Al_{11.5}Ti_{2.5}B_{0.05}$ alloy, Omori et al. [89] reported the brittle β precipitates is more favor formed in the high-angle grain boundaries instead of low-angle grain boundaries. The fraction of high-angle boundaries is high in 90% cold-rolled

samples. As a result, the high volume fraction of β precipitates forms in 90% cold-rolled samples even though the born is added into the alloys. The fraction of low-angle boundaries is high in the 98.5% cold-rolled samples. The formation of β precipitates is suppressed due to formation of low-angle boundaries (low grain boundary energy).

Three conditions need to satisfy to show the excellent superelasticity of 13.5% recoverable strain and high tensile strengthen above 1 GPa in FeNiCoAlTaB SMAs [24]. First, the polycrystalline sheet must have the strong texture in the [100] orientation. If the alloy has the random texture, it will show the brittle behavior. The 90% cold rolling doesn't give rise to a significant recrystallization texture in the [100] orientation. The cold-rolled with reduction of over 98% will provide the significant strong texture in the [100] orientation after the solution heat treatment at 1300°C for 18 hours, however the reason is still needed to investigate [24]. Second, the large grain size is required in this material. The mean grain size of over 400μm is obtained by using the solution heat treatment at 1300°C for 18 hours on the 98.6% cold rolling sheet. Third, the fine $L1_2$ precipitates with diameter of 3 nm was introduced in 600°C-72h aged condition to strengthen the austenite matrix, change non-thermoelastic martensitic transformation to thermoelastic martensitic transformation and improve the superelastic strain.

The thermomechanical processing, heat treatment conditions, recrystallization texture, superelastic results (tensile elongation and maximum superelastic strain) of the FeNiCoAlXB (X = Ti, Nb, Ta) polycrystalline alloys are summarized in Table 2.2.

Table 2.2 Summary of the thermomechanical processing, recrystallization texture, tensile elongation, maximum superelastic strain for $Fe_{40.95}Ni_{28}Co_{17}Al_{11.5}Ta_{2.5}B_{0.05}$ [24], $Fe_{40.95}Ni_{28}Co_{17}Al_{11.5}Nb_{2.5}B_{0.05}$ [88], $Fe_{40.95}Ni_{28}Co_{17}Al_{11.5}Ti_{2.5}B_{0.05}$ [89] polycrystalline alloys.

$Fe_{40.95}Ni_{28}Co_{17}Al_{11.5}X_{2.5}B_{0.05}$ Polycrystalline Alloys (X = Ta, Nb, Ti)		
FeNiCoAlTaB	**FeNiCoAlNbB**	**FeNiCoAlTiB**
Thermomechanical Processing		
➢ Hot-rolled at 1300°C ➢ 1300°C – 15 minutes ➢ Cold-rolled (98.6%)	➢ Hot-rolled at 1100°C ➢ 1200°C – 30 minutes ➢ Cold-rolled (98.5%)	➢ Hot-rolled at 1200°C ➢ Cold-rolled (98.5%)
Solution Heat Treatment		
1300°C – 18 hours	1220°C – 1 hour	1200°C – 3 hours
Recrystallization Texture (after the solution heat treatment)		
{035}<100>	{111}<110> {112}<110>	{012}<100>
Aging Heat Treatment		
600°C –72h	600°C – 96h	550°C – 24h
Superelasticity at room temperature under tension		
Superelastic strain : 13.5% Elongation : 20%	Superelastic strain : 5% Elongation : 8.8%	Superelastic strain : 4.2% Elongation : 6.5%

2.3.3 Literature Review of $Fe_{43.5}Mn_{34}Al_{15}Ni_{7.5}$ Alloys Design

Ran et al. [98] and Liu et al. [99-101] investigated the phase equilibria of FeMnAl alloys by thermodynamic calculation. Umino et al. [102] and Zhang et al. [103] determined the phase equilibria and transition temperatures in FeMnAl ternary system based on the thermodynamic calculated and experimental results. Hwang et al. [101-106] and Cheng et al. [107,108] investigated the morphologies, microstructure and orientation

relationship of fcc second phases, which generate from the various heat treatment conditions in the duplex FeMnAl and FeMnAlC alloys conditions. Several types of fcc phases appeared in the bcc austenite matrix after cooling at different rates from 1300°C. The fcc phases included the grain-boundary allotriomorphs (GBA), Widmanstfitten sideplates (WS) and an intragranularphase (IP). The GBAs are generated along the grain boundaries and WS generally have an arrow, fishbone or feather shapes grow out from the grain boundary region. The diamond or leaf shapes are seen in the interior of bcc grains, which is intragranular phase (IP) [101-108].

Ando et al. [22] have studied the magnetic properties and phase change in FeMnAl SMAs and reported the composition dependence of Curie temperature has a significant effect on the martensitic transformation. The unique phase change in $Fe_{49}Mn_{36}Al_{15}$ is attributed to the relation between the austenite/martenstie phase equilibrium temperature and concentration of manganese [22]. Figure 2.5 shows the phase equilibrium between austenite and martensite as a function of Mn content in FeMnAl system. γ and α represent the martensite and austenite, respectively. At lower concentration of Mn + X, the martensite start temperature is located below the first Curie temperature ($T_0^{\alpha/\gamma}$). At the Curie temperature, the free energy of martensite is equal to that of austenite. As a result, the martensitic transformation is from the fcc austenite to bcc martensite. When the concentration of Mn + X increases, the martensitic start temperature passes through the first Curie temperature and below the second Curie temperature. The martensitic transformation changes from the bcc austenite to fcc

martensite. However, the FeMnAl ternary alloy with the non-thermoelastic martensitic transformation shows no superelasticity [22].

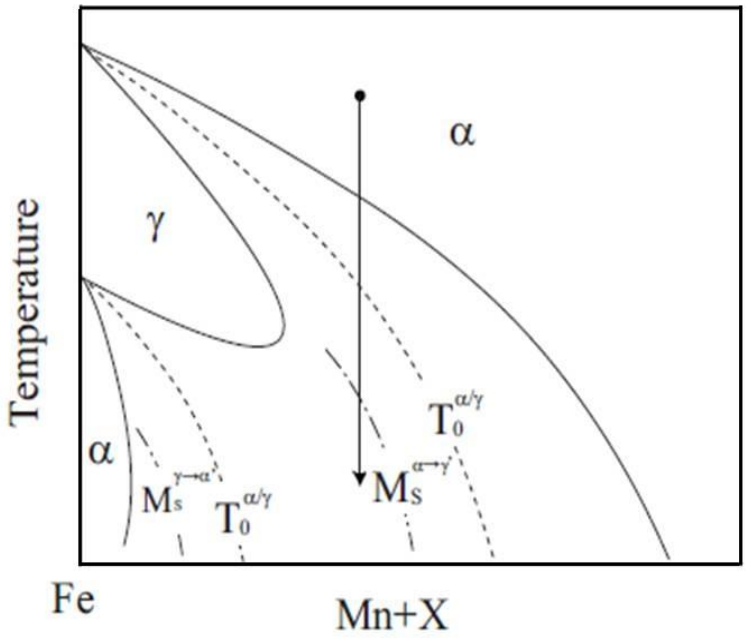

Figure 2.5 Schematic illustration of austenite/martensite phase equilibrium related to the Mn content. X: ferrite stabilizing element [22].

In 2011, Omori et al. [25] reported that the addition of Ni into FeMnAl ternary alloy changes the martensitic transformation from non-thermoelastic to thermoelastic martensitic transformation. The $Fe_{43.5}Mn_{34}Al_{15}Ni_{7.5}$ aged at 200°C for 6 hours shows the 5% recoverable strain from -50°C to 200°C. Here, there is no strong texture in this alloy. As reported, the alloy is hot-rolled at 1200°C and cold-rolled. Before the solution heat treatment, air cooling process is carried out to increase the grain size. In addition, Omori *et al.* [109] reported the B2 precipitates size after aging at 200°C for 15 minutes is around 10 nm. During the heating/cooling, the precipitates were distorted with the

inclination angle about 95°, which is most likely caused by shearing during the martensitic transformation. Since the distortion angle of precipitates is the same as the monoclinic distortion angle of martensite and no dislocation was observed at the interface between martensite and the precipitates, it was suggested that the precipitates were coherent with the martensite phase as well as the austenite phase [109].

In 2013, Omori *et al.* [60] investigated the effect of grain size on superelasticity in textured $Fe_{43.5}Mn_{34}Al_{15}Ni_{7.5}$ polycrystalline wire. The wire was solution heat treated at 1200°C for 30 minutes to obtain the strong texture in the <110> orientation and the single austenite phase. Large grain size about 433 is obtained by annealing at 1200°C flowed by air cooling to room temperature. Then, the homogeneous wire was aged at 200°C for 3 hours. The 5% recoverable strain was obtained at room temperature under tension test.

2.4 Bain Distortion Theory and Theoretical Transformation Strain in FeMnAlNi Shape Memory Alloys

The martensitic transformation in pure iron follows the classical fcc-bcc Bain distortion theory (proposed by Bain in 1924) and it is believed that this martensitic transformation path can also apply in the FeMnAlNi SMAs [25]. The martensitic transformation in FeMnAlNi SMAs is from the bcc austenite to fcc martensite. In the Bain distortion model, both the bcc and fcc structure can be assumed as the bct structure and the bcc-fcc martensitic transformation can be explained by the tetragonal Bain's path, show in Figure 2.6 [39,40]. There are three possible martensite variants during the

bcc-fcc martensitic transformation, and each martensite variant has its c-axis or z'-axis parallel to one of the three [100] direction. Based on the theoretical framework [110-112], the three independent lattice correspondences of the austenite and martensite phases are called Bain correspondence and can explain as follows.

Let a lattice vector $[x_1, x_2, x_3]_f$ in the fcc lattice correspond to a lattice vector $[x_1, x_2, x_3]_b$ in the bcc lattice. Therefore, the Bain correspondence gives the following relation between the fcc lattice and bcc lattice.

$$(\mathrm{x}_1)_b \sim (x_1 - x_2)_f \ , \qquad (\mathrm{x}_2)_b \sim (x_1 + x_2)_f \ , \qquad (\mathrm{x}_3)_b \sim (x_3)_f \tag{2.3}$$

The Bain matrix is

$$\begin{bmatrix} x_1 \\ x_2 \\ x_3 \end{bmatrix}_b = \begin{bmatrix} 1 & \bar{1} & 0 \\ 1 & 1 & 0 \\ 0 & 0 & 1 \end{bmatrix} \begin{bmatrix} x_1 \\ x_2 \\ x_3 \end{bmatrix}_f \tag{2.4a}$$

Or Bain inverse matrix

$$\begin{bmatrix} x_1 \\ x_2 \\ x_3 \end{bmatrix}_f = \frac{1}{2} \begin{bmatrix} 1 & 1 & 0 \\ \bar{1} & 1 & 0 \\ 0 & 0 & 2 \end{bmatrix} \begin{bmatrix} x_1 \\ x_2 \\ x_3 \end{bmatrix}_b \tag{2.4b}$$

The Bain correspondence matrices or correspondence between the fcc and bcc lattice plans is

$$\begin{pmatrix} h_1 & h_2 & h_3 \end{pmatrix}_b = \begin{pmatrix} h_1 & h_2 & h_3 \end{pmatrix}_f \frac{1}{2} \begin{bmatrix} 1 & 1 & 0 \\ \bar{1} & 1 & 0 \\ 0 & 0 & 2 \end{bmatrix} \tag{2.5a}$$

Or inversely

$$\left(h_1\ h_2\ h_3\right)_f = \left(h_1\ h_2\ h_3\right)_b \begin{bmatrix} 1 & \bar{1} & 0 \\ 1 & 1 & 0 \\ 0 & 0 & 1 \end{bmatrix} \tag{2.5b}$$

For the bcc-fcc transformation (FeMnAlNi), three independent lattice correspondence of the transformation can obtain by equation 2.9b or 2.10b and are shown in Table 2.3.

Table 2.3 Lattice correspondences of martensite and austenite in FeMnAlNi SMA; subscripts A and M represent austenite and martensite, respectively.

	Martensite Variant 1	Martensite Variant 2	Martensite Variant 3
$[100]_A$	$[1\bar{1}0]_M$	$[10\bar{1}]_M$	$[01\bar{1}]_M$
$[010]_A$	$[110]_M$	$[011]_M$	$[101]_M$
$[001]_A$	$[001]_M$	$[100]_M$	$[010]_M$

In the bcc structure, all three lattice vectors have the same length, which c/a ratio is equal to one. For the fcc structure, the fcc unit cell is equivalent to the bct unit cell with height-to-base ratio (c/a) ratio of $\sqrt{2}$. During the transformation, the crystal expands in the c-axis (z' direction) and it shrinks in the a-axis (X' and Y' direction). It means when the single crystal is expanded in the Z direction of the bcc austenite, the tensile strain can be assisted by one martensite variant. On the other hand, if the single crystal is pulled in the z direction of the austenite, the compressive strain can be accommodated by two martensite variants. We believe the variant selection will affect the superelastic

response of FeMnAlNi single crystal along the [100] orientation under both tension and compression.

Theoretical transformation strains in both tension and compression are calculated based on the lattice deformation theory (single variant strain) [110-112]. This theory assumes the single crystal austenite is fully transformed into a single crystal martensite without twins. From this method, it generates three principal lattice strains (η_1 , η_2 and η_3) . As we mention before, there are two martensite variants in the compression direction and only one martensite variant in the tension direction during the bcc-fcc transformation. Therefore, the theoretical transformation strain in compression is equivalent to η_1 and η_2 ($\eta_{compression} = \eta_1 = \eta_2$) and it in tension is equivalent to η_3 ($\eta_{tension} = \eta_3$) . In the Bain distortion model, since c/a ratio is equaled to 1 in the bcc austenite, we use a_A to represent the lattice parameter ($a = a_A$, $c = a_A$). In the fcc martensite structure with the c/a of $\sqrt{2}$, we use a_M represent c and a, ($1/\sqrt{2}a = a_M$, $c = a_M$). The equation is defined as follow.

$$\eta_{compression} = \frac{(1/\sqrt{2})a_M - a_A}{a_A} \times 100\% \qquad \eta_{tension} = \frac{a_M - a_A}{a_A} \times 100\% \qquad (2.6)$$

The lattice parameters of $a_M = 0.3672nm$ and $a_A = 0.2903nm$ were used from reference [25] to calculate the theoretical transformation strain in the [100] orientation. From the calculation, the maximum theoretical transformation strain in the [100] orientation are 26.5% in tension and 10.5% in compression, respectively.

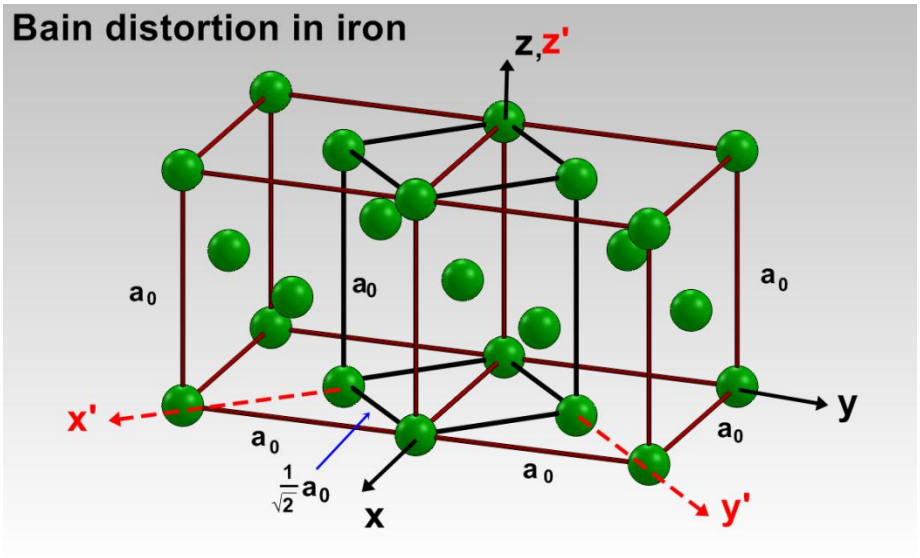

(a)

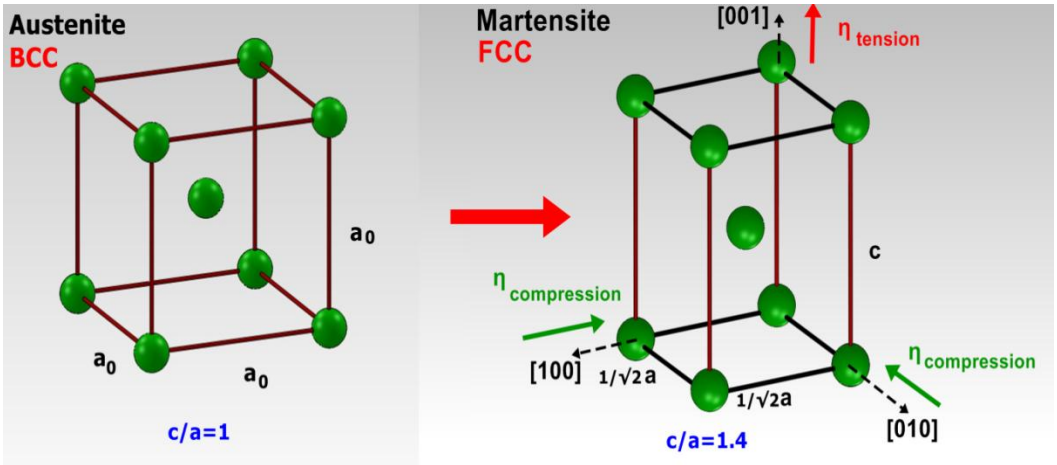

(b)

Figure 2.6 Illustration of the bcc-fcc martensitic transformation that occurs in the FeMnAlNi shape memory alloys. The bcc unit cell with the c/a ratio (the ratio of the height to the base) is equivalent to one. The fcc unit cell is equivalent to a bct unit cell with the c/a ratio of 1.41. The transformation occurs through a shorting of the base of the bcc unit cell (from a_0 to $1/\sqrt{2}a$), and a lengthening of its height (from a_0 to c).

CHAPTER III

EXPERIMENTAL PROCEDURE

The aim of this chapter is to present details on the several microstructural characterization methods and superelastic testing used throughout this study.

3.1 As-Received Materials

The initial states of single crystals and polycrystals used in this study were summarized as follow.

The ingots of FeMnAlNi with nominal compositions of $Fe_{43.5}Mn_{34}Al_{15}Ni_{7.5}$ (at.%) were prepared by using vacuum induction melting process. Single crystals were grown by using the Bridgman methods in a helium condition. The compression specimens with the dimension of 4 mm × 4 mm × 8 mm (length × width × height) and the dog-bone shaped tension samples with the dimension of 1.5 mm × 3 mm × 8 mm (gauge section) were cut in the desired single crystal orientations ([100], [123], and [111]) by using wire electro-discharge machining (EDM).

Before solution and aging heat treatments, all samples were first mechanically ground to remove the surface oxidation and wire EDM residues. In order to prevent the reaction with the quartz tube during the solution heat treatment, FeMnAlNi single crystals were sandwiched between two FeMnAlNi polycrystalline samples and sealed into quartz tube together under high purity argon and solution heat treated at 1200°C for 1 hour followed by quenching into ice water. The homogenized samples were then aged

at 200 °C and 300 °C for different time periods in argon condition and quenched into water to obtain B2 precipitates. For the sake of brevity, we will refer to the $Fe_{43.5}Mn_{34}Al_{15}Ni_{7.5}$ single crystals aged at 200°C and 300°C for x hours as "200°C-xh" and "300°C-xh".

The FeMnAlNi polycrystalline bar with the 3.175 cm diameter by 30.48 cm long was fabricated by the sophisticated alloy company with the nominal composition of $Fe_{43.5}Mn_{34}Al_{15}Ni_{7.5}$ (at.%). The ingots with dimensions of 15×48×10.02 mm^3 (length × width × height) were cut out from the polycrystals bar by using EDM for the thermomechanical processing experiment.

3.2 Thermomechanical Processing

Hot-rolled and cold-rolled experiments of the $Fe_{43.5}Mn_{34}Al_{15}Ni_{7.5}$ polycrystals sheet were carried out by using FENN rolling mill machine which had the pair of grooved rollers, as shown in Figure 3.1a. Figure 3.1b shows the rolling direction of FeMnAlNi sheets, the RD, TD and ND were represented rolling direction, transverse direction and normal direction of the FeMnAlNi sheet. The processing conditions and results were given in Table 3.1.

For the hot-rolled experiment, the polycrystals ingot with the dimension 15×48×10.02 mm (Length × Width × Height) was first heat treated at 1200°C for 1 hour to homogenize the ingot. The homogeneous ingot was hot rolled by grooved rollers to 9.5 mm in thickness. After the first hot-roll testing, the sheet was again heat treatment at 1200°C for 30 minutes and then hot rolled to 9 mm in thickness. The same procedure

was repeated until the sheet was hot rolled to 4.2 mm in thickness. Then, the hot-rolled sheet was annealed at 900°C for 1 hour and quenched into water. For the cold-rolled experiment, the hot-rolled sheet was annealed at 900°C for 1 hour and then the annealed sheet was cold-rolled 76% to 1 mm in thickness. The detail of three thermomechanical processing will show in the chapter VII.

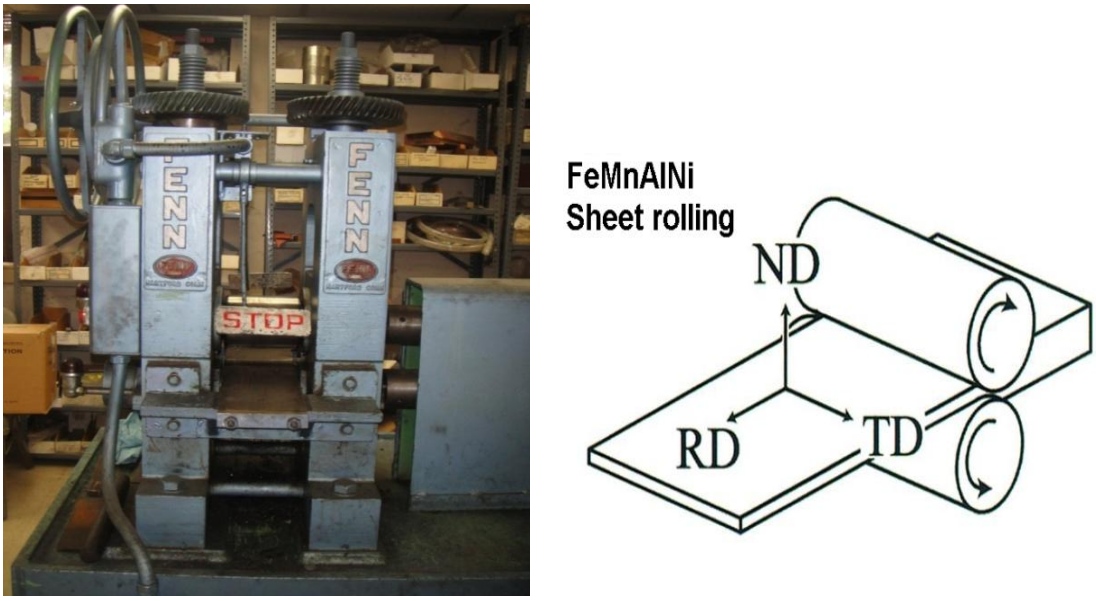

Figure 3.1 (a) FENN rolling machine at Texas A&M University. (b) Schematic illustration of rolling experiment.

Table 3.1: Summary of the $Fe_{43.5}Mn_{34}Al_{15}Ni_{7.5}$ thermomechanical processing conditions.

Experiment	Processing conditions	Results
Experiment 1	Hot-Rolled at 1200°C + Cold-Rolled	Failure
Experiment 2	Hot-Rolled at 1200°C + 1200°C , 1 h + Cold-Rolled	Failure
Experiment 3	Hot-Rolled at 1200°C + 900°C , 1 h + Cold-Rolled	Success

3.3 Microstructural Characterization

3.3.1 Optical Microscopy and Wavelength Dispersive Spectrometer

The microstructure of FeMnAlNi single crystals and polycrystalline were carried out by optical microscopy (OM). The surfaces of the specimens were mechanically ground down to 1000SiC grit paper and then polished to a final step of 0.05 μm colloidal silica and then etched using an etching solution of 7% nitric acid and 93% ethanol by volume, and the OM images were captured with a Keyence digital VH-Z100 optical microscope.

The chemical composition analyses were measured by a scanning electron microscopy (SEM) JEOL JSM-6400 equipped with Camera SX-100 electron microprobe with four wavelength dispersive spectrometer (WDS). The SEM samples were mechanically polished to a final step of 0.05 μm colloidal silica and examined without chemical etching. The back-scattered electron (BSE) mode was used to determine the phase present. It should be noted that the JEOL JSM-6400 equipment can not only identify the different compositions of phase but also different crystal structure. As a result, the different color in the SEM image represents different phases or composition in the sample.

3.3.2 Transmission Electron Microscope

The crystal structure and size of precipitates was observed by transmission electron microscopy (TEM). TEM samples were conducted using a FEI Tecnai G^2 F20 electron microscope operated at a voltage of 200 kV at room temperature. Thin TEM

samples were prepared by mechanical grinding down to 50μm and followed by ion milling under 3.5kV and 5 mA until a hole was formed in the center. Microstructure characteristics such as size of precipitates were observed by transmission electron microscopy (TEM) by using FEI Tecnai G^2 F20 electron microscope. TEM samples of FeMnAlNi single crystals were first mechanically ground down to a thickness of 40μm. The thin samples were put into the vacuum chamber inside the ion-milling machine and ion beam will point in the central area of the sample. The ion-milled will stop until a hole appeared in the center of the specimens. For the tension samples after deformed 8% and compression samples after deformed 6%, TEM samples (3mm in diameter) were first grinded to 70μm in the thickness. Thin foils were produced by twin-jet electro-polishing in a 30% nitric acid and 70% methanol at -20°C with a voltage between 8~12V [113,114].

3.3.3 Atom Probe Tomography

Due to the length scale of these precipitates, determining their composition and volume fraction proved to be difficult using TEM. As a result of this, atom probe tomography (APT) was used to determine the volume fraction and composition, while providing a 3D reconstruction of the precipitates. The APT was performed using a Cameca Local Electrode Atom Probe (LEAP) 3000XSi. The atom probe specimen were lifted-out from the bulk sample, and placed onto pre-fabricated Si posts using a FEI Quanta 200 3D Dual Beam scanning electron-focused ion beam microscope equipped with a probe micromanipulation lift-out system. Once attached to the Si post, the

specimen were annular milled to yield the appropriate geometric needle shape with a radius of ~ 100 nm required for field evaporation. More in-depth details of the FIB-based atom probe preparation can be found elsewhere [115-117]. The specimen were held at a base temperature of 30K (-243°C), ran in laser mode with a pulse rate of 200 kHz, pulse energy 0.2 nJ, and a target evaporation set at 0.5. The atom probe data was reconstructed using the IVAS 3.6.6 software package.

3.4 Vickers Microhardness Testing

Microhardness tests were performed at room temperature by using a Buehler Omnimet (Lake Bluff, IL) microhardness equipment with a Vickers-type microindenter. Vickers Hardness values were determined by using 300N load and a loading time of 15s. In single crystal study, the compression samples with the [100] orientation were homogenized at 1200°C for 1 hour followed by quenching into ice water. The homogenized compressive samples were cut from the lateral side into 8 samples with the dimension 4 mm x 4 mm x 1 mm (length x width x height) by using the EDM machine. The samples were subsequently aged at 200°C and 300°C at various times (0.25h, 1h, 3h, 6h, 10h, 12h and 24h) followed by a water quench. Vickers microhardness values were measured on the {100} faces of the single crystals at room temperature. In FeMnAlNi polycrystals study, the cylindrical sample with the 3.175 cm diameter by 5 mm thickness was cut from the polycrystals bar. The sample was solution heat treatment at 1200°C for 1 hour followed by quenching into ice water. The small disc samples with the 0.5 cm diameter were cut from the solution-treated sample and subsequently heat

treated at various temperatures (800°C, 900°C, 1000°C, 1100°C, 1150°C) for 1 hour followed by quenching into water. The hardness values were measured on the same surface of all the disc samples. The microhardness of sheets after thermomechanical processing was measured on the upper surface of the sheet.

3.5 X-Ray Diffraction

The crystallography texture of the polycrystals was established by a Bruker-AXS D8 X-ray diffractometer with CuK_{α} (1.5406Å). The X-ray diffraction (XRD) pattern of the polycrystals was measure in the 2Θ range of 30°-100°. Because major phase is the bcc phase after the solution heat treatment, bcc peaks were selected for the texture analysis. The planes for the texture analysis were selected (110), (200) and (221). The inverse pole figures for the rolling direction (RD), normal direction (ND) and transverse direction (TD) were generated form the diffraction pattern data by using popLA software.

3.6 Thermomagnetization Testing

The thermo-magnetization curves of FeMnAlNi aged samples before and after the incremental strain experiments in both tension and compression were obtained by a Superconducting Quantum Interference Device (SQUID). The sample was first heated up to 130 °C from the room temperature under a zero magnetic field, and then the sample was cooled down to -260 °C and heated up to 130 °C under a constant magnetic field of 0.5 and 7 kG. The cooling and heating rate is 5 $Kmin^{-1}$. Moreover, the phase

transformation temperatures of FeMnAlNi alloy (austenite finish temperature, A_f ; austenite start temperature, A_s ; martensite start temperature, M_s ; and martensite finish temperature M_f) were determined based on thermomagnetization curve under the magnetic field of 0.05 kG. The temperature hysteresis or thermal hysteresis is defined as $|A_f - M_s|$. The determination of transformation temperature and temperature hysteresis were shown in Figure 3.2 as an example.

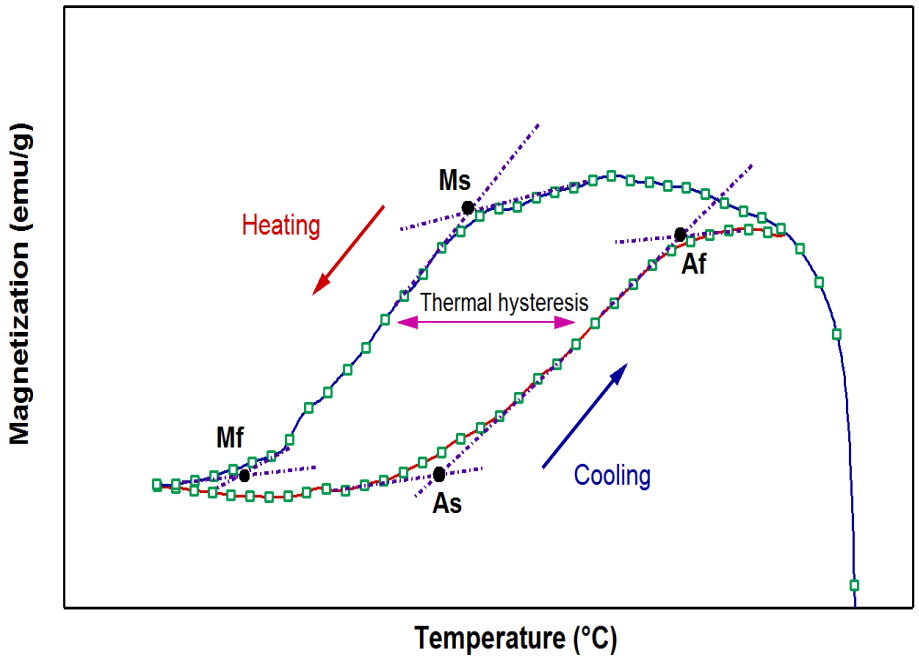

Figure 3.2 Representative magnetization versus temperature response of an SMA under magnetic field schematic illustration of transformation temperature and temperature hysteresis.

3.7 Mechanical Testing

The superelastic characterizations were conducted by two sets of superelastic experiments in both tension and compression: constant strain superelastic experiments at

various temperatures and incremental strain experiments at room temperature. In the constant strain experiments, the samples were loaded to a strain level of 2% at various test temperatures from -80 °C to 160 °C. From these experiments, the transformation stress levels at different temperatures were determined, and the transformation stress-temperature diagram, which showed the temperature dependence of the transformation stress, was constructed. In the incremental strain experiment, samples were tested at room temperature to determine the maximum recoverable strain levels. The samples were first loaded to 2% strain and unloaded. The strain levels were then increased during each loading-unloading cycle until the martensite transformation was completed or the samples was failure. Both superelastic experiments were conducted using a servo-hydraulic Material Test System (MTS) test frame with a strain rate of $\dot{\varepsilon} = 5 \times 10^{-4} s^{-1}$. The heating and cooling of tension and compression samples was achieved by heating band and liquid nitrogen. The upper and bottom grips were heated by heating bands and cooled by liquid nitrogen flowing through copper tubing wrapped around the grip. The heating and cooling rate is 10°C /min. To measure specimen temperature, a thermocouple was attached directly on the gauge section of tension samples and the compression samples. A MTS high temperature extensometer with a 12.7 mm gauge length was used to measure the axial strain. In the tension test, the MTS high temperature extensometer was directly attached on the gauge section of the tensile sample. In the compression test, the MTS high temperature extensometer was attached to the grips roughly 2 mm from the sample.

CHAPTER IV

SUPERELASTIC RESPONSE OF A SINGLE CRYSTAL FeMnAlNi SHAPE MEMORY ALLOYS IN BOTH TENSION AND COMPRESSION

In this chapter, the superelastic behavior of single crystalline $Fe_{43.5}Mn_{34}Al_{15}Ni_{7.5}$ samples oriented along the [100] direction was investigated under tension and compression after a precipitation heat treatment at 200°C. In constant strain, multi-temperature experiments, the single crystals showed a σ_{SIM} vs. temperature slope of 0.54 MPa $°C^{-1}$ in tension and 0.41 MPa $°C^{-1}$ in compression, and superelasticity over a wide temperature range from -80°C to 160°C. The irrecoverable strains in both tension and compression samples detected during the superelastic experiments were found to be due to retained martensite in detailed transmission electron microscopy investigations. The volume fraction of the retained martensite in the samples tested under tension was considerably larger than those for the samples tested in compression showing that 20 the transformation is less recoverable in tension. The differences in the volume fraction of retained martensite and reversibility in both tension and compression are attributed to high density of dislocations in the tension samples as compared to the compression samples. The differences between the shape of the stress–strain curves under tension and compression are attributed to the lower number of martensite variants activated under

---

*Reprinted with permission from " Superelastic response of a single crystalline FeMnAlNi shape memory alloy under tension and compression" by LW Tseng, Ji Ma, SJ Wang, I Karaman, M Kaya, ZP Luo, YI Chumlyakov, 2015. Acta Materialia,copyright 2015 by Acta Materialia Inc. published by Elsevier Ltd.

tension as compared to compression, which were clearly verified with the transmission electron microscopy examinations.

4.1 Microstructure

The room temperature BSE image of the FeMnAlNi single crystals aged at 200 °C for 15 minutes was shown in Figure 4.1. Because the JEOL JSM-6400 microscope is equipped with high voltage beam, it can detect not only composition differences but also structural differences. We observe both the martensite and austenite crystal structure at room temperature, where the white areas represent the martensite plates and the dark areas displays the austenite matrix.

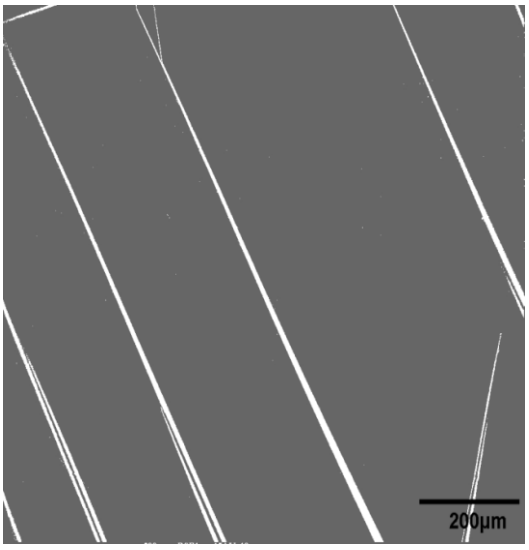

Figure 4.1 Back scattered electron micrograph of the FeMnAlNi single crystals aged at 200 °C for 15 minutes.

Table 4.1 shows the WDS analysis result of single crystals aged at 200°C for 15 minutes. Ten measurements were taken from austenite matrix and ten measurements

from martensite plates. There is no difference between the composition of austenite and martenstie. The composition result was used average of these twenty measurements, shown in Table 4.1. The result demonstrates the compositions of the single crystal are similar to the nominal composition after the solution heat treatment.

Table 4.1 Composition of the FeMnAlNi single crystal oriented along the [100] direction aged at 200 °C for 0.25h found by WDS: +/- denotes one standard deviation from a total of 20 measurements.

	Fe (at%)	Mn (at%)	Al (at%)	Ni (at%)
Measured	43.28 ± 0.11	33.9 ± 0.08	15.1 ± 0.11	7.72 ± 0.03
Nominal	43.5	34	15	7.5

Figure 4.2a and b show the bright field TEM image and corresponding selected-area electron diffraction pattern (SAED) of the FeMnAlNi single crystals aged at 200 °C for 15 minutes. The area circled by white dashed lines shows the precipitate size and position. The diameter of the precipitates is roughly 3-5 nm. In the corresponding SAED pattern, the strong reflections are from the austenite (bcc structure) along its [011] zone axis. Apparently, weak reflections from the B2 phase (bcc structure) appear at the positions between the austenite spots, as indicated with circles. Other weak reflections are identified as two variants of [112] martensite (fcc structure). The rest weak reflections are produced by double diffraction. It is seen that $(2\bar{1}1)_A$ is nearly parallel to $(\bar{3}11)_M$ and their lattice spacing are very close, $d_{2\bar{1}1} = 1.18$ Å , $d_{\bar{3}11} = 1.11$ Å. The austenite is the majority phase while the martensite is the minor remaining phase. The result demonstrates austenite and martensite phase coexist at room temperature. Omori

et al. has also reported [109] the same B2 precipitates after aging at 200°C for 15 minutes, with the average sizes of 10 nm, which is comparable, but slightly larger than the size of precipitates we observed in the present study after the identical heat treatment. They also reported that the precipitates were distorted with the inclination angle about 95°, which is most likely caused by shearing during the martensitic transformation. Since the distortion angle of precipitates is the same as the monoclinic distortion angle of martensite and no dislocation was observed at the interface between martensite and the precipitates, it was suggested that the precipitates were coherent with the martensite phase as well as the austenite phase [109].

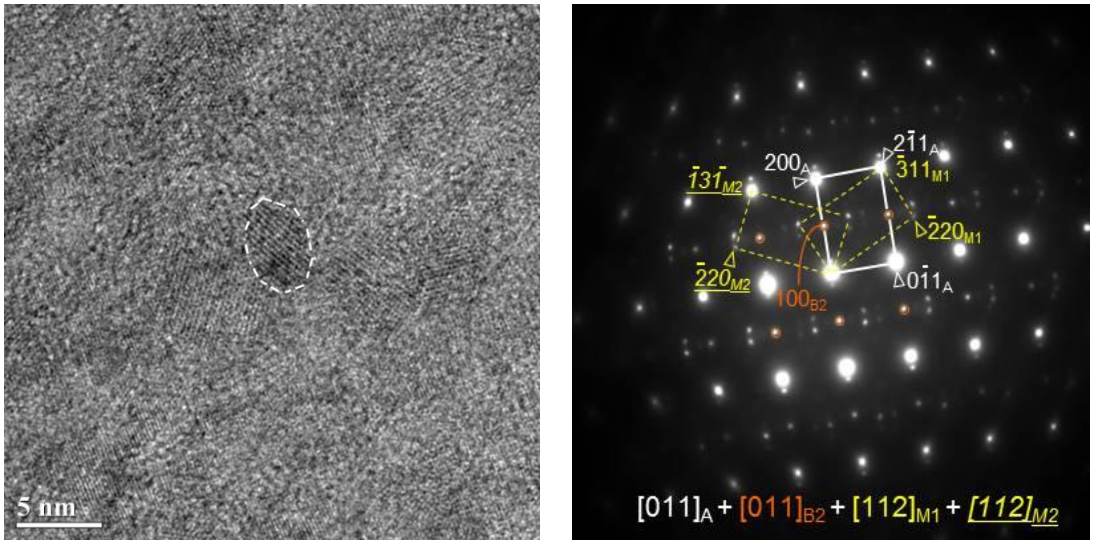

(a) (b)

Figure 4.2 Room temperature TEM micrographs of the FeMnAlNi single crystals aged at 200 °C for 15 minutes. (a) the bright field TEM image and (b) corresponding selected-area electron diffraction (SAED) of the FeMnAlNi single crystals aged at 200 °C for 15 minutes. A precipitate is circled with the dashed white lines in Figure 4a, showing the diameter of roughly 3-5nm. The ordered B2 precipitates with {100} superlattice reflection spots is visible within in the A2 (BCC) matrix when viewed along the [011] zone axis. Other weak reflections are identified as two variants of [112] martensite (FCC). The remaining weak reflections are produced by double diffraction.

4.2 Transformation Temperatures

Figure 4.3 displays the thermo-magnetization result of FeMnAlNi single crystal aged at 200°C for 15 minutes. In this test, the sample was first heated up from room temperature to 130°C. After the test temperature reached 130°C, a magnetic field of 0.5 kG was applied and the sample was cool down to -260°C and heat up to 130°C under the applied field. Magnetization decreased during the cooling and increased during the heating. From the result, the austenite appears to be ferromagnetic while the martensite is weakly magnetic. We used the tangent line method to determine the transformation temperature as indicated in the figure 4.3. The transformation temperatures of the aged single crystal are: A_f = 30°C , A_s = -93°C , M_s = -90°C and M_f = -213°C. The temperature hysteresis is about 120°C.

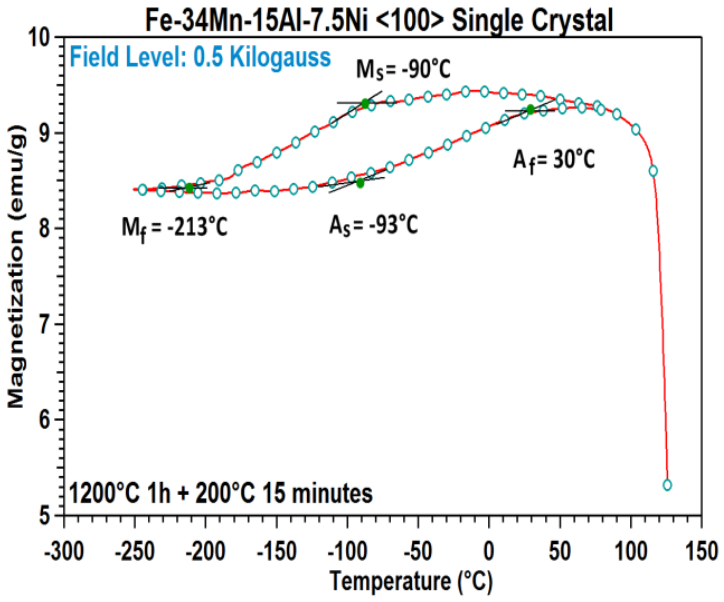

Figure 4.3 Magnetization response of the FeMnAlNi single crystals aged at 200°C for 15 minutes as a function of temperature under a magnetic field of 0.5 kG.

4.3 Superelastic Responses in both Tension and Compression

Figure 4.4a and b display the compressive and tensile responses of FeMnAlNi [001] single crystals aged at 200°C for 15 minutes. For this test, the samples were first loaded to 2% strain and unload at -80°C. After the test, the samples were heated to 100°C (above A_f) and cooled down to next test temperature (-40°C) to recover all irrecoverable strain from previous test. The same procedures were applied in the test temperature (-40°C, 0°C, 40°C and 80°C). For the test temperature 120°C and 160°C, the superelastic test was directly carried out at the test temperature. The critical stress in both tension and compression is summarized as a function of temperature in Figure 4.5. In both cases, it is seen that the critical stress increases only slightly with increasing test temperature. The relationship between temperature and critical stress appears to be linear which follow the Clausius-Clapeyron (CC) relation, show in equation (2.2)

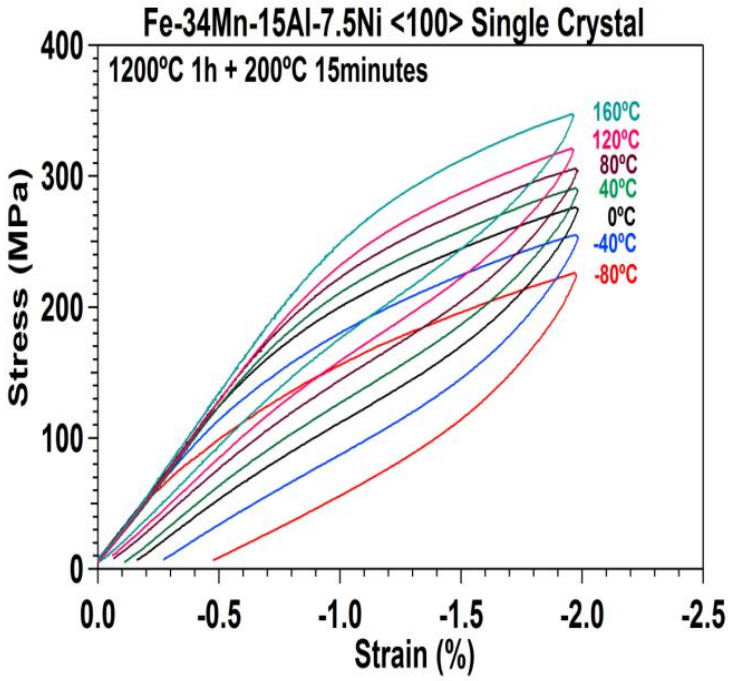

(a)

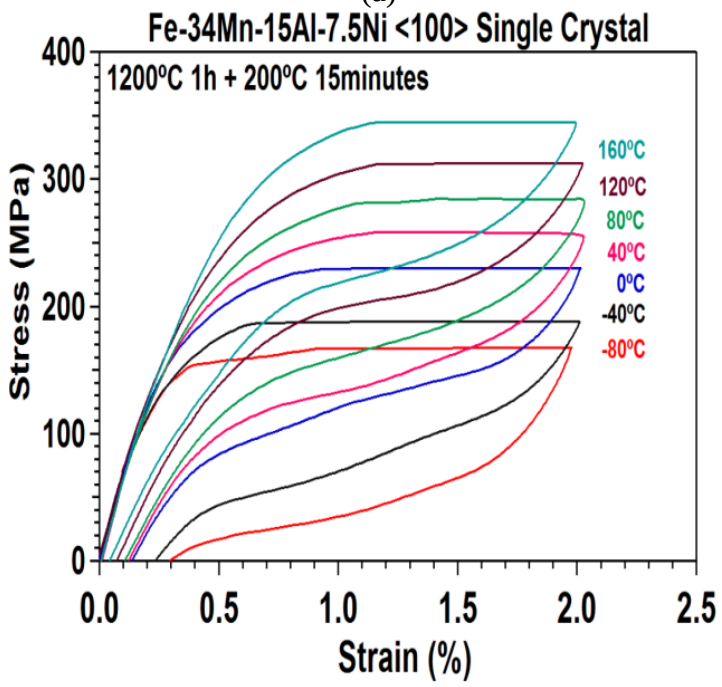

(b)

Figure 4.4 Stress vs Strain response of the FeMnAlNi shape memory single crystals oriented along the <100> direction at various temperature under (a) 2% compressive strain and (b) 2% tensile strain.

The slopes of the critical stress-temperature curves ($d\sigma_c/dT$) for the present single crystals are 0.54 MPa °C $^{-1}$ in tension and 0.41 MPa °C^{-1} in compression. In the polycrystalline samples of the same composition, the $d\sigma_c/dT$ value was reported to be 0.74 MPa °C^{-1} under tension in between -80°C and 200°C in a sample aged at 200 °C for 6 hours [25]. Thus, the values for $d\sigma_c/dT$ in the single crystals are, therefore, comparable to the reported value for the polycrystalline samples. Strikingly, these values are significantly lower than those for the [100] oriented single crystals of CoNiGa (2.2 MPa °C^{-1} [118]), CuAlNi (1.7 MPa °C^{-1} [119]), NiMnCoIn (2.1 MPa °C^{-1} [120]), NiTi (4 - 8 MPa °C^{-1} [121]), and CoNiAl (4.1 MPa °C^{-1} [122]), all in compression, and CoNiAl (1.3 MPa °C^{-1} [122]) in tension. Such temperature insensitivity of σ_c can stem from either low ΔS or large transformation strain or both. The theoretical transformation strain of the [100] oriented $Fe_{43.5}Mn_{34}Al_{15}Ni_{7.5}$ is larger than most of the alloys listed above which partially explains the low $d\sigma_c/dT$ values. This property makes the present FeMnAlNi alloys an excellent candidate for applications requiring nearly temperature-invariant superelastic response.

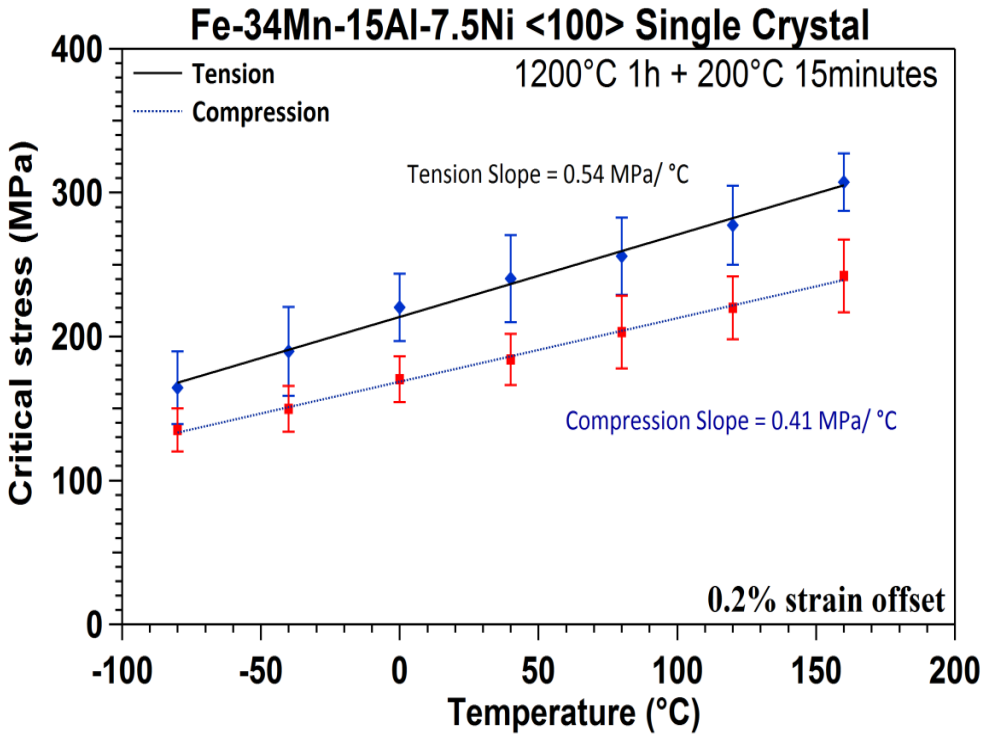

Figure 4.5 Temperature dependence of critical stress (σ_c) of FeMnAlNi single crystal in both tension and compression.

4.4 Experimental and Theoretical Transformation Strain

Figure 4.6a shows the room temperature superelastic response of the [001] oriented FeMnAlNi single crystals under incremental compressive loading-unloading cycles. The slope of the stress-strain curves remains low in the plateau region during the stress-induced martensitic transformation, but increases sharply near 9% applied strain, which indicates near completion of the martensitic transformation and start of intense martensite variant-variant interaction. Figure 4.6b shows the recoverable strain and irrecoverable strain as a function of applied strain levels from the incremental strain experiment of Figure 4.6a. For the compression samples, the irrecoverable strain is around 6% (out of 10.5% theoretical transformation strain). This suggests that the

deformed compressive samples retain about 60% volume fraction of martensite. Figure 4.6c shows an optical microscopy image taken on the sample surface after the 10% applied strain, exhibiting significant amount of martensite plates in the austenite matrix after unloading, which suggests a large volume of retained martensite exists. The irrecoverable strain levels appear to be high, and we believe that a significant portion of it, if not all, comes from the retained martensite instead of plastic deformation.

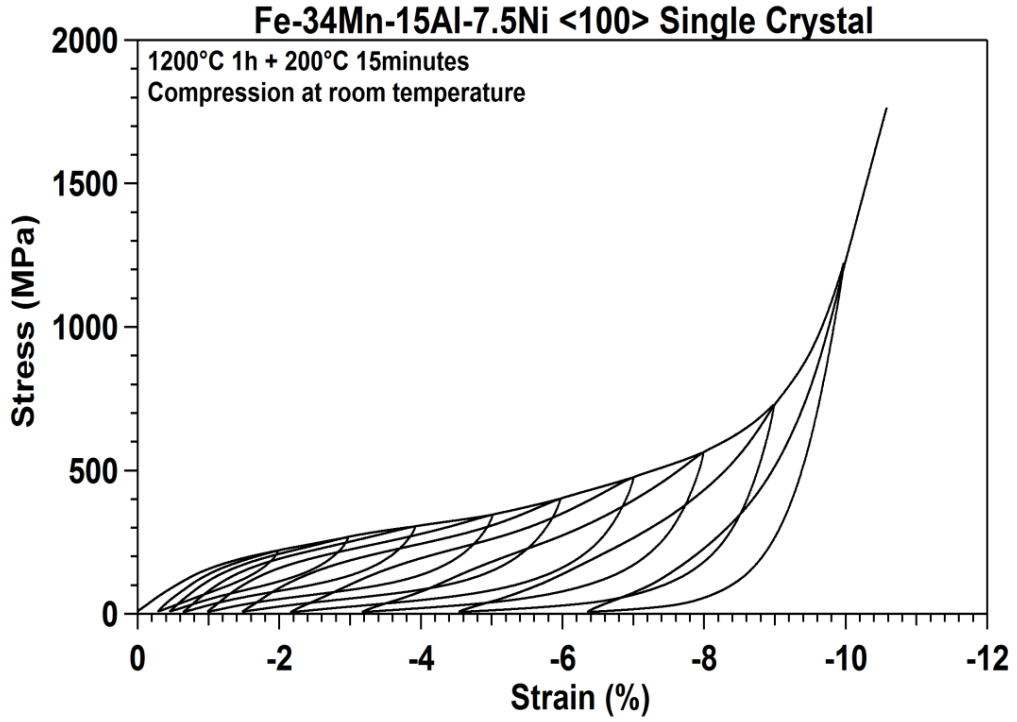

(a)

Figure 4.6 The strain dependence of the superelastic response of the $Fe_{43.5}Mn_{34}Al_{15}Ni_{7.5}$ single crystals oriented along the <100> direction under incremental compression loading at room temperature. (a) shows the stress-strain response. (b) is the evolution of recoverable strain and irrecoverable strain as a function of applied strain. (c) is the optical microscopy image of the compression sample after the test shown in (a), taken on the sample surface. The image shows the large volume fraction of retained martensite on the sample.

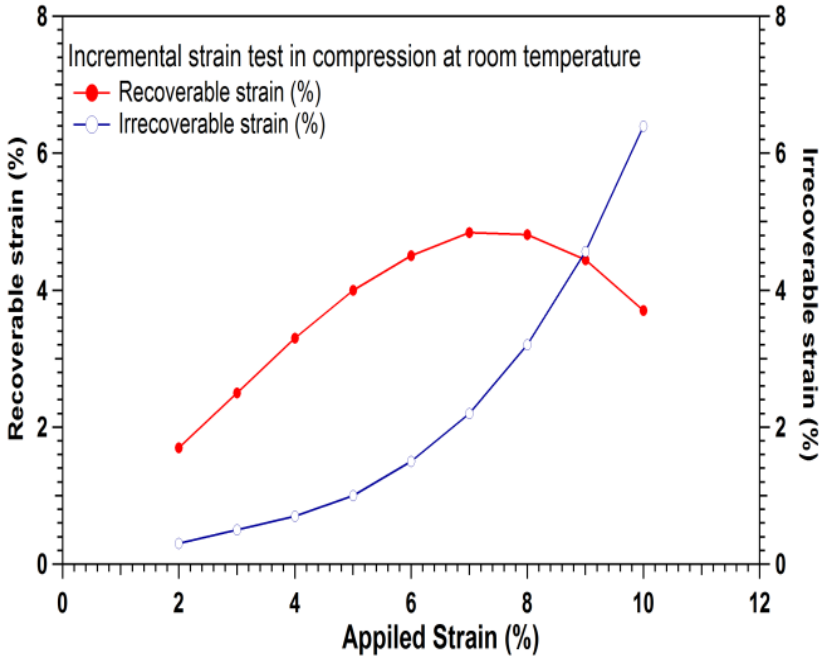

(b)

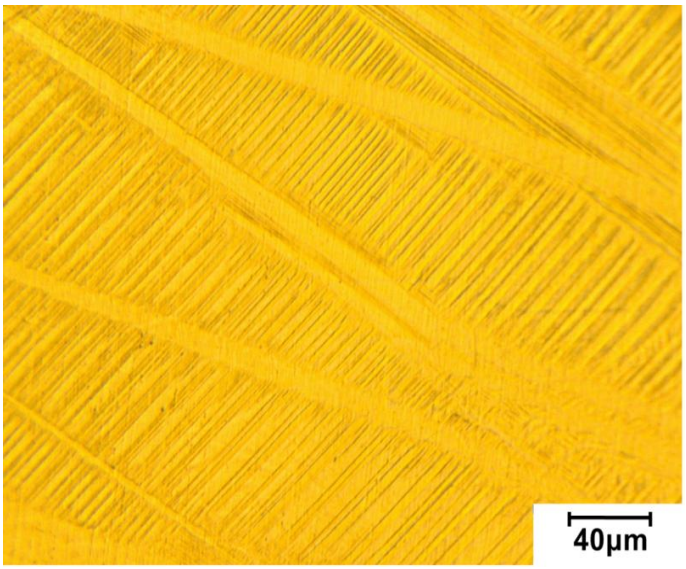

(c)

Figure 4.6 Continued.

Figure 4.7a shows the tensile superelastic response of the single crystal samples under incremental strain experiments at room temperature. The differences in the response of the tension samples as compared to that of the compression samples are: (a) much higher applied strain levels over 20% at low stresses; (b) load drop near 5% applied strain; (c) long plateau region, an indication of stress-induced martensitic transformation; and (d) higher irrecoverable strain. Figure 4.7b represents the recoverable strain and irrecoverable strain as a function of applied strain from the incremental strain experiment. For the tension samples, the irrecoverable strain is around 24% (out of 26.5% theoretical transformation strain). This suggests that the deformed tensile samples retain about 90% volume fraction of martensite. Figure 4.7c presents an optical microscopic image of the tensile sample after 26% applied strain taken near the fracture surface and shows large martensite plates and needle-like thin plates. The band-like regions can observe in Figure 4.7c. We performed electron backscatter diffraction (EBSD) mapping to determine the phases present in these band-like regions. Figure 4.7d shows the EBSD analysis on the gauge section of tension sample after the incremental strain test. The red and green colors represent the martensite and austenite phases, respectively. From the analysis result, the volume fraction of martensite and austenite is about 0.985 and 0.011, respectively, so that the sample is almost fully martensitic after the test. We further examined the boundaries of these band-like features in TEM, which appears to be composed of a mixture of {111}<112> twin boundaries shown in Figure 4.9b (known to be a deformation twin system in FCC), and areas containing small amount (with thicknesses around ~200 nm) of remnant austenite. These results suggest

that the sample is indeed almost fully martensitic after the tensile test, and the band-like structures are a combination of martensite deformation twins and perhaps small amount of habit plane variants from the remnant austenite.

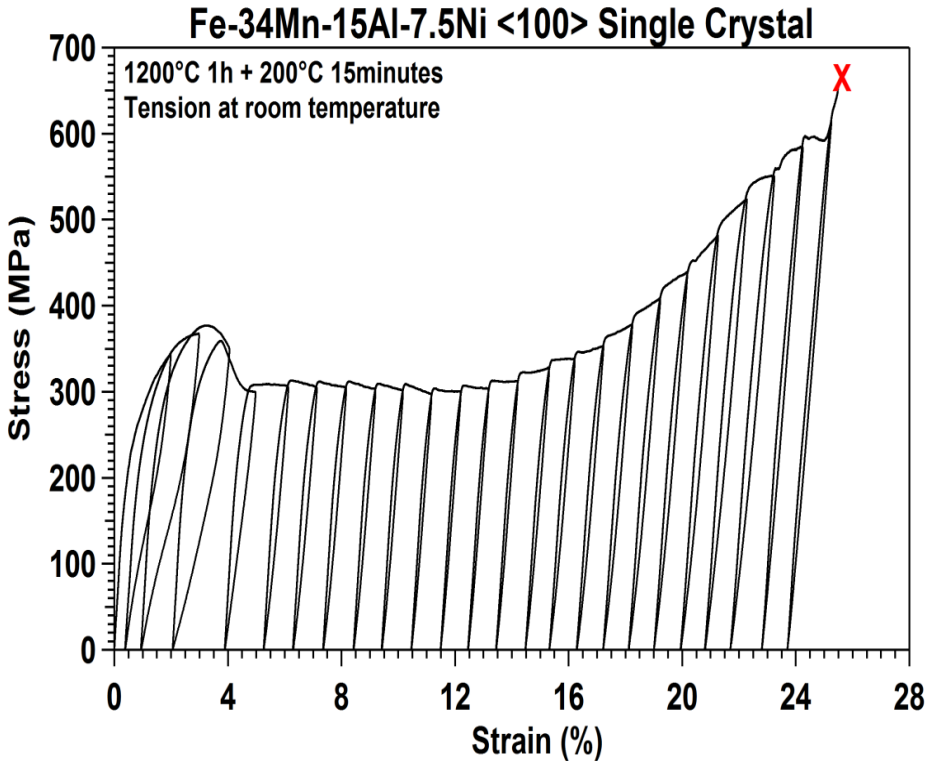

(a)

Figure 4.7 The strain dependence of the superelastic response of the $Fe_{43.5}Mn_{34}Al_{15}Ni_{7.5}$ single crystals oriented along the <100> direction under incremental tension loading at room temperature. (a) shows the stress-strain response. (b) recoverable strain and irrecoverable strain as a function of applied strain after each loading-unloading cycle. (c) is the optical microscopy image of the tension sample after the test shown in (a), taken on the sample surface. The image shows retained martensite on the sample (d) shows the phase map of the gauge section of the tension sample after incremental strain test at room temperature determined through EBSD. The red and green colors represent the martensite and austenite phases, respectively.

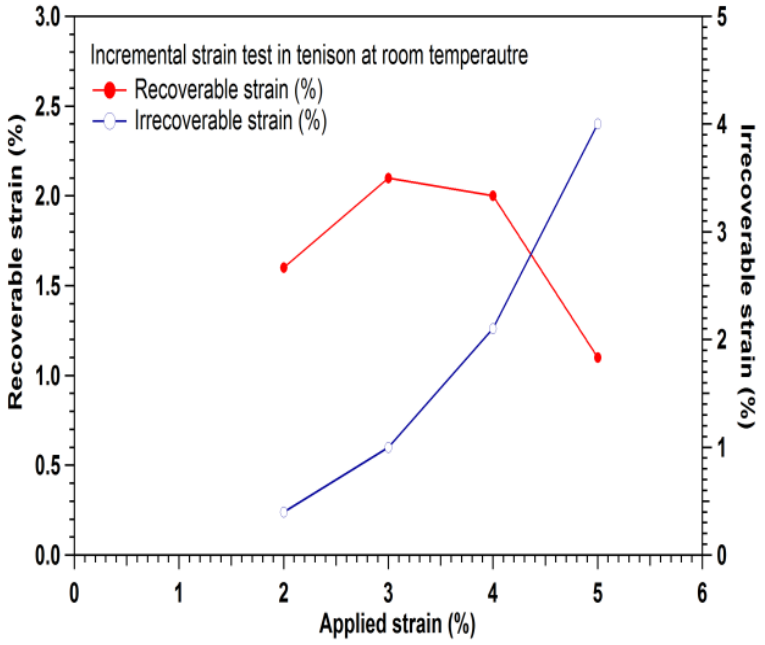

(b)

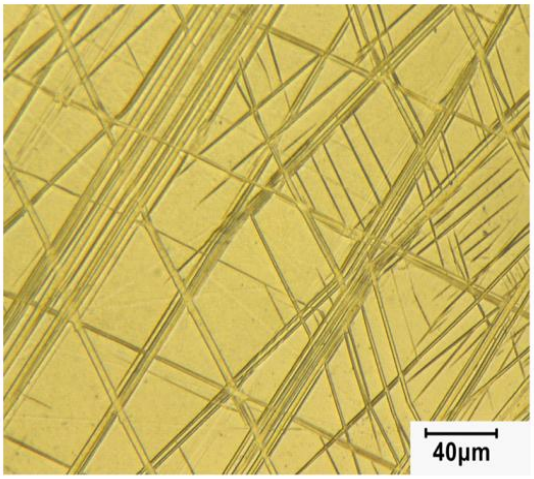

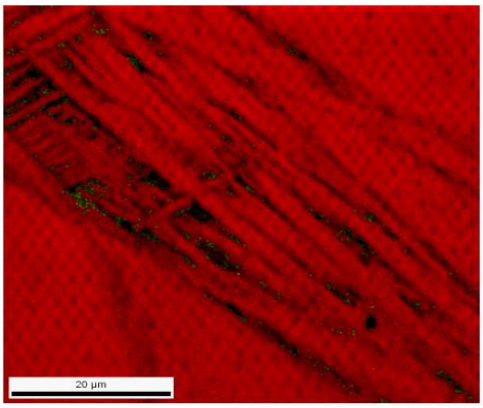

Phase	Total Fraction
Martensite	0.985
Austenite	0.011

(C) (d)

Figure 4.7 Continued.

From these result, it is clear that the superelastic response in tension is different than it is in compression. First, the tensile sample shows heavily retained martensite (90%) than the compression sample (60%). Second, although the transformation strains in the FeMnAlNi single crystals along the [100] orientation are 26.5% in tension and 10.5% in compression from the theoretical calculation, the compressive sample shows higher recoverable strain than that in tension. In order to study the reasons behind these differences, a detailed TEM investigation is carried out in both compressive and tensile samples after the incremental strain experiments.

Bright field TEM image of the compression sample after the incremental strain test is shown in Figure 4.8a. The TEM images are taken at room temperature. Two martensite variants are observed in the compression sample. Figure 4.8b is the bright field TEM image showing two large martensite plates in the austenite matrix, and Figure 4.8c shows the high magnification TEM bright field image taken from one of the martensite plates in Figure 4.8c. The martensite plate contains a high density of thin plate-like structures, which were found to be nano-twins (Figure 4.8e). A similar martensite structure was observed by Omori et al. [109]. Figure 4.8d shows the corresponding SAED pattern from the area 1 in Figure 4.8c and can be identified as the fcc martensite structure. Few dislocations are observed at the austenite-martensite interface from TEM weak beam image, show in Figure 4.8f.

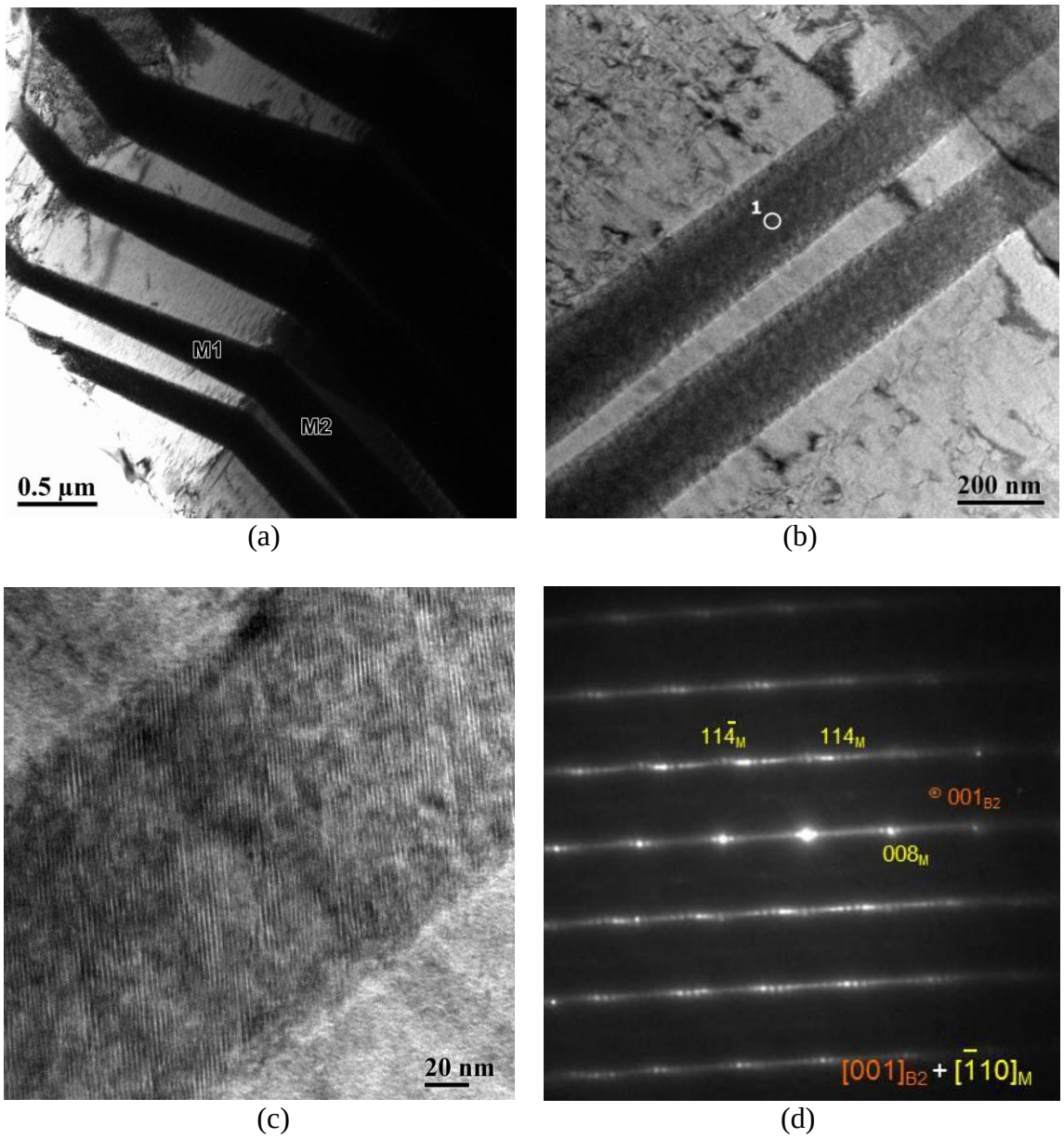

Figure 4.8: TEM microstructure of the $Fe_{43.5}Mn_{34}Al_{15}Ni_{7.5}$ single crystalline compression sample after incremental-strain experiment at room temperature. (a) Bright field TEM image showing two martensite variants (M1 and M2) where the stress direction is perpendicular to the planes of the bright field TEM image. (b,c) TEM bright field images of retained martensite plates and (d) the diffraction pattern from area 1. (e) is a representative high resolution TEM image of the stress-induced martensite structure at room temperature showing nano-twinned structure. (f) TEM weak beam micrograph of compression sample after deformation to 6% strain at room temperature. Few parallel dislocations appear near the austenite-martensite boundary.

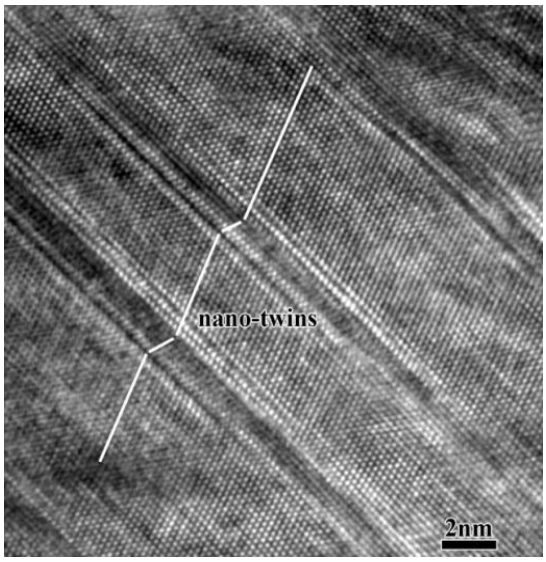

(e)

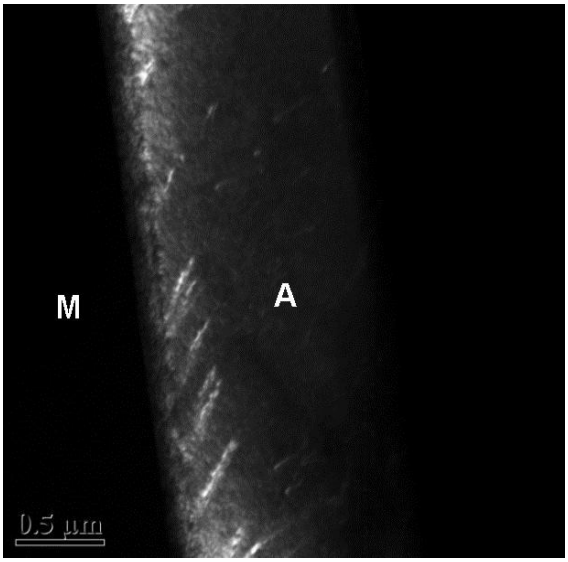

(f)

Figure 4.8 Continued

Figure 4.9a displays the room temperature bright field TEM image of the tensile sample after the incremental strain experiment shown in Figure 4.7a. The TEM image reveals retained martensite and twinned martensite structure in the sample. Only one martensite lattice correspondence variant could be observed from the TEM image and the matching SAED pattern (Figure 4.9c). The twin boundary shown in Figure 4.9b is found to be {111}<112> type, which corresponds to typical deformation twins in fcc crystal structure. Because the tension sample after the completion of incremental strain test (tested to failure) is almost fully martensitic, it is difficult to locate the martensite-austenite interface. Therefore, we performed an additional experiment where a tensile sample was strained to 8% instead, such that the transformation is not fully completed. Figure 4.9d is the bright field TEM image showing the martensite plates in the austenite matrix after the 8% deformation, and dislocations are observed at the austenite-

martensite boundary. The corresponding selected area diffraction patterns of area 1 and 2 are shown in Figures 4.9e and 4.9f, respectively, confirming area 1 to be the austenite phase while area 2 to be the martensite phase. Unlike the compression sample, distinct dislocation features are found to be in the austenite matrix as shown in Figure 4.9g (bright field TEM image) and Figure 4.9h (weak beam TEM image).

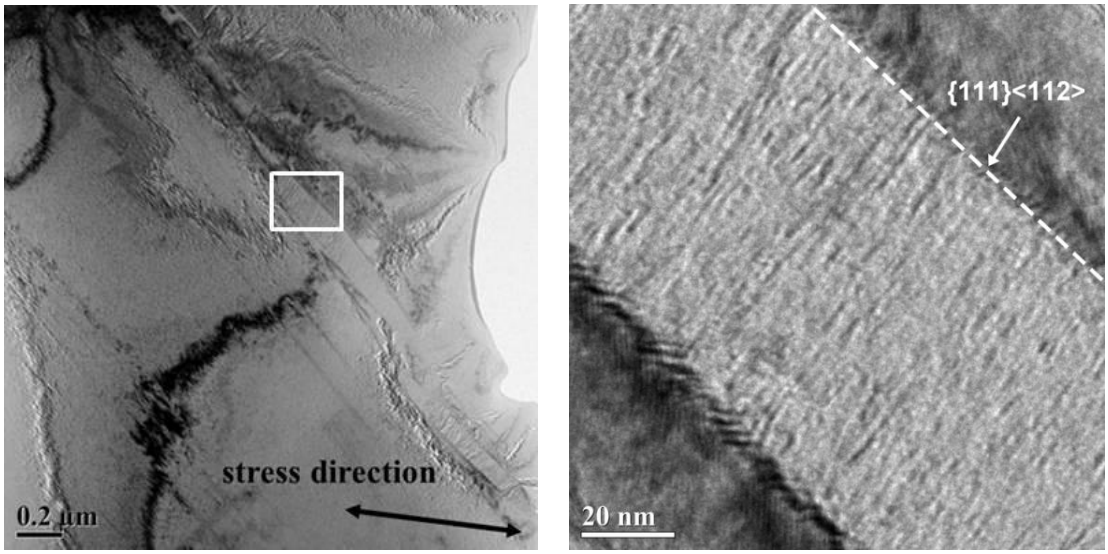

(a) (b)

Figure 4.9 (a) is the bright field TEM image and (b) is TEM image from the region shown in (a), of the tension sample after the incremental-strain experiment at room temperature, shown in Figure 6a. (c) is the corresponding SAED pattern for (b). (d) Bright field TEM microstructure of the tension sample after being deformed to 8% strain at room temperature showing parallel dislocations at the austenite-martensite interface. (e) and (f) are the corresponding SAED patterns of area 1 and area 2 in (d), respectively. (g) Bright field TEM image showing the hairpin-shaped dislocations. (h) TEM weak beam micrographs of the tension sample after deformation to 8% strain.

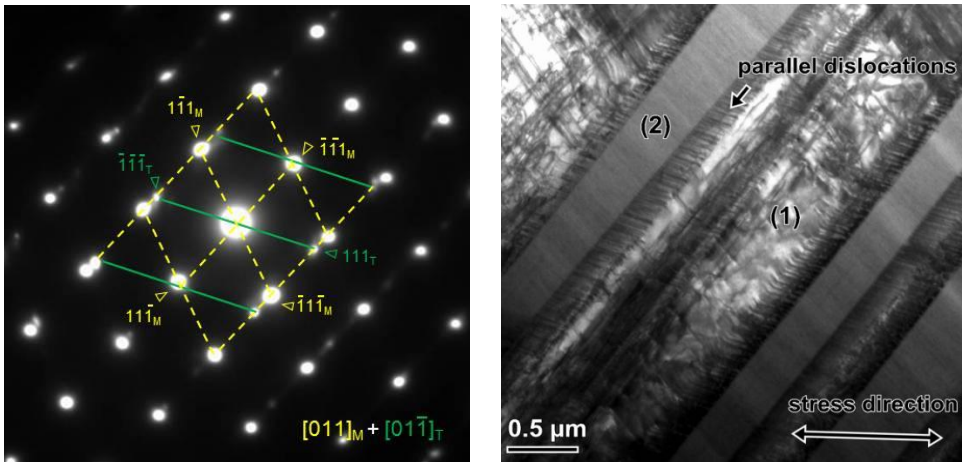

(c) (d)

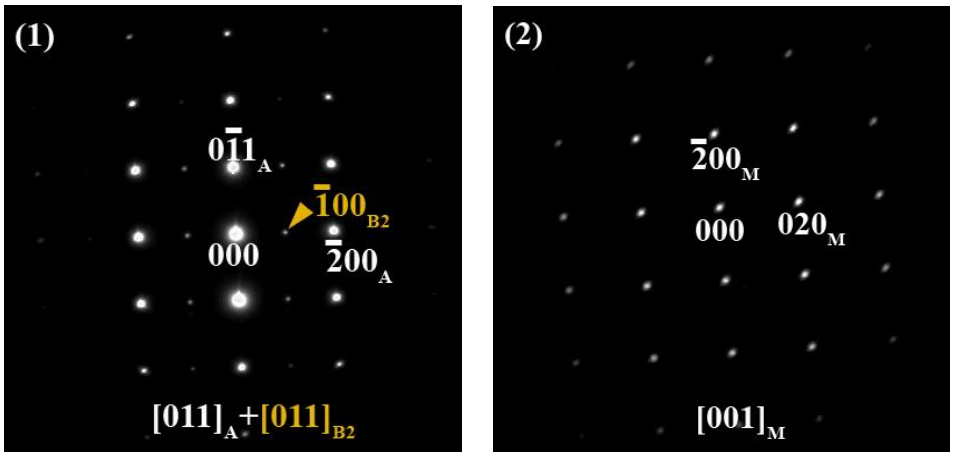

(e) (f)

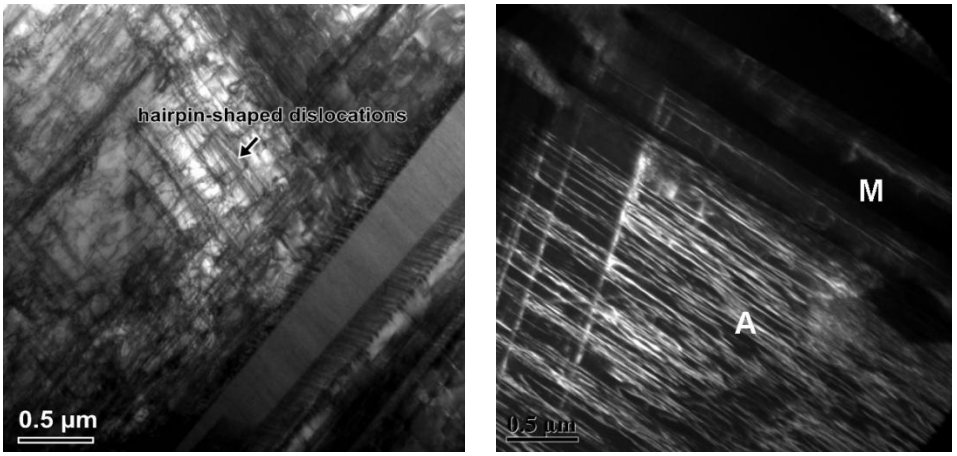

(g) (h)

Figure 4.9 Continued.

From above TEM results, there appears to be two types of dislocations in the tension samples. One is a series of short parallel dislocations seen at the austenite-martensite interface and the other is longer and observed in the austenite matrix. These two kinds of dislocations were also observed by Kikuchi et al. [123-125] in a FeNiCoTi shape memory alloy and were named parallel and hairpin-shaped dislocations, respectively. For the tension sample, the density of parallel dislocations at the austenite-martensite interface is very high, shown in Figure 4.9d. Kikuchi et al. [123-125] mentioned that these dislocations are formed to accommodate the lattice strain at the austenite-martensite interface in conjunction with nanotwins observed in the martensite. Since the refinement of martensite through twins is limited due to excessive interfacial energy generated by twin boundaries, parallel dislocations are formed in austenite as well with spacing comparable to the spacing of nanotwins in martensite. Furthermore, they report that the parallel dislocations do not appear to pin the martensite boundary, and the austenite-martensite interface remains mobile despite the presence of these dislocations. On the other hand, the hairpin-shaped dislocations coalesce together and form the dislocation loops in the austenite matrix, shown in Figure 4.9g and h. When the austenite is slip, the dislocations are trapped in the austenite matrix and caused the formation of hairpin-shaped dislocations [123-125]. Based on their studies, FeNiCoTi alloy does not show particularly good superelastic recovery due to formation high density of dislocations.

Moreover, we can see the differences of TEM micrographs in both tension and compression. (1) A high density of parallel dislocations at the austenite–martensite interface and hairpin-shaped dislocations in the austenite matrix are observed in the tension sample as shown in Figure 4.9d and g. However, only few parallel dislocations are observed in the compression sample. (2) The lattice invariant strain appears to be accommodated by a combination of the nanotwins in the martensite and the parallel dislocations [123-125]. (3) Only one martensite variant can be seen in the tension sample as show in Figure 4.9a and two martensite variants can be observed in the compression sample as shown in Figure 4.8a.

Based on above micrograph results, we can explain why the samples show a large irrecoverable strain in tension and better recovery in compression. Irrecoverable strain in both tension and compression are caused by retained martensite. Figure 4.8b shows two martensite plates remaining in the austenite matrix after the compression test. However, the sample is mostly martensite in the tensile sample after the test, shown in Figures 4.9a, b and c. The result indicates that the martensite is more heavily retained in the tensile sample than that in the compression sample. Figure 4.9d and g show high density of parallel dislocations at the austenite-martensite boundaries and hairpin-shaped dislocations in austenite matrix. On the contrary, parallel or hairpin-shaped dislocations are largely absent in the austenite matrix in the compression sample, shown in Figure 4.9a and b. While the parallel dislocations were reported to not negatively impact the mobility of the martensite-austenite interface [123-125], the longer hairpin dislocations may have this effect [126] and their presence may cause the martensite to be pinned.

Since we observe only martensite phase in the tensile sample, this suggests while the austenite transforms to the martensite, martensite does not transform back to the austenite. The reason is perhaps that the hairpin dislocations generated during transformation pin the martensite to prevent it from transforming back to the austenite. As a result, more martensite remains in the tensile sample and contribute to the large irrecoverable strain.

Although the irrecoverable strains in both tension and compression are caused by retained martensite, the difference in their recovery ratio is related to the volume fraction of the retained martensite. From the bright field TEM images of the tested specimens in Figure 4.8c and 4.9a, the as-tested compression sample shows a mixture of austenite and martensite, where the as-tested tension sample shows mostly martensite. Therefore, we suspect that a high volume fraction of martensite in the tensile sample is pinned by dislocations. The stabilized martensite cannot be transformed back by heating significantly above the austenite finish temperature. In order to test this hypothesis, we conducted a series of temperature vs. magnetization measurements under an applied magnetic field of 0.05 Tesla for the samples before and after the incremental strain tests, as shown in Figure 4.10a. The aged sample without testing indicate that the martenstie phase is weakly magnetic**.** When the compression sample after 10% applied strain was cycled from 130 °C to -260 °C under an applied magnetic field of 0.05 Tesla, the phase transformation is clearly visible and the response is similar to that of the untested sample. This indicates that some of the martensite is still reversible even after an applied strain of 10%. On the other hand, the SQUID profile of the sample after tension test does

not show any sign of transformation at all, and indicates that the martensite is pinned by dislocations and cannot be recovered just by heating to moderate temperatures. In addition, Figure 4.10b is the thermo-magnetization results under 7 Tesla showing that magnetization of the deformed tension sample is notably lower than that of the compression sample (both of which are significantly lower than that of the untested sample), which indicate both samples have large volume fractions of remnant martensite, but the compression sample should also have austenite phase. This is in agreement with Figures 4.9d and g, which shows the high density of dislocations generated and large volume fraction of martensite remained in the tensile samples.

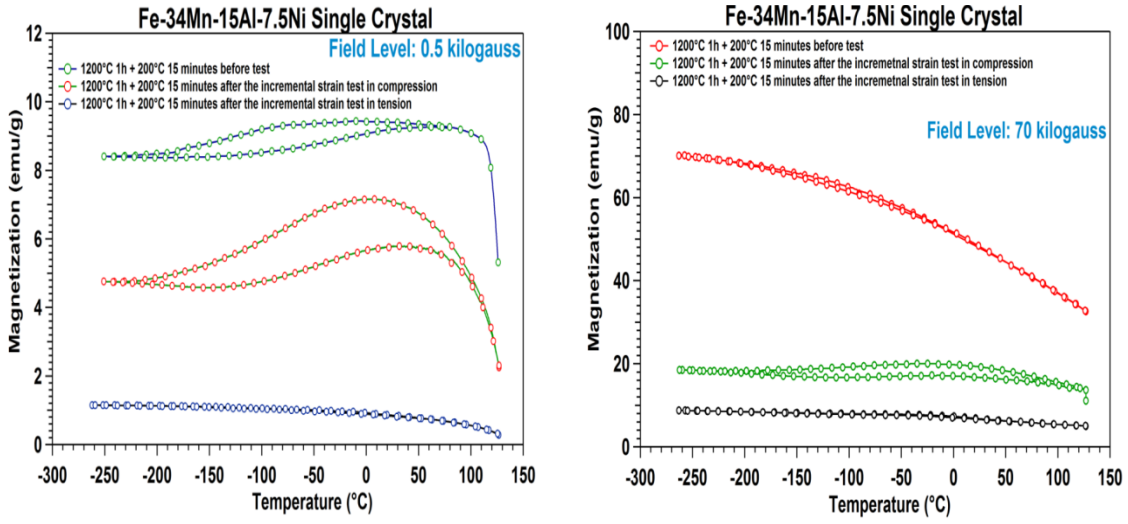

(a) (b)

Figure 4.10 Thermo-magnetization curves of the $Fe_{43.5}Mn_{34}Al_{15}Ni_{7.5}$ single crystalline samples aged at 200 °C for 15 minutes before the experiments and after the incremental strain tests at room temperature. The magnetic field is (a) 0.5kG and (b) 70 kG.

Additional systematic heating experiments conducted after each loading-unloading increments and recovery strains were measured under both tension and compression. In order to determine the maximum strain recovery in both tension and compression, the compressive and tensile samples were heated up to 160 °C and cooled down to room temperature after each loading-unloading cycle to obtain additional strain recovery (shape memory strain) from retained martensite after unloading. The same procedure was applied until the martensitic transformation is completed or no significant recovery after heating-cooling experiment. Figure 4.11a and b summarizes the total strain recovery (recoverable strain + shape memory strain) and irrecoverable strain as a function of applied strain in both compression and tension. Compare to Figure 4.6b and 4.7b results, it is seen that while significant strain recovery occurs after re-heating in compression at all applied strain levels, full recovery was not observed. The reason for the lack of full recovery is possibly related to the short aging time, which does not sufficiently strengthen the alloy against plastic deformation; plastic deformation accompanies martensitic transformation also under compression, and the heating temperature is not sufficient to unpin all remnant martensite plates. In contrast, the strain recovery from heating is much lower in the tension sample, and becomes negligible after 5% applied strain. The results support the above arguments, where the compression samples demonstrate more shape memory recovery than the tension samples.

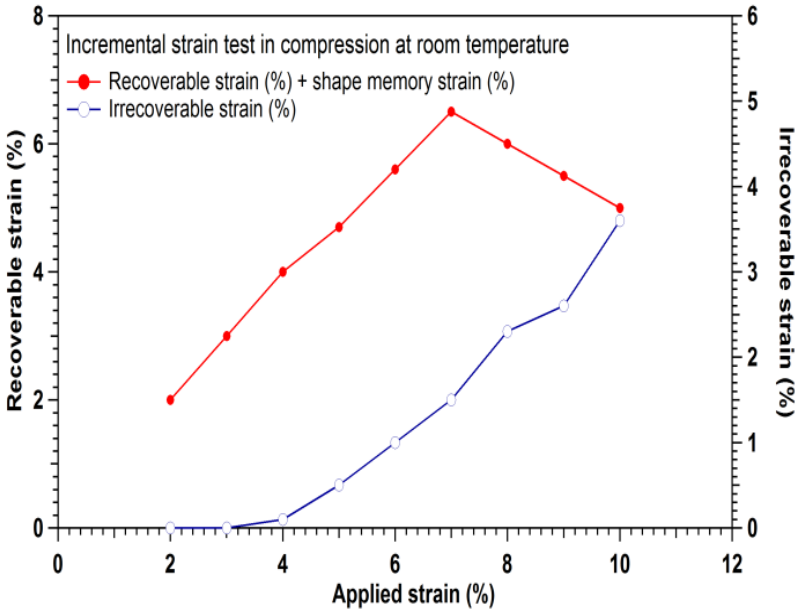

(a)

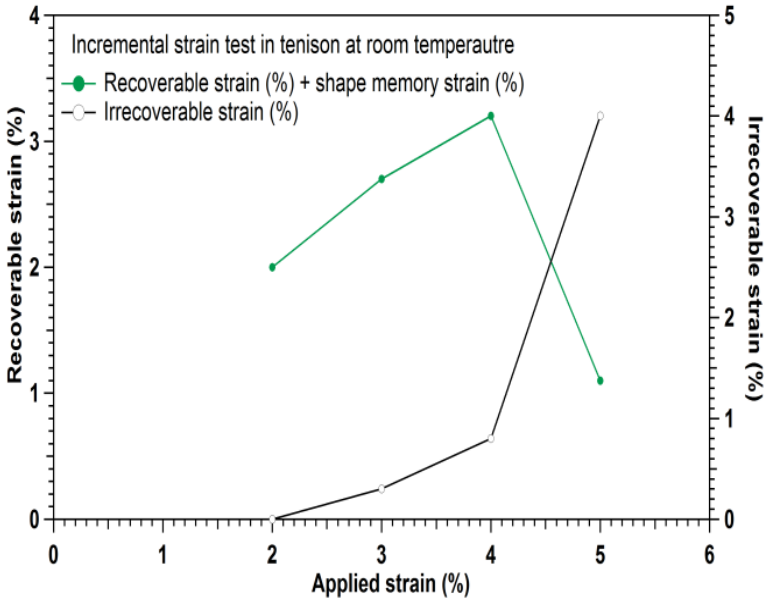

(b)

Figure 4.11 The recoverable stain plus shape memory strain and irrecoverable strain as a function of applied strain in (a) compression and (b) tension.

Moreover, the retained martensite cannot be free by heating to higher temperature in tension sample, indicates the irrecoverable strain cannot be recover by heating to higher temperature based on the figure 4.11b results. The results suggest the tension sample shows the poor recoverable strain is not due to insufficient test temperature. Even if the samples test in higher temperature, the similar stress-strain response will also observe in the high test temperature. In order to prove the irrecoverable strain in the tensile sample is caused by the dislocations instead of insufficient test temperature, we performed the incremental strain tensile test at 160°C, shown in Figure 4.12. From the result, we can see the similar tensile stress-strain response at higher test temperature compare to the incremental strain test result at room temperature, shown in Figure 4.7a. The result indicates the retained martensite is pinned by dislocations and cannot be reverse to austenite in higher test temperature.

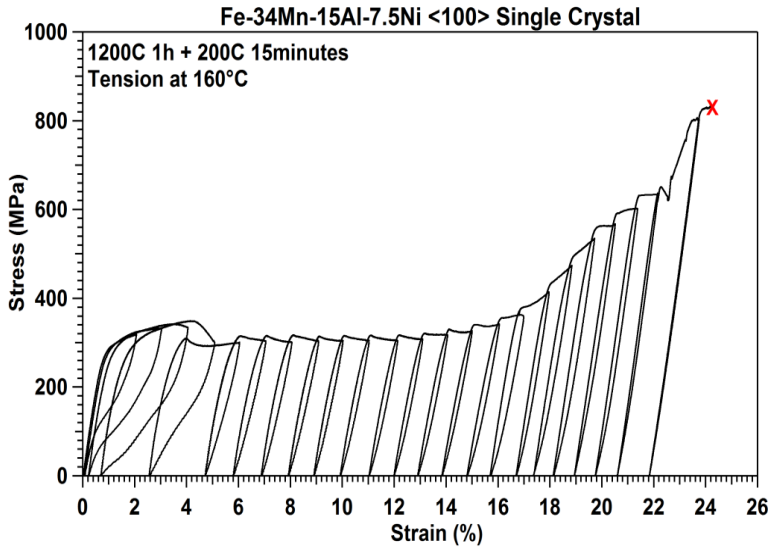

Figure 4.12 The superelastic response of FeMnAlNi shape memory single crystals oriented along the <100> direction under incremental tension strain at 160°C, stress and strain curve "X" refers to the fracture of the samples.

We believe that this difference in the superelastic response in tension and compression is also caused by the number of martensite variants activated during stress-induced martensitic transformation. As we mentioned in Section 2.5, there are three possible martensite variants in the fcc-bcc transformation. Figure 4.8a and Figure 4.9a show that there are two martensite variants present in the sample loaded in compression and only one martensite variant in the sample loaded in tension, respectively. In the compressive experiment along the [100] direction, two martensite variants can contribute equally to compressive strain. Consequently, the compression samples show better recoverability during the incremental strain test. However, only one martensite variant is capable to provide transformation strain in tension. As a result, hairpin-shaped dislocations may form and pin the martensite, and prevent them reverting back to the austenite, leading to large irrecoverable strain. Figures 4.9g also provide the evidence for this hypothesis as hairpin-shaped dislocations are clearly observed in the austenite matrix. However, the hairpin dislocation loops are not observed in the austenite matrix of the compression sample (Figure 4.7b). When the deformation in the tension sample increases, the fcc deformation twinning occurs in the martensite phase. Figure 4.9a and 9b provides the important evidence for this hypothesis shows the martensite and deformation twins in the tension sample after the incremental strain test. Although the inherent transformation strain is higher in tension, the lack of ability of the specimen to accommodate geometric incompatibilities results in large local defect generation, and thus, the lower recoverable strains in tension.

Furthermore, the difference in the number of active variants in compression and tension also contributes to the difference in the shape of the stress-strain curve and stress hysteresis. Two martensite variants can assist the compressive deformation; as a consequence, the onset of stress-induced transformation is followed by a gradual increase in stress with increasing strain as twinned martensite forms, and leading to a stress hysteresis around 200-300 MPa. On the contrary, the single martensite variant activated in tension deformation, result in the motion of a large, single-variant plate. The stress-strain response in tension resembles a nucleation-controlled transformation where upon the creation of martensite nuclei of sufficient size, it quickly propagates through the entire material and is accompanied by plastic deformation and the loss of stored elastic energy [127]. This leads to a very large stress hysteresis. No additional stress is needed once a nucleus of the critical size has formed until significant martensite-martensite interaction occurs. As a result, we observe the stress drop and long flat plateau region in tension.

In summary, irrecoverable strain in both tension and compression are caused by retained martensite. The tension sample has heavily retained martensite and poor recoverability due to formation of high density of dislocations at the austenite-martensite interface and in the austenite matrix. The difference in recovery rate, stress hysteresis, and the shape of the stress-strain curves, and nature and mobility of the retained martensite between the samples tested in tension and compression are related to the number of active martensite variants during deformation.

4.5 Summary and Conclusions

In the present work, we have investigated the superelastic response of the $Fe_{43.5}Mn_{34}Al_{15}Ni_{7.5}$ single crystals oriented along the [001] direction and aged at 200 °C for 15 minutes. Through the combination of the microstructure, thermo-magnetization, and superelasticity results, the main findings and conclusions can be summarized as follows:

1. In constant strain superelastic tests at various temperatures in both tension and compression, the superelastic responses of the single crystals show low values of stress-temperature slope under tension (0.54 MPa °C $^{-1}$) and compression (0.41 MPa °C $^{-1}$) over a wide temperature window between -80 °C and 160 °C. The small temperature dependence of the critical stress for the onset of martensitic transformation can allow this material to show superelasticity in a large range of temperatures with nearly temperature-invariant stress levels for the transformation.
2. In the incremental strain superelastic experiments at room temperature, the compressive samples show a small and smooth stress increase during loading and better recovery upon unloading than the tensile samples. On the contrary, the tensile samples display a Luders-type stress-strain behavior and large irrecoverable strain. The main reason for irrecoverable strain in both compression and tension is the retained martensite. The retained martensite cannot be easily recovered by heating significantly above austenite finish temperature due to pinning by dislocations. The TEM investigations of the

compression samples show a mixture of austenite and martensite phases with relatively smooth phase interfaces. No hairpin-shaped dislocations are observed in the austenite matrix. On the other hand, the sample deformed under tension is almost fully martensitic, high density of straight parallel dislocations and hairpin-shaped dislocations are visible at the austenite-martensite boundaries and in austenite matrix, respectively. These dislocations may be responsible for the reduction in recoverability by pinning the martensite phase.

3. Almost fully martensitic nature of the sample deformed under incremental tensile loading and two phase structure of the sample deformed under compression are also confirmed with the thermo-magnetization measurements. Since the austenite phase is ferromagnetic and the martensite phase is weakly magnetic, the magnetization of the deformed tension sample is considerably lower than the magnetization of the deformed compression sample due to the much higher volume fraction of remnant martensite in the deformed tension sample.
4. The difference in the number of active martensite variants also contributes to the difference in the superelastic responses under tension and compression. In compression, two martensite variants are able to accommodate the transformation strain arising from the phase transformation. In contrast to compression, only one variant provide the transformation strain in tension accommodate the tension deformation. Therefore, high density of

dislocations is generated and will limit the recoverability and amplify the hysteresis. The difference in stress hysteresis and shape of the stress-strain curves are also related to this difference in the number of active variants during the transformation.

CHAPTER V

EFFECT OF AGING ON MICROSTRUCTURE AND SUPERELASTICITY OF FeMnAlNi SHAPE MEMORY ALLOYS SINGLE CRYSTALS UNDER BOTH COMPRESSION AND TENSION

In our previous study, we characterized the superelastic response of the $Fe_{43.5}Mn_{34}Al_{15}Ni_{7.5}$ single crystal with [100] orientation under tension and compression because this orientation possessed the highest theoretical transformation strain in both tension (26.5%) and compression (10.5%) [10]. Although both tension and compression samples showed small values of stress-temperature slope (0.54 MPa°C $^{-1}$ in tension and 0.41 MPa°C $^{-1}$ in compression) [10], the recoverable superelastic strain in both tension and compression were considerable smaller than theoretical predictions, with the compression sample showing significantly better superelastic recovery than the tension sample. The asymmetry is likely caused by differences in the variant selection during the superelastic experiment. Two martensite variants are readily activated when the sample is compressed along the [100] orientations, this deformation can be easily accommodated. On the other hand, only one martensite variant can accommodate the tension deformation along [100] orientation, and as a result, the high density of parallel and hairpin shaped dislocations are generated at the austenite-martensite interface and in the austenite matrix, causing widespread retained martensite and poor superelastic recovery. In any case, a maximum obtainable superelastic strain of only 4.2% is in the aged compression sample, which is still much smaller than theoretical values. Aging

governed the stress-temperature phase diagram, stress hysteresis, critical stress for phase transformation and recoverable strain of the superelasticity. In contrast to the previous study where aging time is focused on one condition (200°C-0.25h), this chapter will aim to present in detail the effect of aging on the size, composition and volume fraction of precipitates and in turn, the effect of precipitate size and volume fraction on the transformation temperature, superelastic characteristics such as stress hysteresis, superelastic strain, critical stress for stress-induced martensitic transformation, and stress-temperature slope in the [100] oriented $Fe_{43.5}Mn_{34}Al_{15}Ni_{7.5}$ single crystals.

5.1 Effect of Aging on Microhardness and Transformation Temperatures

Figure 5.1 summarizes the effect of aging temperature and duration on the Vickers microhardness at room temperature for the FeMnAlNi single crystals along the [100] orientation. The hardness values were measured on the (100) face of single crystals. The data points in the figure are aging 0, 1, 3, 6, 10, 12 and 24 hours. It is clear that the hardness values of samples increase with increasing aging times due to increased precipitation hardening, although the increase under 300°C is much more significant to the increase under 200°C.

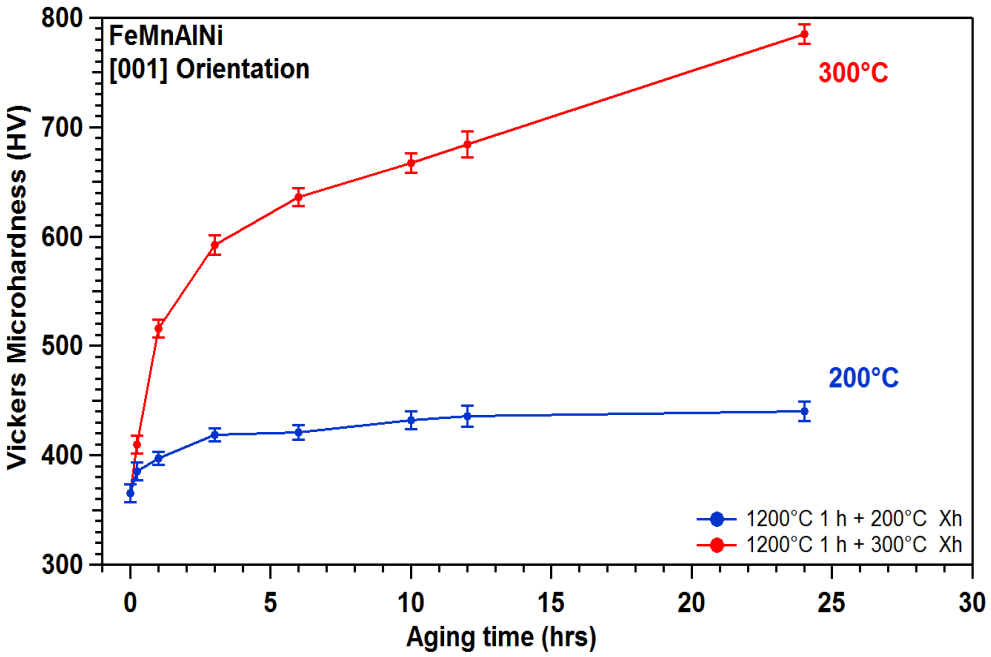

Figure 5.1 Vickers Microhardness in $Fe_{43.5}Mn_{34}Al_{15}Ni_{7.5}$ [001] single crystals aged at 200°C and 300°C for various durations.

Figure 5.2 displays the thermo-magnetization result of solution-treated FeMnAlNi single crystals. In this test, the sample was first heated up from room temperature to 130°C. After the test temperature reached 130°C, a magnetic field of 0.5 kG was applied and the sample was cool down to -260°C and heat up to 130°C under the applied field. Magnetization decreased during cooling and increased during heating, which suggest the austenite to be ferromagnetic while the martensite more weakly magnetic. We used the tangent line method to determine the transformation temperature as indicated in the figure. For the solution treated sample, the martensitic transformation temperatures were: austenite finish temperature (A_f) = 45°C, austenite start temperature (A_s) = -84°C, martensite start temperature (M_s) = -82°C, and martensite finish

temperature (M_f) = -210°C. The temperature hysteresis is defined as $|A_f - M_s|$, and was calculated to be of 127 °C. The same test was conducted for a FeMnAlNi single crystal aged at 200°C for 15 minutes, shown in previous chapter. The transformation temperatures of the aged single crystal were: A_f = 30°C , A_s = -93°C , M_s = -90°C and M_f = -213°C. The temperature hysteresis was 120°C. The result indicates the transformation temperature and temperature hysteresis tend to decrease after aging. Table 5.1 summaries the transformation temperatureS and thermal hysteresis of single crystals aged at 200°C for different times (from 0 to 48 hours) and 300°C for 1 hour. Long aging times or higher aging temperature will suppresses the thermoelastic martensitic transformation.

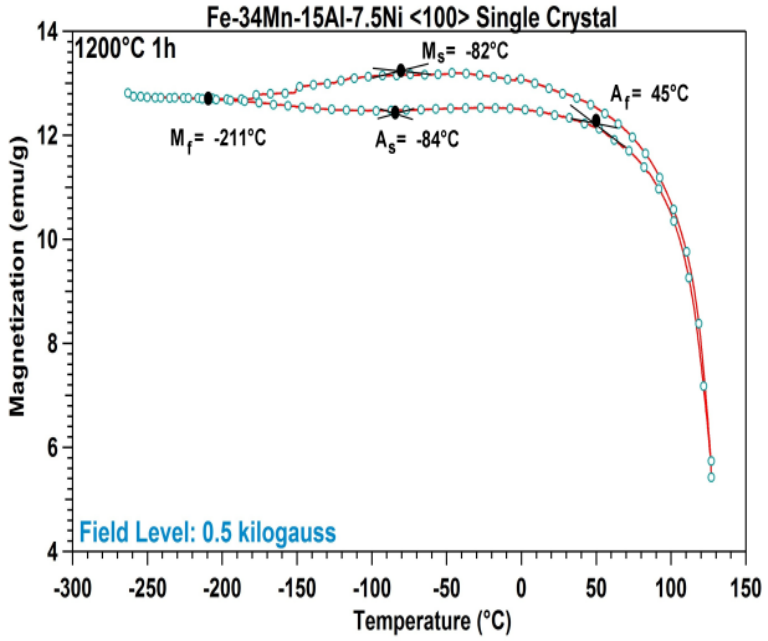

Figure 5.2 Thermomagnetization curves of the $Fe_{43.5}Mn_{34}Al_{15}Ni_{7.5}$ single crystals solution heat treated at 1200°C for 1 hour in a magnetic field of 0.5 kG.

Table 5.1 Summary of the transformation temperature and thermal hysteresis of the $Fe_{43.5}Mn_{34}Al_{15}Ni_{7.5}$ single crystals in different aging conditions.

	M_f (°C)	M_s (°C)	A_s (°C)	A_f (°C)	Thermal hysteresis (°C)
1200°C,1h	-210°C	-85°C	-84°C	45°C	127°C
1200°C,1h + 200°C-0.25h	-213°C	-90°C	-93°C	30°C	120°C
1200°C,1h + 200°C-1, 3, 6, 12, 24 and 48h	-	-	-	-	-
1200°C,1h + 300°C-1h	-	-	-	-	-

5.2 Effect of Aging on Size, Volume Fraction and Composition of Precipitates

5.2.1 TEM Investigation of Precipitates

Figure 5.3a shows the selected area diffraction (SAD) pattern of the single crystal solution treated at 1200°C for 1 hour. The diffraction pattern indicates that the austenite, precipitates and martensite are of the disordered bcc (A2) structure, ordered bcc (B2) structure and disordered fcc structure, respectively. The diffraction pattern also shows the $[001]_{BCC} \parallel [001]_{FCC}$ Kurdjumov-Sachs (K-S) relationship. It is important to note that signs of precipitates are observed in a solution-treated sample, indicating a rapid formation during the quenching process. However, it is difficult to see the precipitates form the bright field and dark field TEM images due to their small size and their existence could only be detected from the diffraction pattern result. Figure 5.3b shows the high resolution bright field TEM images at different aging times, and figure 5.3c summaries the relationship between precipitate size and aging times at 200°C. When the aging time is 1 hour, the precipitate size is around 3-6 nm and increases to 6-10 nm at 3 hours and 12-15 nm at 10 hours. Comparatively, the precipitate size for 300°C-1h aged sample is about 20-25 nm. The result indicates the size of precipitates increase with increasing the aging times and temperature. These values are comparable to the reported values of ~10 nm for FeMnAlNi polycrystals aged at 200°C for 15 minutes [109]. In comparison, the precipitate size of FeNiCoTi SMAs was reported to be around 20 ~ 25 nm in a sample aged at 600°C for 85minutes [35].In FeNiCoAlTa single crystals, the precipitate size increases with increasing the aging times form 600°C-7h to 600°C-90h. The precipitate size is around 5 nm in 600°C-90h aged sample [28].

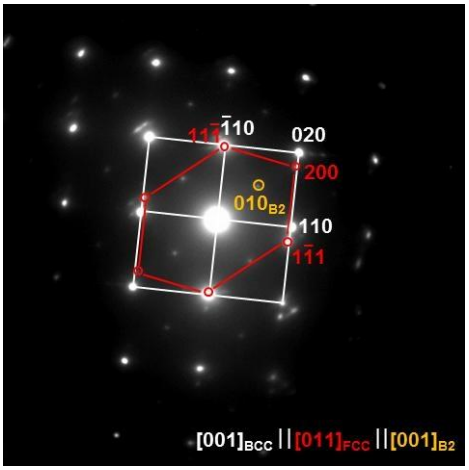

(a)

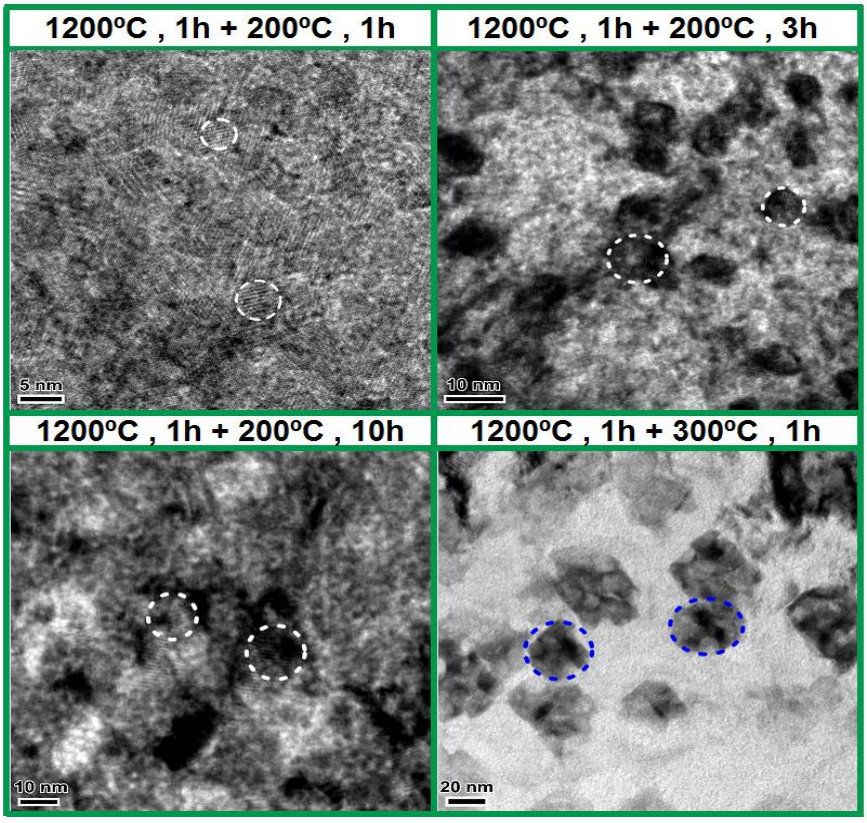

(b)

Figure 5.3 (a) The diffraction pattern of the FeMnAlNi [001] oriented single crystals solution heat treated at 1200°C for 1 hour. (b) The High resolution TEM images of the B2 precipitates in the FeMnAlNi single crystal SMA for different aging times. The size of precipitates was shown in the circle. (c) The relation between the precipitate size and aging times.

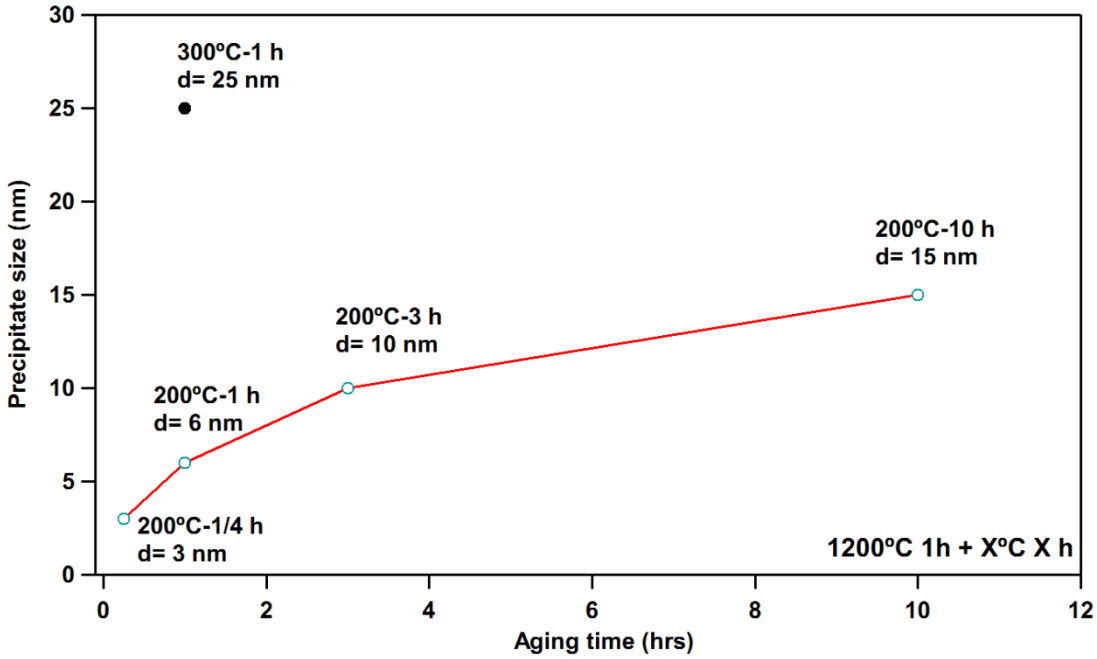

(c)

Figure 5.3 Continued.

5.2.2 Atom Probe Tomography Analysis of Precipitates

Atom probe tomography was performed on three, separate aging conditions: 200°C-1h, 200°C-3h, and 300°C-1h. Figure 5.4a and b show the Fe ions along with Ni isoconcentration surfaces used to delineate the precipitates from the matrix for the 200°C-1h and 200°C-3h samples. The precipitate volume fraction of the 200°C-1h sample was determined to be 29.8% using the procedure outlined in Ref. [128] with an approximate precipitate number density of 3.43 ± 0.69 x 10^{23} m^{-3}. The precipitates appear to be spherical in shape. Applying the same analysis technique to the 200°C-3h sample, its precipitate volume fraction was determined to be 34.3% with an approximate precipitate number density of 2.07 ± 0.24 x 10^{23} m^{-3}. For this condition, the precipitate

shape appears to be more plate-like with one axis becoming elongated. The increase in volume fraction and decrease in number density from the 1 hour to 3 hours aged sample indicates growth of the precipitates is occurring and nucleation has concluded. Figure 5c shows the Fe ions along with Ni isoconcentration surfaces used to delineate the precipitates from the matrix for the 300°C-1h samples. Analysis of this condition yielded a precipitate volume fraction of 30.6% with an approximate precipitate number density of 3.05 ± 0.61 x 10^{23} m^{-3}. Additionally, the precipitate are of an oblate spindle type shape opposed to the spherical precipitates seen in the 200°C-1h sample.

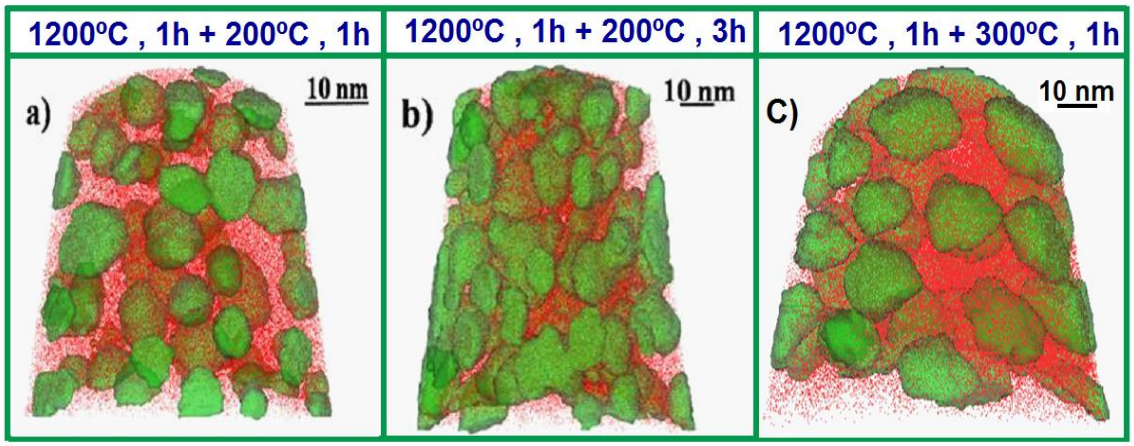

Figure 5.4 Atom probe tomography analysis of the B2 precipitates in the FeMnAlNi SMAs aged at 200°C and 300°C. Atom probe reconstruction image for the (a) 200°C-1h (b) 200°C-3h and (c) 300°C-1h samples.

The corresponding proximity histogram for the 200°C-1h, 200°C-3h, and 300°C-1h specimen were generated from 36.20% Fe, 37.85%Fe and 39.00% Fe isoconcentration surfaces respectively, an example of the result is shown in Figure 5.5 for 200°C-1h sample. The proximity histograms for both conditions clearly show an

enrichment of Ni and Al in the precipitate from their respective levels in the matrix, while Fe is strongly segregated to the matrix and Mn to a lesser degree. This observation of Ni-rich precipitates has been observed several other material systems: FeNiCoAlTaB and FeNiCoTi [23, 24]. The numeric values for precipitate compositions are reported in Table 5.2.

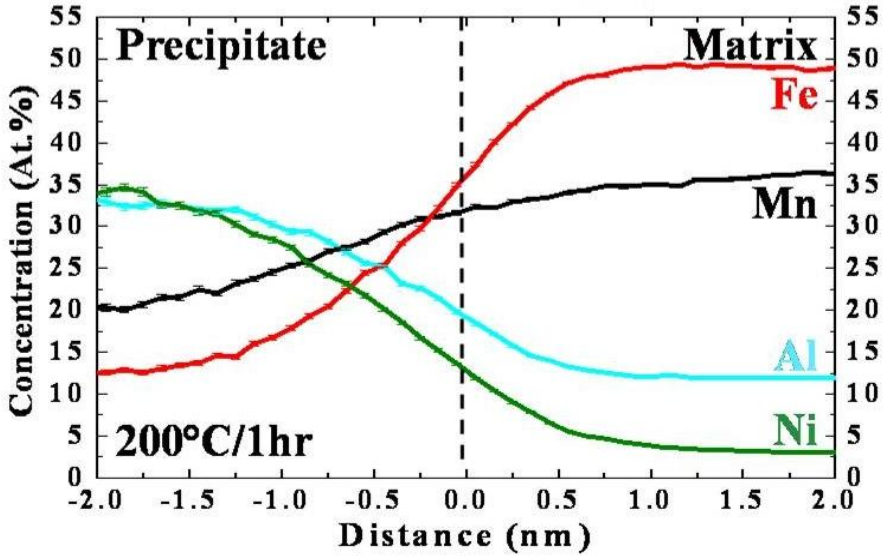

Figure 5.5 Proximity histogram taken across the precipitate and matrix boundary for the 200°C-1h aged sample.

Table 5.2 Matrix and precipitate compositions determined from atom probe tomography measurements for the 200°C-1h, 200°C-3h and 300°C-1h aged samples.

	Matrix Composition (at.%)			**Precipitate Composition (at.%)**		
	200°C-1h	**200°C-3h**	**300°C-1h**	**200°C-1h**	**200°C-3h**	**300°C-1h**
Fe	43.54 ± 0.07	43.61 ± 0.32	43.75 ± 0.22	22.03 ± 1.48	25.05 ± 3.05	26.07 ± 1.97
Mn	34.04 ± 0.03	34.09 ± 0.14	34.1 ± 0.09	25.69 ± 1.45	27.54 ± 1.02	25.92 ± 0.98
Al	14.96 ± 0.04	15.03 ± 0.16	14.9 ± 0.13	27.20 ± 1.19	23.70 ± 1.54	21.04 ± 1.44
Ni	7.45 ± 0.06	7.27 ± 0.30	7.24 ± 0.17	25.11 ± 1.50	23.70 ± 2.72	19.29 ± 2.04

From the results shown in table 5.2, changes in the aging heat treatment times and temperature slightly alters the composition of the precipitates: the Ni and Al content in the precipitate decrease with increasing the aging times and temperature, while the Fe content increase. The change composition of precipitate alters the composition of the matrix, which may affect the transformation temperatures.

Based on the microhardness, TEM and APT results, Table 5.3 summarizes Vickers microhardness, precipitate size and precipitate volume fraction in 200°C-1h sample and 300°C-1h samples. From the result, the hardness values in 300°C-1h sample is almost four times higher than 200°C-1h sample. Since the volume fraction of precipitates in these two aging samples is similar: the result suggests the changes in the hardness values of the aging temperature of 300°C are closely related to change in the size of the B2 precipitates instead of differences in the volume fraction.

Table 5.3 Summary of the microhardness, precipitate size and volume fracton in 200°C-1h and 300°C-1h samples.

Aging conditions	Micro hardness	Precipitate size	Precipitate volume fraction
200°C-1h	380 HV	3-6 nm	29.8%
300°C-1h	520 HV	20-25 nm	30.6%

5.3 Effects of Aging on Superelasticity in Compression

5.3.1 Constant-Strain Superelastic Experiments and Critical Stress-Temperature Phase Diagram

In order to investigate the effect of aging times and temperature on the stress-temperature phase diagram, the single crystal samples with [100] orientation were aged at 200°C for different times and also at 300°C for 1 hours. The compression specimens were loaded to 2% strain at various temperatures between -80°C and 160°C. Further increase in the test temperature causes precipitation during the experiment, which increases the critical stress values. Figure 5.6a, b, c, d, e and f show the constant superelastic test at various temperatures in different aging conditions.

A linearly relationship between critical stress and testing temperature was summarized in Figure 5.7 for the single crystal sample aged at 200 °C for 0, 1, 3, 6 and 10 hours and at 300 °C for 1 hour under compression. The linear stress-temperatures curves can be described by the Clausius-Clapeyron relationship, shown in equation 2.7. From the compressive result, the slopes for solution heat treatment, 200°C-3h and 200°C-10h samples are 0.52, 0.38 and 0.3 MPa/°C, respectively. For 300°C-1h sample, the slope is about 0.3 MPa/°C. It is clear that at the same test temperature, the critical stresses increase with increasing aging time, which indicates that transformation temperatures of the alloy are decreased with increasing aging treatment time. At the same test temperature (ex. -80°C), the critical stress for 300°C-1h sample about 1100MPa is higher than that in the 200°C-1h sample about 200MPa. Since the precipitate volume fraction of the sample is not appreciably increased from 200°C-1h to

300°C-1h, it is likely that transformation temperatures are primarily influenced by the size and composition of the precipitates.

Similar trend in aging time vs. transformation temperature was reported in FeNiCoTi SMAs. Increasing the aging times at 550°C or at 600°C caused the transformation temperature to increase, which corresponded with an increase in the superelastic critical stress under compression [37,38]. In contrast, the superelastic critical stress and the values of stress-temperature slope of the FeNiCoAlTa SMAs decreases in both tension and compression when the aging times increase from 7 hours to 90 hours at 600°C [40].

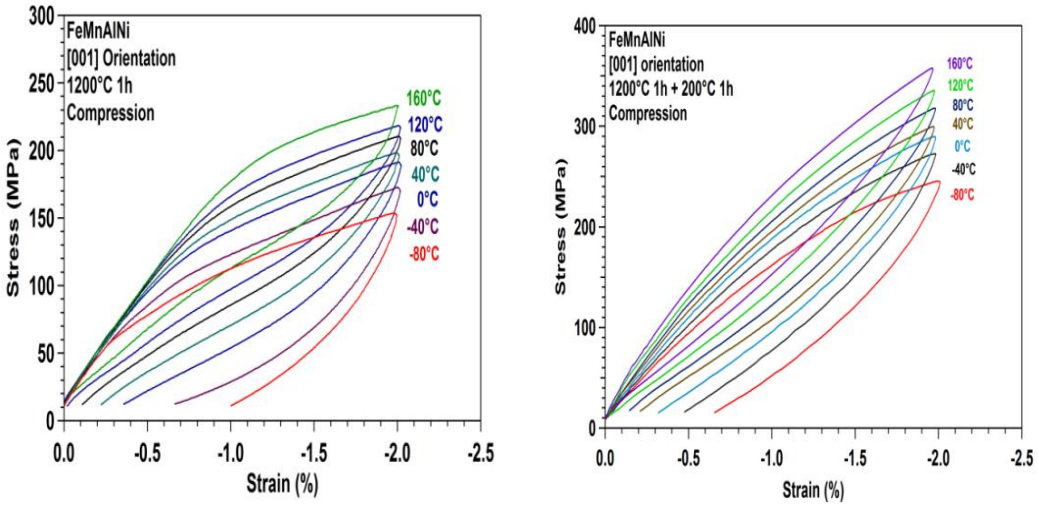

Figure 5.6 The constant strain superelastic experiment: the $Fe_{43.5}Mn_{34}Al_{15}Ni_{7.5}$ [100] single crystal specimens were solution heat treated at 1200°C for 1 hour and aged at different aging conditions. (a) 200°C-0h (b) 200°C-1h (c) 200°C-3h (d) 200°C-6h (e) 200°C-10h and (f) 300°C-1h. The specimens were loaded in compression at various temperatures to approximately 2% strain.

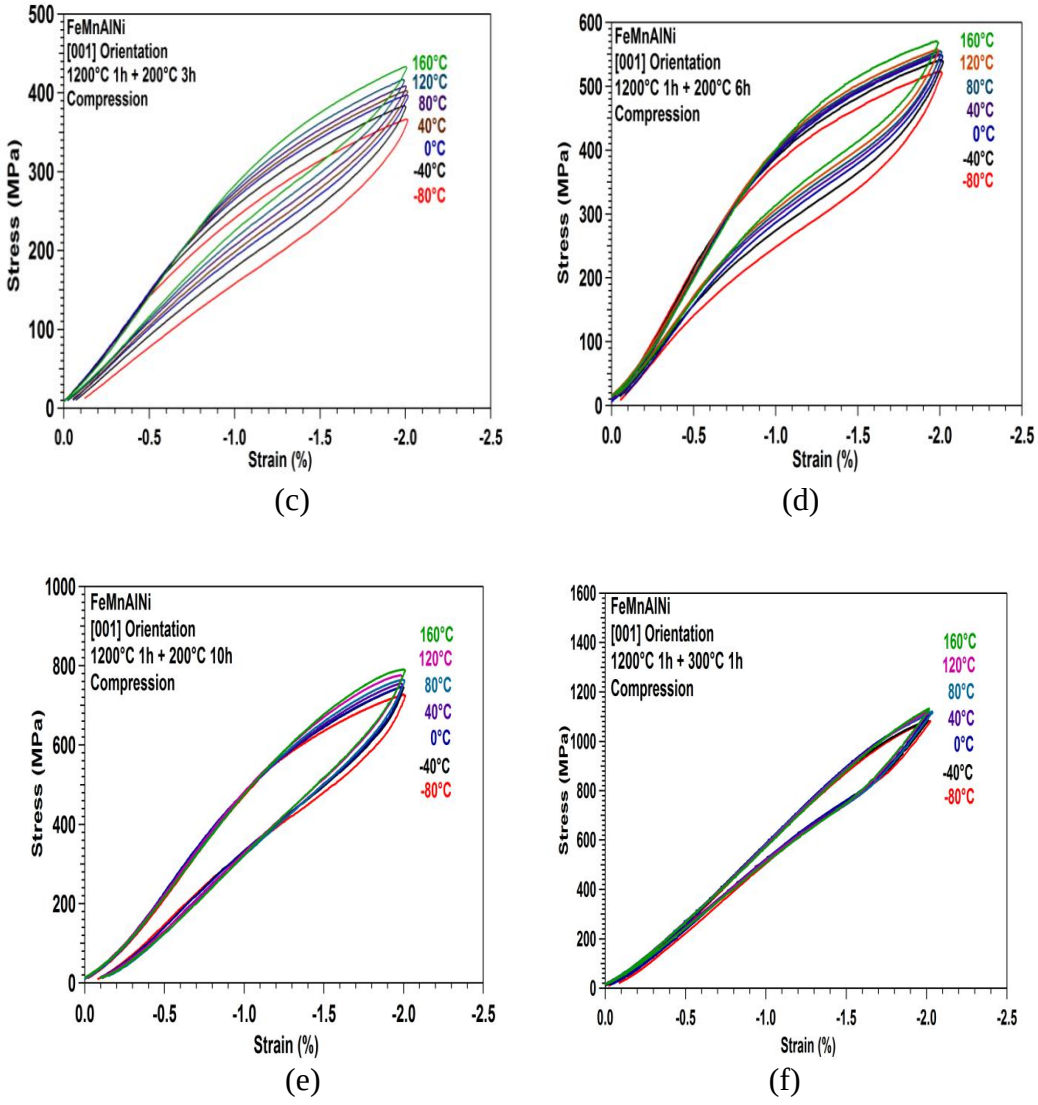

Figure 5.6 Continued.

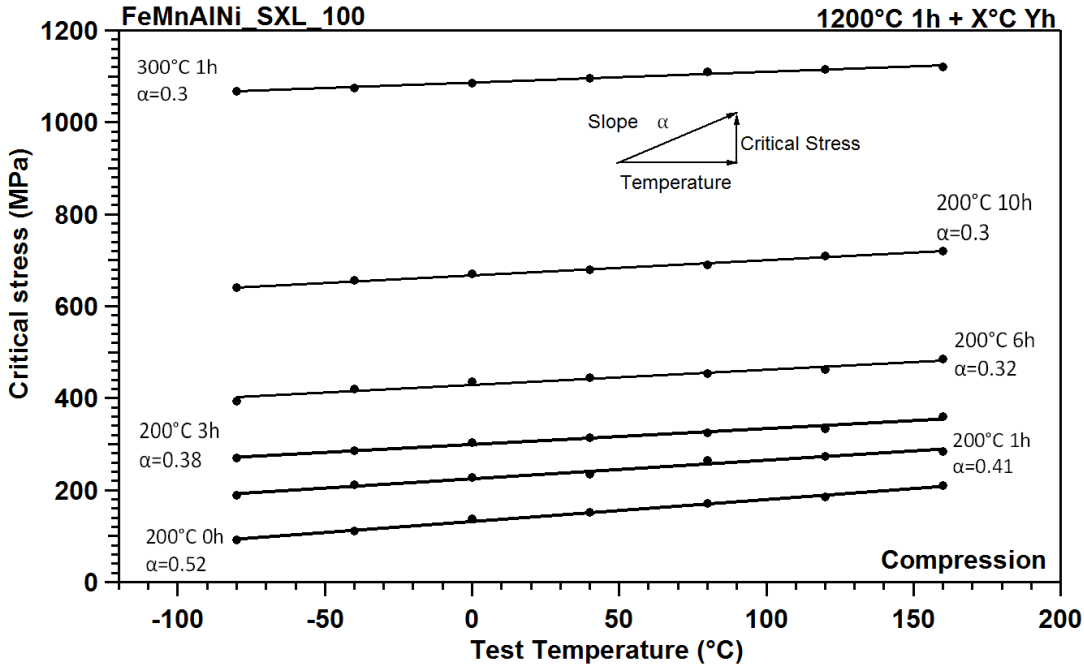

Figure 5.7 Summary of the critical stress for stress-induced martensitic transformations under compression in [100] oriented $Fe_{43.5}Mn_{34}Al_{15}Ni_{7.5}$ single crystals heat treated at 200°C for different times and 300°C for 1 hour. The results were determined from constant strain superelastic experiments at different temperature shown in Figure 5.6.

5.3.2 Incremental-Strain Experiments and Superelastic Strain

In the incremental strain test, experiments were carried out at room temperature under compression. The sample was loaded to 2% strain and unloaded. Subsequently, the cyclic loading was increased at 1% strain increments until the specimen showed significant hardening after the transformation plateau region. Figure 5.8a, b, c, d, e and f show the stress-strain curves of $Fe_{43.5}Mn_{34}Al_{15}Ni_{7.5}$ [100] single crystal specimen aged at 200°C for 0, 1, 3, 6, 10 hours and 300°C for 1 hour. For the 300°C-1h samples, cracks appeared in the sample during the 6% applied strain cycle and the test was stopped.

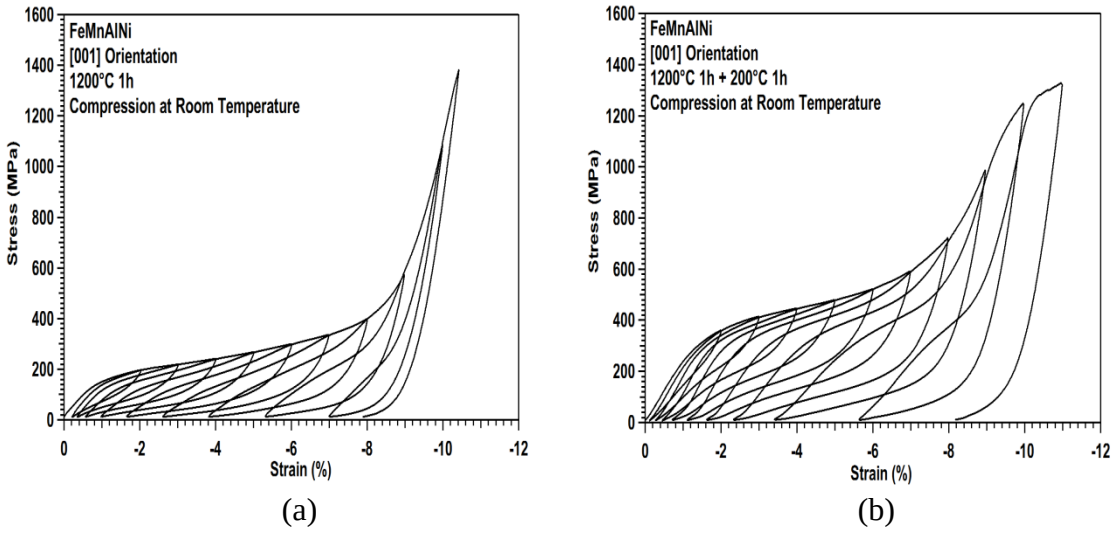

Figure 5.8 Incremental strain superelastic test in $Fe_{43.5}Mn_{34}Al_{15}Ni_{7.5}$ [100] single crystal specimens solution heat treated at 1200°C for 1 hour and aged at 200°C for different times (a) 200°C-0h (b) 200°C-1h (c) 200°C-3h (d) 200°C-6h (e) 200°C-10h (f) 300°C-1h. The specimens were loaded in compression at various temperatures to approximately 2% strain. The experiments were conducted at room temperature

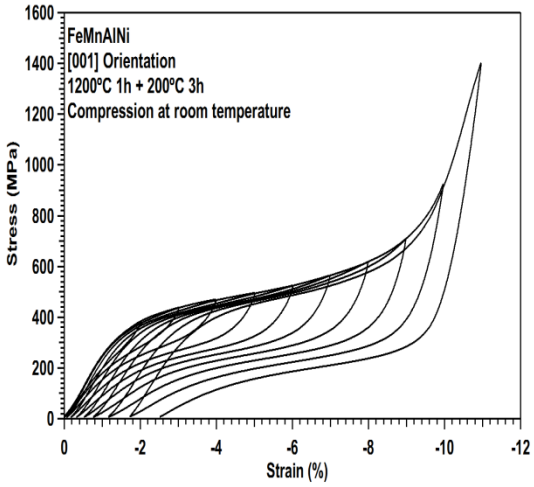

(c)

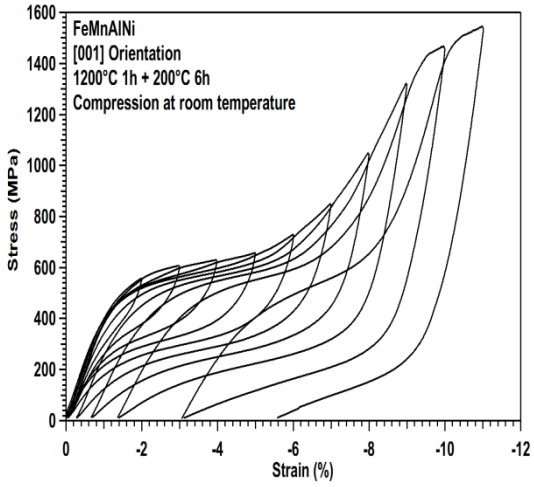

(d)

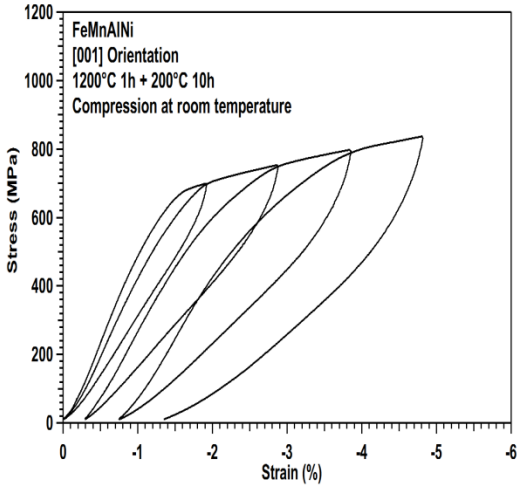

(e)

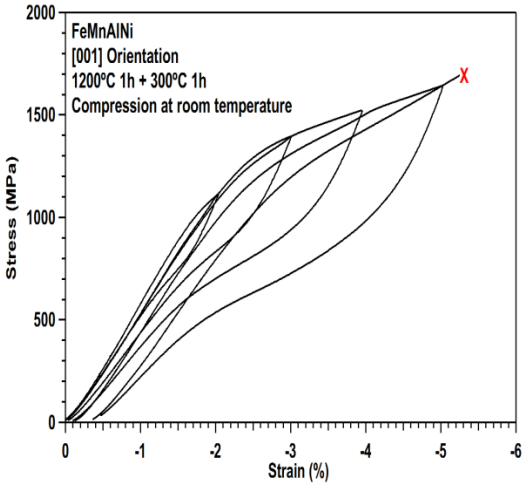

(f)

Figure 5.8 Continued

The superelastic strains and irrecoverable strain extracted from incremental strain test were plotted as a function of applied strain in Figure 5.9a. At low levels of applied strain, the maximum superelastic strain increases with increasing applied strain, gradually reaching a peak values beyond which maximum superelastic strain decreases with future applied strain. The maximum values of superelastic strain are defined as ε_{SE}^{MAX}. From this result, the maximum superelastic strains are about 3.6%, 5%, 7.2%, 6.3%, 2.5% and 2.2% for 200°C-0h, 200°C-1h, 200°C-3h, 200°C-6h, 200°C-10h and 300°C-1h, respectively. Figure 5.10 summaries the maximum superelastic strain similarly obtained from additional aging duration at 200°C. The results show that the maximum superelastic strain is obtained after aging at 200°C for 3 hours.

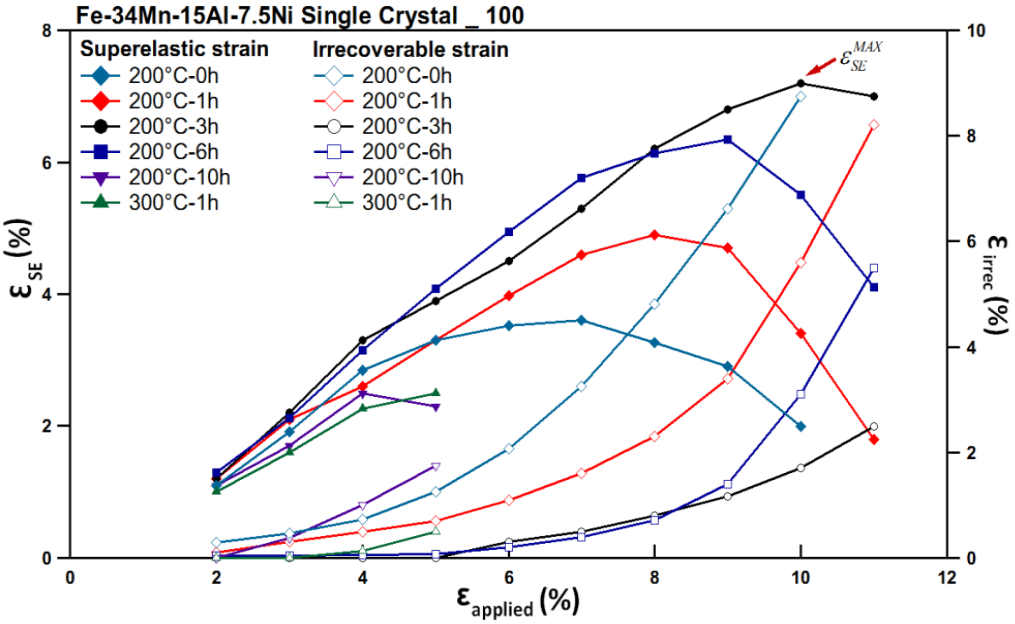

Figure 5.9 Variation of superelastic strain and irrecoverable strain with the applied strain in $Fe_{43.5}Mn_{34}Al_{15}Ni_{7.5}$ single crystal with the [100] orientation with various aging times.

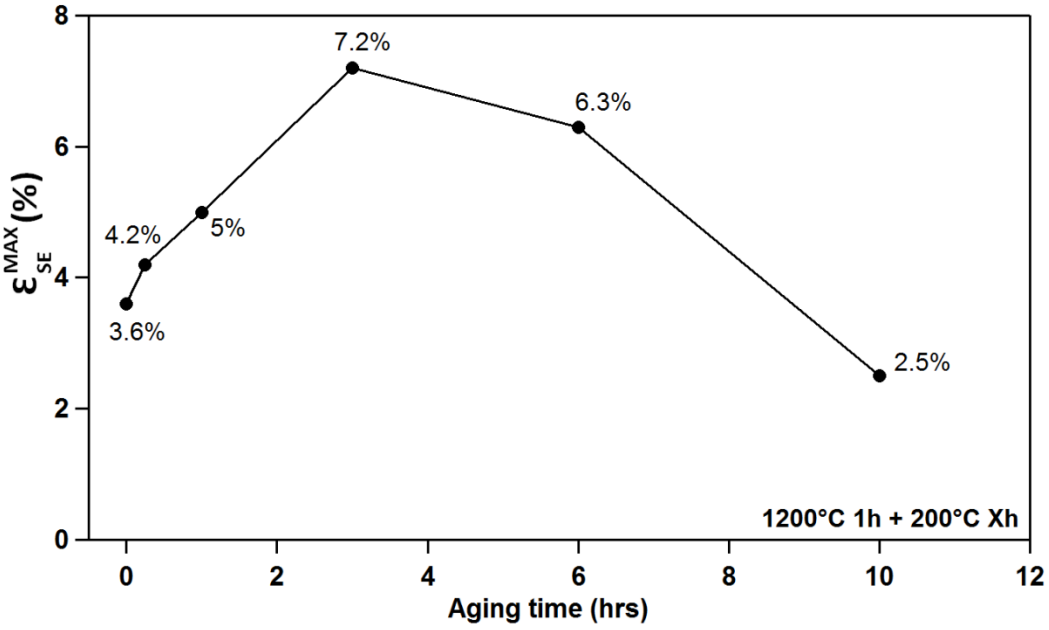

Figure 5.10 The maximum superelastic strain for the $Fe_{43.5}Mn_{34}Al_{15}Ni_{7.5}$ [100] orientation single crystals aged at 200 °C for different duration.

Based on the previously shown TEM, APT and superelastic results, larger precipitates were formed in the 300°C-1h sample compared to the 200°C-1h and 200°C-3h samples. The largest superelastic strain is obtained in the 200°C-3h sample with the precipitate size about 6- 10 nm and the volume fraction of precipitates around 34.3%. The volume fraction of precipitate in 200°C-1h sample is about 29.8%, which is closed to the 30.6% in 300°C-1h sample. However, the superelastic strain is considerably higher in the 200°C-1h sample than that of the 300°C-1h sample. Since the volume fraction of the precipitates in all three of these samples does not differ significantly (<5%), and the differences in the precipitate compositions are small and not are expected to create large differences in mechanical response, it is likely that the discrepancies in superelastic strain could be explained by differences in the size of non-transforming precipitates in the samples.

The effect of precipitate size is also apparent in the microhardness of the samples. Figure 5.11 summarizes Vickers hardness as a function of precipitates size for different aging times and temperature. It is clear that an increase in precipitate size drastically increases the hardness of the material without a concomitant increase in volume fraction for 200°C-1h and 300°C-1h sample. This again suggests that the size of precipitate has a significant effect on the mechanical and superelastic response of the alloy.

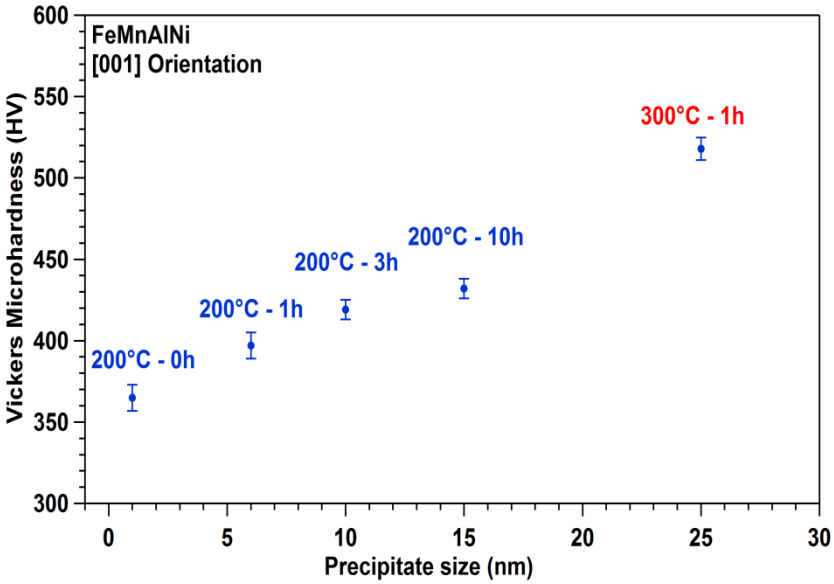

Figure 5.11 The relationship between the Vickers microhardness and precipitate size in $Fe_{43.5}Mn_{34}Al_{15}Ni_{7.5}$ single crystal with various aging times.

5.3.3 Precipitate Effect on Superelastic and Recoverable Strain

It is possible that the portions of the irrecoverable strain observed in the experiments shown in Figure 5.8 are caused by unrecovered martensite. This component is also a portion of total transformation strain and should be considered when comparing to theoretical values. For the three aforementioned aging conditions (200°C-1h, 200°C-3h, 300°C-1h), the specimen after the incremental strain experiment were heated to 100°C. Total strain recovery during heating was recorded and added to superelastic strain to as a measure to the total recoverable strain of the specimen, and plotted as a function of precipitate size in Figure 5.12. The result shows the maximum recoverable strains are about 6.2%, 7.3% and 3% for 200°C-1h, 200°C-3h and 300°C-1h, respectively. The stress hysteresis as a function of precipitate size is also plotted in this

Figure 5.12. The stress hysteresis is determined from the 5% applied strain. We will discuss the relationship between the stress hysteresis and precipitate size in the next section.

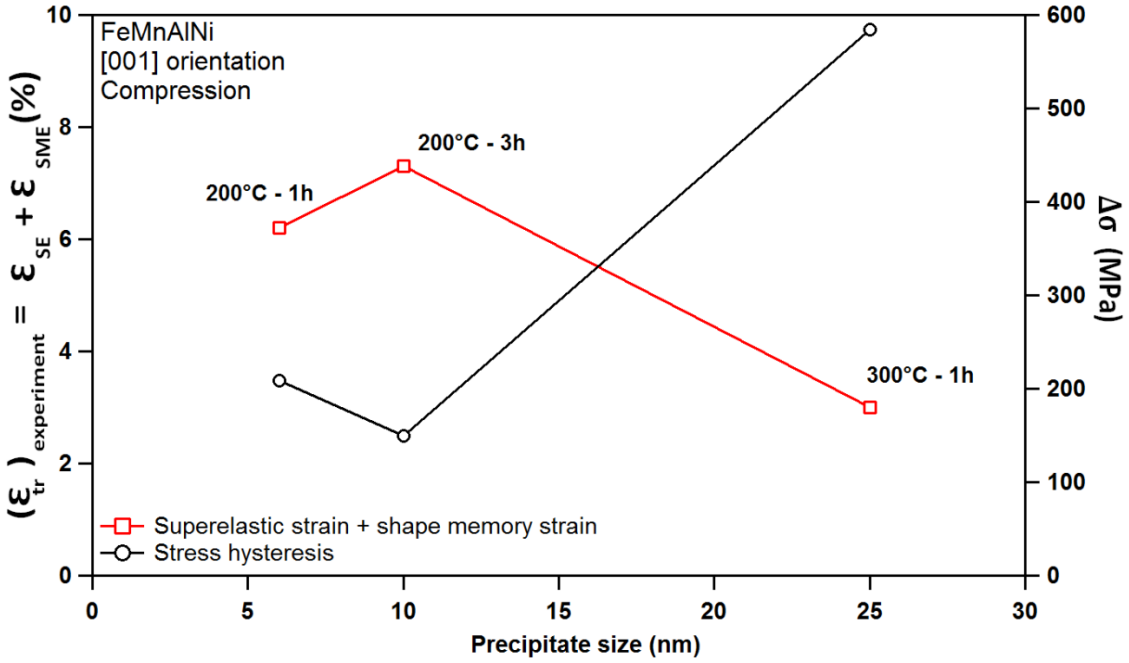

Figure 5.12 The relationship between the superelastic strain plus shape memory strain and stress hysteresis in three different aging conditions. The stress hysteresis is determined from the 5% applied strain shown in Figure 5.8.

We use simple rule of mixture calculation for the expected experimental transformation strain. The equation can be expressed as

$$(\varepsilon_{rec})_{experiment} = (\varepsilon_{tr})_{theory} \bullet (1 - V_m) \tag{5.1}$$

$(\varepsilon_{rec})_{experiment}$, $(\varepsilon_{tr})_{theory}$ and V_m represents the expected experiment superelastic strain, theoretical transformation strain and volume fraction of precipitates. For the 200°C-1h

sample, the $(\varepsilon_{tr})_{theory} = 10.5\%$ and $V_m = 0.298$, we can obtain the expected experiment transformation strain $(10.5\%)(1-0.298) = 7.04\%$. For the 200°C-3h sample, the expected experiment transformation strain $(10.5\%)(1-0.343) = 6.9\%$ by using $V_m = 0.343$. For the 300°C-1h sample, the predict superelastic strain can be calculated as $(\varepsilon_{SE})_{experiment} = 10.5(1-0.306) = 7.29\%$. The result indicates the 200°C-1h sample has the higher expected superelastic strain than 200°C-3h sample. However, the experimental result shows the 200°C-3h has a significantly higher superelastic strain than 200°C-1h sample. The reason could be related to precipitates size. For the 200°C-1h sample, the size of precipitate is about 3-6 nm. The small precipitate size may not be strongly enough to strengthen the austenite matrix to resist the plastic deformation. As a result, the plastic deformation occurs during at higher applied strain levels when martensite variant interactions dramatically increase the magnitude of internal stresses within the sample. By comparison, the size of precipitate is around 6-10 nm in the 200°C-3h sample, which may provide improved strengthening and better recoverability.

On the other hand, further increase in the precipitate size, as in the case of the 300°C-1h sample, may result in a loss in coherency and reduced effects of precipitation hardening. In a study on FeMnAlNi polycrystals, Omori et al. [109] mention the precipitates with the diameter around 10 nm are coherent with the matrix during the martensitic transformation. The range of 5-10 nm also resulted in coherent precipitates in aged FeNiCoAlTa [39,40] and FeNiCoAlTi [84] single crystals. Geng et al. [87] report in aged FeNiCoAlTaB polycrystals that as aging time increases at temperature of

700°C, the martensitic transformation changes from thermoelastic to non-thermoelastic due to coherency loss between the precipitates and the matrix. The precipitate size is around 40 nm in 700°C–240h aged sample. Similar effect may be relevant to the observed results in the present study. Additionally, the increase precipitate size also appears to significantly embrittle the sample, causing fracture at 6% applied strain. Omori et al. [25] reported that aging temperature higher than 300°C decreases the ductility. The similar tensile result is also observed in our study which will show in the later. The single crystal with the [100] orientation aged at 300°C for 1 hour fractures during 2% strain test (reach 1.9% applied strain) at -80°C.

5.3.4 Precipitate Effect on Stress Hysteresis

In order to determine the relationship between the precipitate size and stress hysteresis in different aging conditions, the stress hysteresis values at various applied strain levels was extracted from Figure 5.8 and summarized in Figure 5.13. As expected, stress hysteresis increased with increasing applied strain as greater portion of the material is transformed. It is interesting to note, however, that at any applied strain levels, the stress hysteresis in the 300°C-1h sample was consistently the highest, and in the 200°C-3h sample the lowest. The rate at which stress hysteresis increased with increasing applied strain followed a similar comparable trend: fastest in 300°C-1h and slowest in 200°C-3h.

Interestingly, there appears to be an inverse relationship between maximum recoverable strain and stress hysteresis, shown in Figure 5.12. When the aging time

increases from 1 hour to 3 hours at aging temperature 200°C, the stress hysteresis decreases and superelastic strain increases, and the smallest hysteresis and highest superelastic strain both occur in the 200°C-3h sample. This suggests that superelastic recovery and stress hysteresis may be governed by similar sets of mechanisms. On the smaller end of the precipitate size spectrum, such as in the 200°C-1h sample, plastic deformation that becomes active due to insufficient precipitation strengthening increases the energy dissipation during a transformation cycle, resulting in a larger hysteresis. In contrast, when the precipitates are large as in the case for 300°C-1h, large critical stress is required to induce the martensitic transformation and the frictional resistance to phase boundary motion will increase due to a hardening effect [27-29]. The increase the frictional resistance will amplify hysteresis loop.

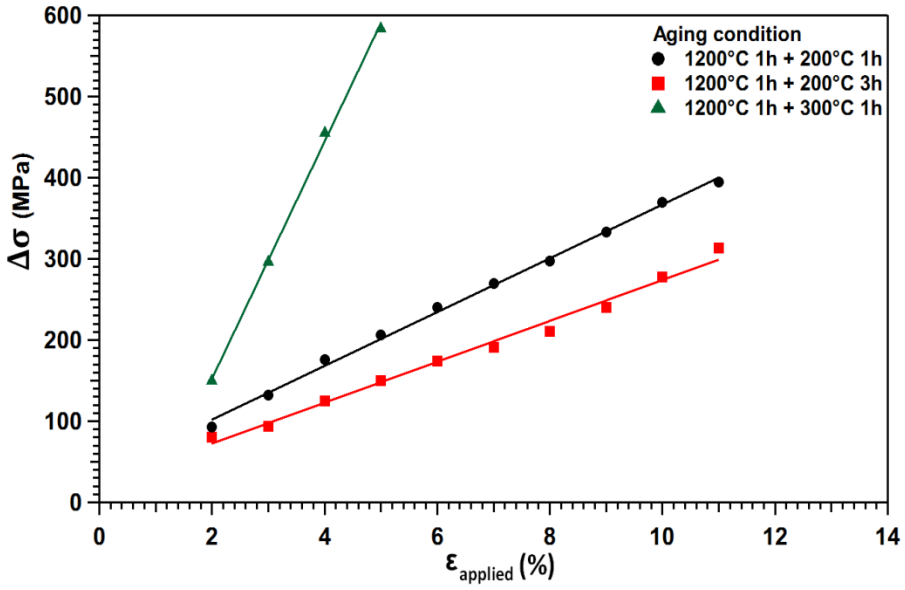

Figure 5.13 The relation between the stress hysteresis and applied strain in $Fe_{43.5}Mn_{34}Al_{15}Ni_{7.5}$ single crystals with the [100] orientation for various aging conditions.

5.4 Effect of Aging on Superelasticity in Tension

The constant strain test in various temperature levels were also carried out in the tension sample. The single crystal samples with the [100] orientation were aged at 200°C for different times and also at 300°C for 1 hours. The tension specimens were loaded to 2% strain at temperatures between -80°C and 160°C. Figure 5.14a-e show the superelastic response of single crystal oriented along the [100] orientation aged at 200°C for 0, 1, 3, 6, 10 hours and 300°C for 1 hour. For 300°C-1h aged sample, the tension sample was fracture during the 2% strain test at -80°C due to forming the large size of precipitates (25 nm). The large precipitate size increases the critical stress for stress-induced martensitic transformation (900MPa) and decreases the ductility.

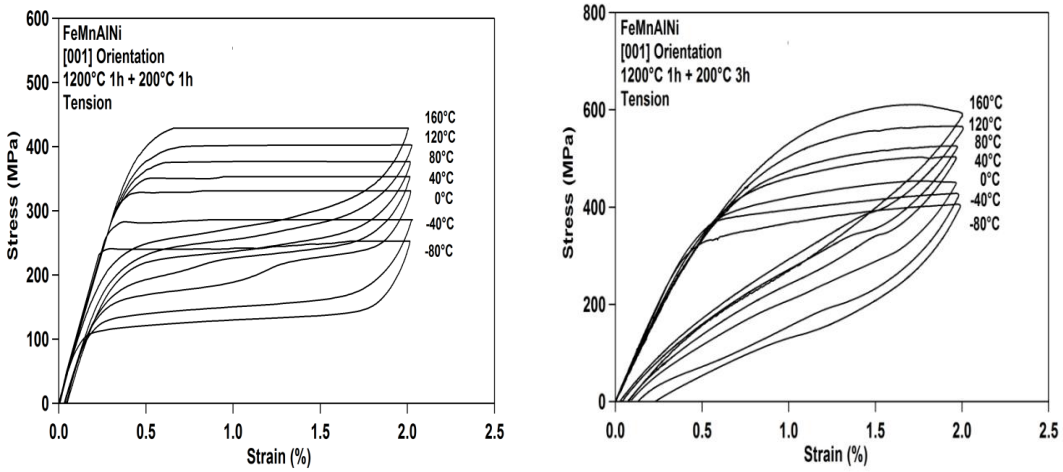

Figure 5.14 Constant strain superelastic experiment: the $Fe_{43.5}Mn_{34}Al_{15}Ni_{7.5}$ [100] single crystal specimens were solution heat treated at 1200°C for 1 hour and aged at different aging conditions. (a) 200°C-1 h (b) 200°C-3 h (c) 200°C-6 h (d) 200°C-10 h (e) 300°C-1 h. The specimens were loaded in tension at various temperatures to approximately 2% strain.

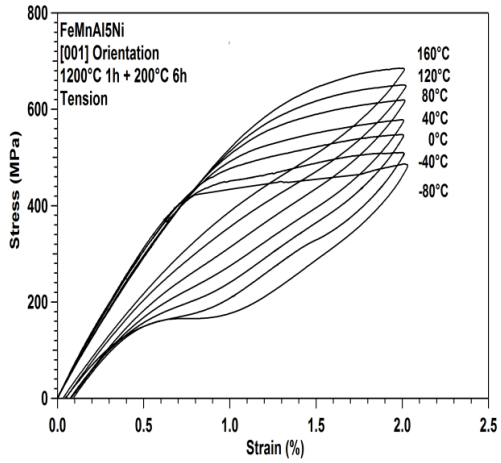

(c)

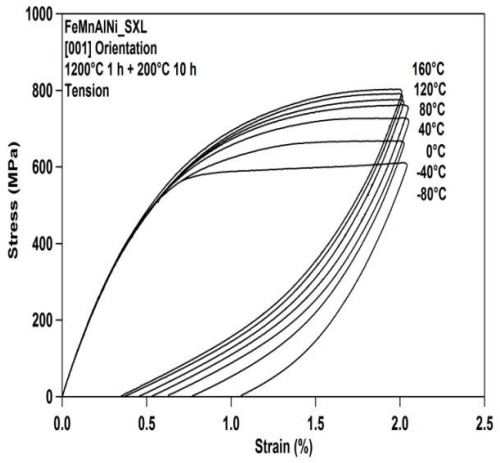

(d)

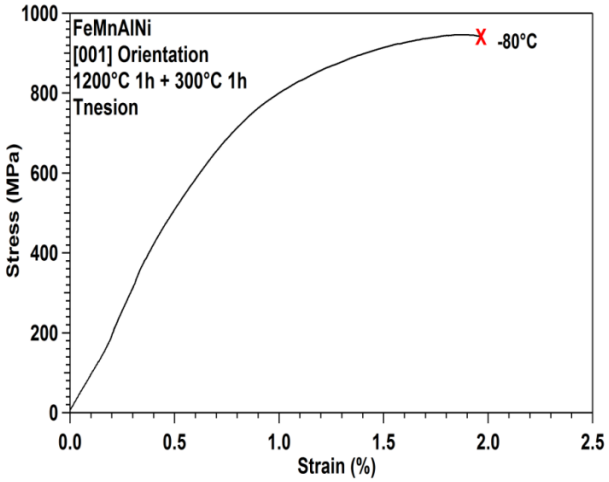

(e)

Figure 5.14 Continued

Figure 5.15 summaries the critical stress in both tension and compression as a function of test temperatures in different aging conditions. The same trend can be also observed from the tension results. The critical stress increases as aging time increase.

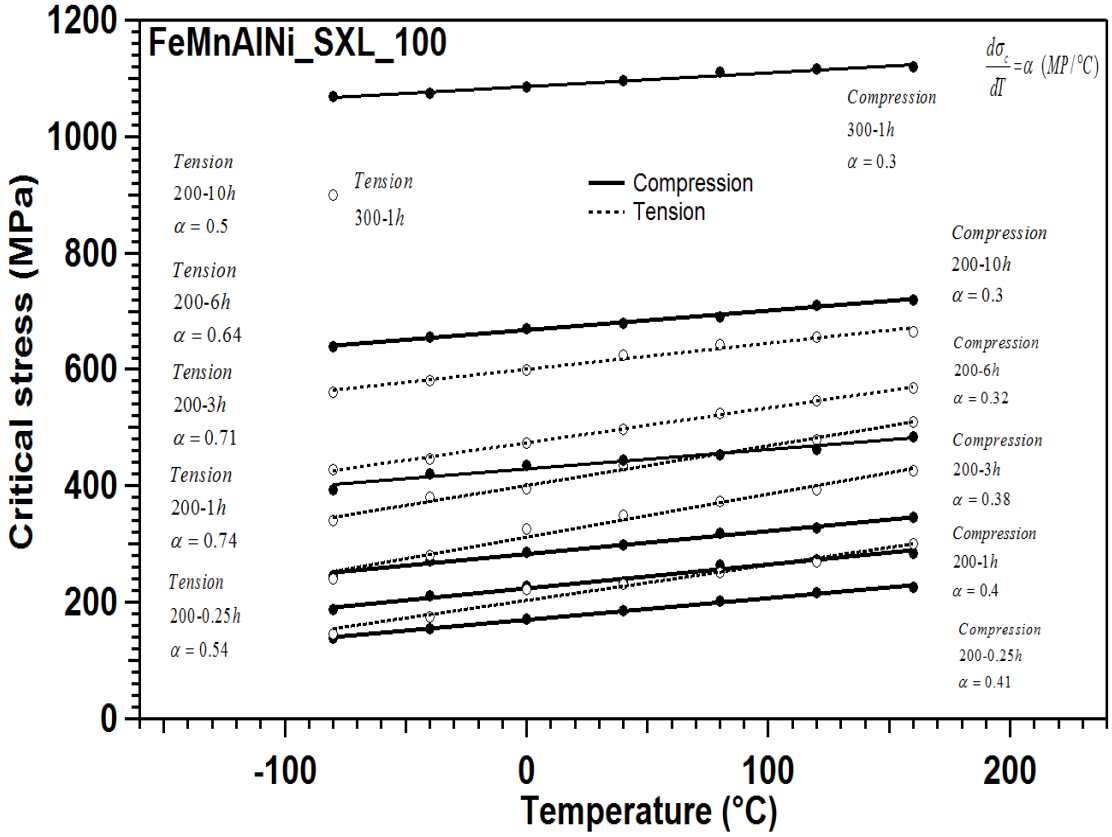

Figure 5.15 Summary of the critical stress for stress-induced martensitic transformations under tension and compression in [100] oriented $Fe_{43.5}Mn_{34}Al_{15}Ni_{7.5}$ single crystals heat treated at 200°C for different times and also at 300°C for 1 hour. The results were determined from constant strain superelastic experiments at different temperatures shown in Figure 5.14.

Figure 5.16a, b, c and d show the incremental stress-strain curves of FeMnAlNi [100] single crystal specimens aged at 200°C for 1 hour, 3 hours, 6 hours, 10 hours under tension test. The superelastic strain and irrecoverable strain levels in tension were extracted from the Figure 5.16 results, shown in Figure 5.17. From the result, the superelastic strain decreases as aging times increase from 1 hour to 10 hours.

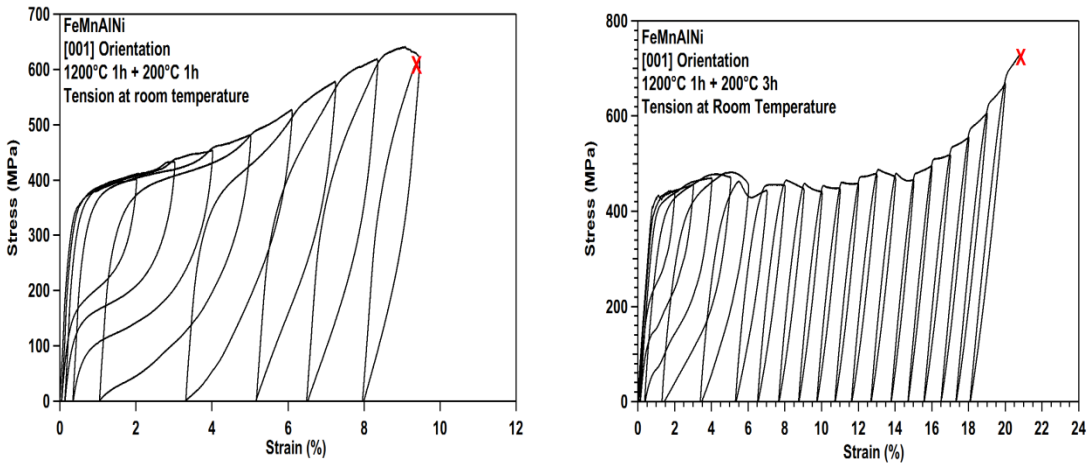

(a) (b)

Figure 5.16 Incremental strain superelastic test at tension in $Fe_{43.5}Mn_{34}Al_{15}Ni_{7.5}$ [100] single crystals solution heat treated at 1200°C for 1 hour and aged at 200°C for different times. (a) 200°C-1h (b) 200°C-3h (c) 200°C-6h and (d) 200°C-10h.

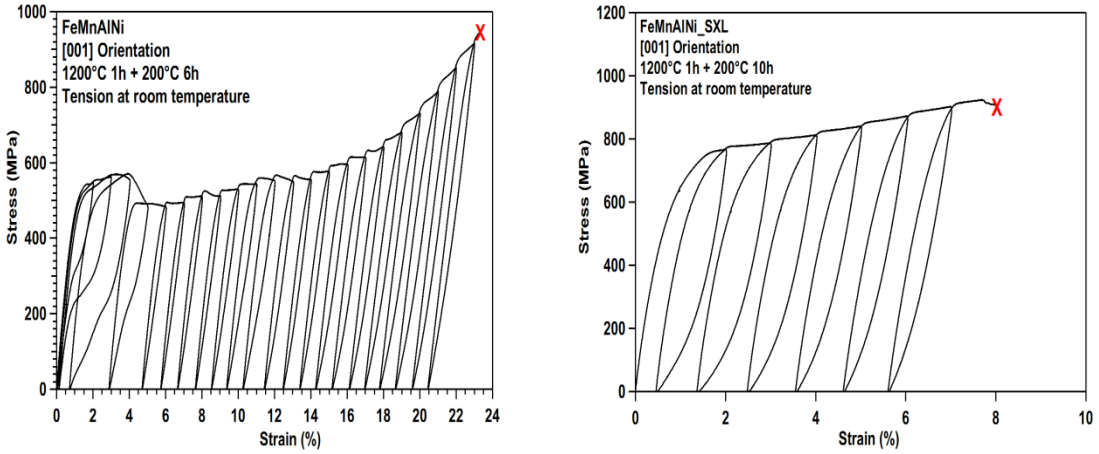

(c) (d)

Figure 5.16 Continued

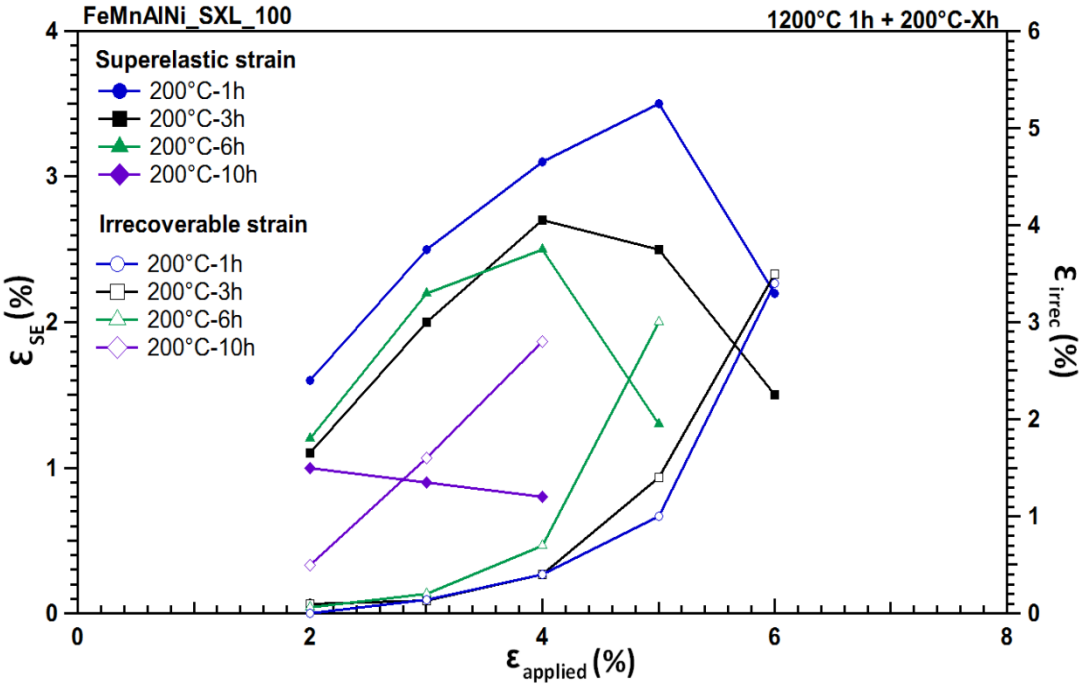

Figure 5.17 The superelastic strain and irrecoverable strain as a function of the applied strain in $Fe_{43.5}Mn_{34}Al_{15}Ni_{7.5}$ single crystal oriented along with the [100] orientation in different conditions under tension test. The data were extracted from Figure 5.16.

From above tension results, the tensile samples do not show complete superelastic recovery when the applied strain levels exceeded about 4 or 5%. Increasing the aging times does not significant improve the superelastic strain in tension compare to it in compression. Table 5.4 summaries the maximum superelastic strain and stress hysteresis in 200°C-1h and 200°C-3h aged samples in both tension and compression. The stress hysteresis is measured from the strain level of 4% from the incremental strain test in both tension and compression. From the result, increasing the aging times from 1 hour to 3 hours at aging temperature of 200°C decreases the stress hysteresis and improves the superelastic strain in compression. In contrast to compression sample, the stress hysteresis increases and superelastic strain declines as aging time increases from 1 hour to 3 hours.

Table 5.4 Summary of the superelastic strain and stress hysteresis in both tension and compression.

Aging conditions (200°C)	Superelastic strain (compression)	Superelastic strain (tension)	Stress hysteresis (compression)	Stress hysteresis (tension)
200°C-1h	5.0%	3.5%	220 MPa	300MPa
200°C-3h	7.2%	2.7%	110 MPa	410MPa

The reason causes the difference of superelastic strain after aging in both tension and compression is related to the martensite variant selection during the superelastic test. As we mention in the previous chapter, two martensite variants can assist the compression deformation and decrease density of dislocations at the austenite-martensite interface and in the austenite matrix. The availability of two martensite variants under compression can improve the stored elastic energy and decrease the stress hysteresis by reduction of the frictional resistance between the austenite-martensite interface and martensite-precipitate boundaries. Increasing the aging times, precipitates assist the martensitic transformation and results in improvement of the stored elastic energy and reduction of the stress hysteresis. On the other hand, increasing the aging times create the larger obstacles that need to accommodate by distortion of precipitates. This leads the generation of dislocations due to immobility of austenite-martensite interface in tension. The high density of dislocations produce the relaxation of austenite-martensite interface causing the stored elastic strain energy dissipation and less elastic strain energy is available to assist the reverse transformation, which amplify the stress hysteresis loop.

5.5 Summary and Conclusions

In this study, we showed that aging heat treatment affects the size, volume fraction and composition of precipitates, which in turn affect transformation temperature and superelastic characteristics such as superelastic strain, stress hysteresis, critical stress and critical stress temperature slope in a FeMnAlNi single crystal sample with the [100] orientation. We summarize the major findings:

1. Increasing the aging times at 200°C increases the size and slightly increases the volume fraction of B2 precipitates. Precipitation coarsening occurs much more quickly at 300 °C compared to 200 °C, but precipitate volume fraction appears to be unaffected. Precipitates are enriched in Ni and Al, and with increasing aging time and temperature, the chemical segregation is magnified.
2. Transformation temperature of the FeMnAlNi single crystal decreases with increasing the aging time and temperature.
3. Mechanical properties such as hardness and superelastic properties such as recoverable strain and stress hysteresis are most directly influenced by the size of precipitates. Larger precipitates monotonically increase hardness, but its influence on recoverable strain and hysteresis show maxima/minima behavior.
4. Optimal superelastic properties are found for samples with precipitate size around 6-10 nm, which represents a balance between sufficient precipitation hardening and avoidance of loss of coherency or excessive embrittlement.

5. The difference of aging effect on the superelastic properties of FeMnAlNi single crystal in both tension and compression is related to the difference of the martensite variant selection. In compression, two variants improve the mobility of austenite-martensite interface. Increasing the size of precipitates results in reduction of the stress hysteresis and improvement of the recoverable strain. In tension, one variant is capable to accommodate the tension deformation. As a result, increasing the size of precipitates leads to more obstacles for the martensitic transformation, and thus large frictional energy generates during the martensitic transformation and cause the poor recoverable strain and large stress hysteresis.

CHAPTER VI

EFFECT OF ORIENTATIONS ON SUPERELASTICITY OF FeMnAlNi SINGLE CRYSTALS UNDER BOTH COMPRESSION AND TENSION

In the previous two chapters, we focus on the superelastic response of the $Fe_{43.5}Mn_{34}Al_{15}Ni_{7.5}$ single crystals with the [100] orientation under both tension and compression. In this chapter, the single crystals with the [111] and [123] orientations are used to investigate the effect of orientations on superelasticity under both compression and tension. The different superelastic responses (critical stress, recoverable strain and slope of stress-temperature curve) of the FeMnAlNi single crystals are related to the crystallographic orientation. The [123] orientation is selected for this study because the multiple martensite variants can activate in this orientation. The [100] and [111] orientations are expected to the large differences in the slopes of the stress-temperature curve because the transformation strains are different significantly for the maximum transformation strain in the [100] orientation compared to the minimum transformation strain in the [111] orientation. The investigation of this chapter contains following section: (1) effects of orientations on superelasticity in the solution-treated FeMnAlNi single crystals with the [100], [111] and [123] orientations under compression test, (2) effects of precipitation or aging on the critical stress and slopes of stress-temperature curve in the aged single crystals with three orientations under compression test, (3) effects of orientations in the aged single crystals with the [100] and [123] orientations under tension test.

6.1 Theoretical Calculations of Transformation Strains

The calculation of theoretical transformation strain was commonly performed by using energy minimization theory [130,131]. The more detailed description of theoretical framework can find in the Ball and James works [132-136]. The theory assumes the two twins related martensite variants can form correspondent variant pair (CVP). Each CVP has unique habit planes and transformation shear. Figure 6.1 shows a schematic of the CVP martensite and habit plane. The vectors n and m represent the twinning and habit planes. f, a and b represent volume fraction of martensite, twin shear and transformation shear, respectively [131,137]. In this theory, there is no prior assumption about twinning system and habit plan.

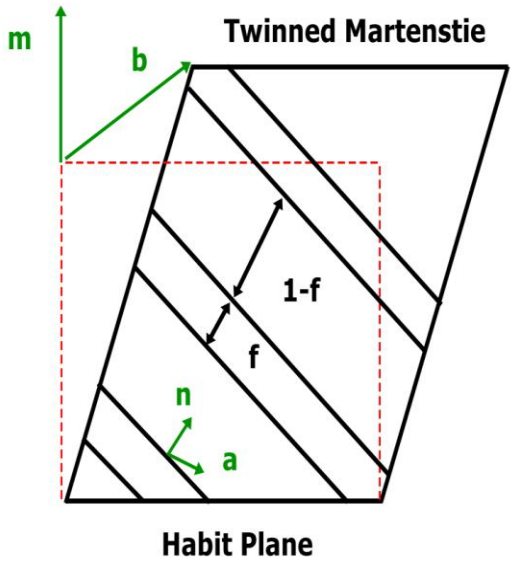

Figure 6.1 Twinning plane (n), habit plane (m), twin shear (a), transformation shear (b), and the volume fraction of martensite (f) [131,137].

The mechanism of the martensitic transformation in iron-based SMAs follows the Bain distortion model. Based on this model, the phase change in FeMnAlNi is from the cubic (austenite) to the tetragon (martensite). The cubic austenite has $S = \rho^{24}$, where S is the point group of the crystal and contains 24 rotations of a cubic. The point group of austenite and martensite are defined as (P_a) and (P_m), respectively. The number of martensite variants (N) is defined as

$$N = \frac{\textit{the}\ \text{number of rotations in}\ \mathrm{P}_a}{\textit{the}\ \text{number of rotations in}\ \mathrm{P}_m} \tag{6.1}$$

For a cubic to tetragonal martensitic transformation (N = 24/8 = 3), it means there are three martensite variants in the fcc-bcc transformation. Let U_1, U_2 and U_3 be the transformation matrix for three martensite variants shown in Figure 6.2. The transformation matrix can be written as

$$U_1(\theta) = diag(\eta_2\ ,\ \eta_1\ ,\ \eta_1),\ U_2(\theta) = diag(\eta_1\ ,\ \eta_2\ ,\ \eta_1),\ U_3(\theta) = diag(\eta_1\ ,\ \eta_1\ ,\ \eta_2) \tag{6.2}$$

$$U_1 = \begin{bmatrix} \eta_2 & 0 & 0 \\ 0 & \eta_1 & 0 \\ 0 & 0 & \eta_1 \end{bmatrix},\quad U_2 = \begin{bmatrix} \eta_1 & 0 & 0 \\ 0 & \eta_2 & 0 \\ 0 & 0 & \eta_1 \end{bmatrix},\quad U_3 = \begin{bmatrix} \eta_1 & 0 & 0 \\ 0 & \eta_1 & 0 \\ 0 & 0 & \eta_2 \end{bmatrix} \tag{6.3}$$

where $\eta_1 = \frac{a}{\sqrt{2}a_0}$, $\eta_2 = \frac{c}{a_0}$, a_0 is the lattice parameter of austenite and a and c are the lattice parameters of martenstie. In the FeMnAlNi material, the lattice parameter of bcc

austenite is $a_0 = a_A = 0.2903nm$ [25]. Because the fcc martensite is the cubic structure, the lattice parameter of martensite is $a = c = a_M = 0.3672\text{nm}$ [25].

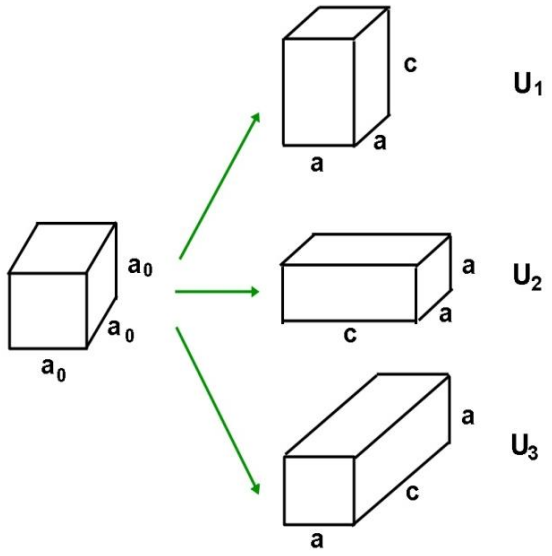

Figure 6.2 The transformation matrix for three variants of martensite in a cubic to tetragonal transformation [131].

The kinematic compatibility between austenite and martensite is

$$R_{ij}U_j - U_i = a \otimes n \tag{6.4}$$

where U_i and U_j are two lattice correspondence variants. The symbol $\otimes$ represents the dyadic product. The R_{ij} is an orthogonal tensor and need to satisfying $R_{ij}^{\ T}R_{ij} = \text{I}$ (T represents the transpose of a matrix) U_i and U_j are the known parameters, and the unknown parameters R_{ij}, a and n can be solved by the equation.

In order to obtain a symmetric matrix C, post multiplying equation 6.3 by U_i^{-1}

$$R_{ij}U_jU_i^{-1} - I = a \otimes \left(nU_i^{-1}\right) \tag{6.5}$$

A symmetric matrix C is formed as

$$C = \left(R_{ij}U_jU_i^{-1}\right)^T \cdot \left(R_{ij}U_jU_i^{-1}\right) = U_i^{-1} \cdot U_j^{\,2} \cdot U_i^{-1} \tag{6.6}$$

C tensor has eigenvalues $\{\lambda_1 , \lambda_2 , \lambda_3\}$ and the corresponding eigenvector $\{e_1 , e_2 , e_3\}$. To satisfy the ordered triple eigenvalues, the necessary and sufficient condition for equation 6.4 has a solution is

$$\lambda_1 \le \lambda_2 = \mathbf{1} \le \lambda_3 \tag{6.7}$$

Then the two solutions are given by

$$\mathrm{a} = \rho\left(\sqrt{\frac{\lambda_3\left(\lambda_2 - \lambda_1\right)}{\lambda_3 - \lambda_1}}e_1 + \kappa\sqrt{\frac{\lambda_1\left(\lambda_3 - \lambda_2\right)}{\lambda_3 - \lambda_1}}e_3\right) \tag{6.8}$$

$$n = \frac{1}{\rho}\left(\frac{\sqrt{\lambda_3} - \sqrt{\lambda_1}}{\sqrt{\lambda_3 - \lambda_1}}\right)\left(-\sqrt{\lambda_2 - \lambda_1}e_1 + \kappa\sqrt{\lambda_3 - \lambda_2}e_3\right) \tag{6.9}$$

where $\rho \neq 0$ and $k = \pm 1$ are selected to make $|n| = 1$

The transformation shear of the martensite b and habit planes normal m can be obtained by using the invariant plane conditions

$$F_M - I = b \otimes m \tag{6.10}$$

where I is the identity tensor and F_M is the average gradient of the twinned martensite. When the twins are fine enough, F_M is represented as:

$$F_M = R_h\left[fR_{ij}U_j + (1-f)U_i \right] \tag{6.11}$$

6.11 where f and $1-f$ are represented volume fractions. The term R_h is the relative rotation between the twinned martensite and the parent phase. Using equations 6.3 and 6.10 substitute into equation 6.9, we can obtain

$$R_h\left[U_i + fa\otimes n\right] = I + b\otimes m \tag{6.12}$$

In order to find the solution for the equation 6.11, we can calculate the symmetric matrix $C(f)$ similar to that in equation 6.5

$$C(f) = (U_i + fa\otimes n)(U_i + fn\otimes a) \tag{6.13}$$

The necessary condition for equation 6.11 to have solution is to satisfy that $C(f)$ has ordered eigenvalues $\lambda_1 \le \lambda_2 = 1 \le \lambda_3$, and the corresponding eigenvectors e_1 , e_2 , e_3 are obtained. The volume fraction of f can calculate by

$$\det(C(f) - \mathrm{I}) = 0 \tag{6.14}$$

The solutions of b and m in equation (6.11) are given by

$$m = \frac{1}{\rho}\left(\frac{\sqrt{\lambda_3} - \sqrt{\lambda_1}}{\sqrt{\lambda_3 - \lambda_1}} \right)\left(-\sqrt{\lambda_2 - \lambda_1}e_1 + \kappa\sqrt{\lambda_3 - \lambda_2}e_3 \right) \tag{6.15}$$

$$b = \rho\left(\sqrt{\frac{\lambda_3(\lambda_2 - \lambda_1)}{\lambda_3 - \lambda_1}}e_1 + \kappa\sqrt{\frac{\lambda_1(\lambda_3 - \lambda_2)}{\lambda_3 - \lambda_1}}e_3 \right) \tag{6.16}$$

Given the lattice parameters of austenite and martensite, we can easily calculate the n, a, b and m. The values of all the transformation vector are determined as

$n = \{\bar{1}, 1, 0\}$, $a =< 0.4005, 0.5571, 0 >$, $b =< 0.0365, -1.637, 0.127 >$ and $m = \{0.1953, 0.7078, 0.6789\}$. Once the transformation shear (b) and habit plane (m) are determined, it is possible to calculate the transformation strain as

$$\varepsilon^{CV} = \frac{1}{2}(\mathrm{F}_M^T \cdot \mathrm{F}_M - I) = \frac{1}{2}\left[b \otimes m + m \otimes b + (b \cdot b) m \otimes m\right] \tag{6.17}$$

The transformation strain contours for CVP strain in both tension and compression are provided in Figure 6.2a and b. From the result, the transformation strain level is 10.5% for the [100] orientation, 2.2% for the [111] orientation and 7% for the [123] orientation in compression. The CVP strains are 10.5% for the [001] orientation, 2.5% for the [111] orientation and 9% for the [123] orientation in tension.

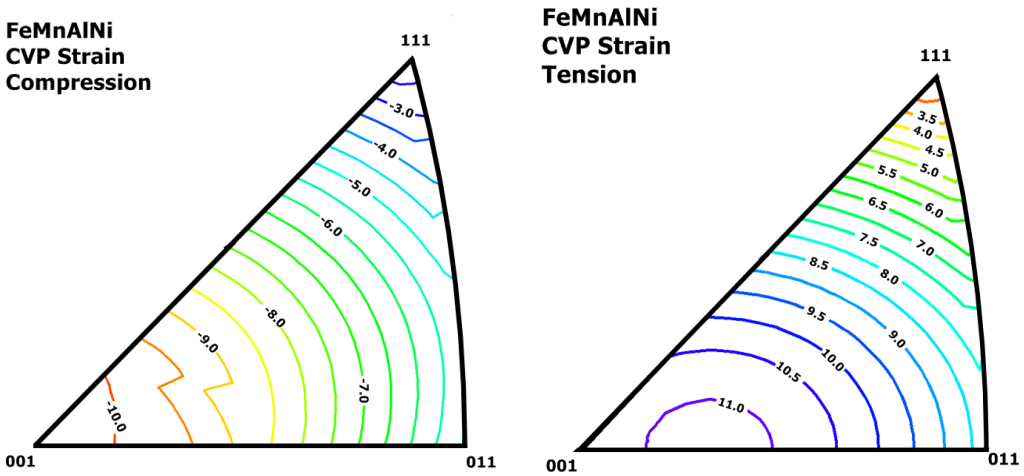

(a) (b)

Figure 6.3 CVP formation strain contours for FeMnAlNi SMAs (a) in compression and (b) in tension.

The detwinning strain is the growth of the variant with the large volume fraction, as a result the deformation after detwinning is $f = 0$

$$F_M^{dt} = R_h U_i \tag{6.18}$$

If the volume fraction (f) is greater than 0.5, martensite variant will growth and the martensitic transformation will include detwinning, the equation is given by

$$F_M^{dt} = R_h R_{ij} U_i = R_h \cdot \left(U_i + a \otimes n\right) \tag{6.19}$$

Once F_M^{dt} is obtained and substitute the F_M to F_M^{dt} in the equation 6.17. The transformation strain (ε^{CV}) will include not only CVP strain but also detwinning strain.

The transformation strain (the CVP and Detwinning strains) contour in both tension and compression are displayed in Fig. 6.3a and b. The CVP and Detwinning strains are -10.5% for the [001] orientation, -0.5% for the [111] orientation and -9% for the [123] orientation in compression. In tension results, the CVP and Detwinning strains are 26.5% for the [001] orientation, 3.3% for the [111] orientation and 14% for the [123] orientation.

The resolved shear stress factor (RSSF) is calculated by using equation 6.19.

$$RSSF = \left(b \cdot e + m \cdot e\right) / \left|b\right| \tag{6.19}$$

The RSSF contours in both tension and compression are shown in Figure 6.5a and b. in compression are -0.52 for the [001] orientation, -0.15 for the [111] orientation and -0.36 for the [123] orientation. The RSSFs in tension are 0.44 for the [001] orientation, 0.12 for the [111] orientation and -0.36 for the [123] orientation. The RSSFs are higher than 0.5 is feasible as the vector b and m are not exactly orthogonal [137].

The RSSF above 0.5 were also reported in many SMAs such as NiTi [131,138], InTi [131], CuNiAl [139,140], CoNiAl [141] and CoNiGa [142].

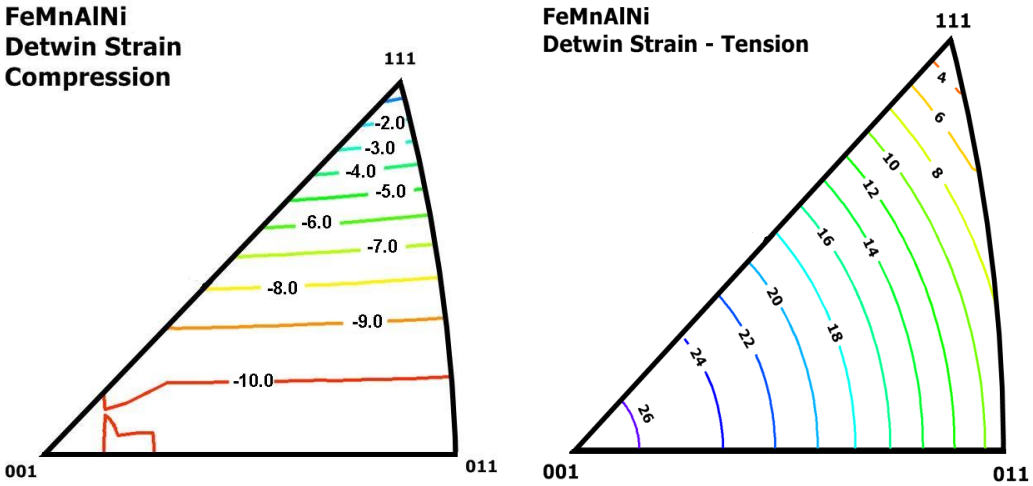

(a) (b)

Figure 6.4 Transformation strain contours after detwinning for FeMnAlNi SMAs in (a) compression and (b) tension.

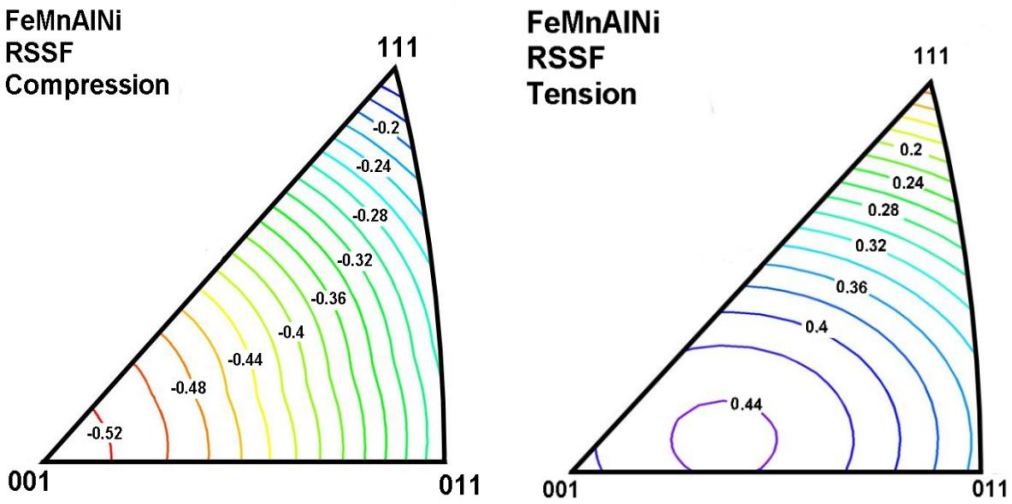

(a) (b)

Figure 6.5 Resolved shear stress factors for FeMnAlNi SMAs in (a) compression and (b) tension.

6.2 Orientations Dependence of Stress-Strain Response in Solution-Treated Single Crystals under Compression

Figure 6.6a and b display the compressive stress-strain curves at various temperatures in the solution-treated $Fe_{43.5}Mn_{34}Al_{15}Ni_{7.5}$ single crystals with the [111] and [123] orientations. The 2% applied strain is used for all test temperatures. After finishing test at each test temperature, the sample is heated up to 100°C above the austenite finish temperature and cooled down to the next test temperature to recover all irrecoverable strain from the previous superelastic test. The stress-strain response of the single crystals with the [100] orientation in compression test have been shown in previous chapter. From the results, the recoverable strain in all orientations increases with increasing the temperature because the test temperatures are closed to austenite finish temperature. When the test temperatures are higher than A_f (45°C), the superelastic results show nearly full recoverable strain after unloading the force. Moreover, the stress-strain curve in the [111] orientation is steeper than it in the [100] and [123] orientations. From the transformation strain contour results, the transformation strain in the [111] orientation is about 2.2%. The 2% applied strain is closely to the transformation strain in the [111] orientation. As a result, the compressive stress-strain curves exhibit an upward slope which indicates the martensitic transformation is almost completion in the [111] orientation.

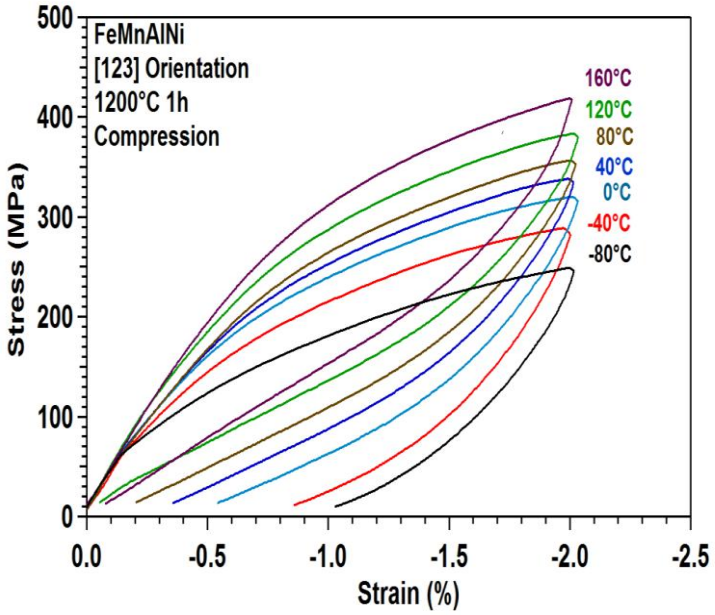

(a)

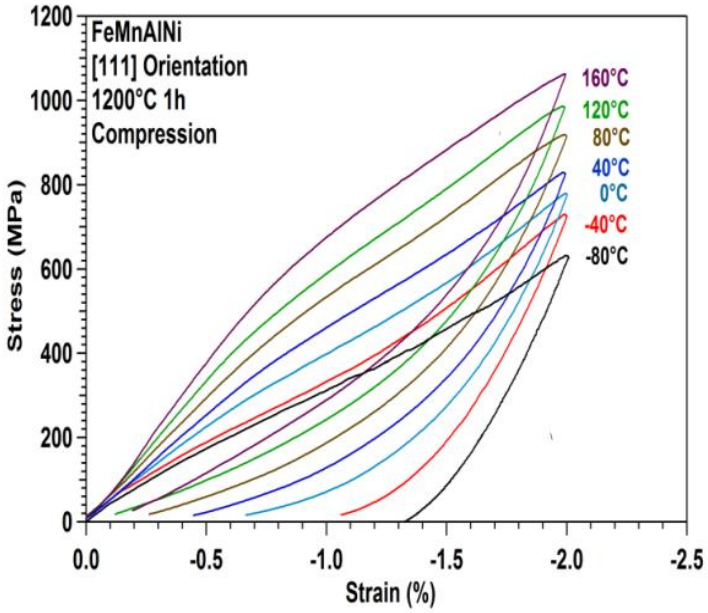

(b)

Figure 6.6 Compressive stress-strain responses for the $Fe_{43.5}Mn_{34}Al_{15}Ni_{7.5}$ single crystals solution heat treated at 1200°C for 1 hour under constnat strain test: (a) [123] orientation and (b) [111] orientation.

The slopes of Clausius-Clapeyron curve in different orientations are summarized in Figure 6.7. A thermodynamic analysis of stress-induced martensite transformation presents that critical stresses for stress-induced martensitic transformation linearly increase with the temperature. The slopes are 0.52 MPa/°C, 0.73 MPa/°C and 2.05 MPa/°C from -80°C to 160°C for the [100], [123], and [111] orientations, respectively. The largest stress-temperature slope is in the [111] orientation compared to that in the [100] and [123] orientations, which is attributed to the transformation strain. From the Clausius-Clapeyron equation (equation 2.7), the stress-temperature slope is inversed proportional to the transformation strain. From the transformation strain contour results (Figure 6.3a), the transformation strains in the [100], [123] and [111] orientations are 10.5%, 7% and 2.2%. Higher transformation strain in the [100] orientation corresponds to the smaller stress-temperature slope.

Moreover, the critical stress for stress-induced martensitic transformation in the [111] orientation is higher than that in the [100] and [123] orientations at the same test temperatures. The reason is related to the resolved shear stress factors in different orientations. From the Figure 6.5 result, the [111] orientation has the lowest RSSF, which is 0.15. Thus, the large stress is required to initial the martensitic transformation in the [111] orientation. The [100] orientation with the large RSSF about 0.52 can easily activate the martensitic transformation during the superelastic test and results in the small critical stress to induce the martensitic transformation.

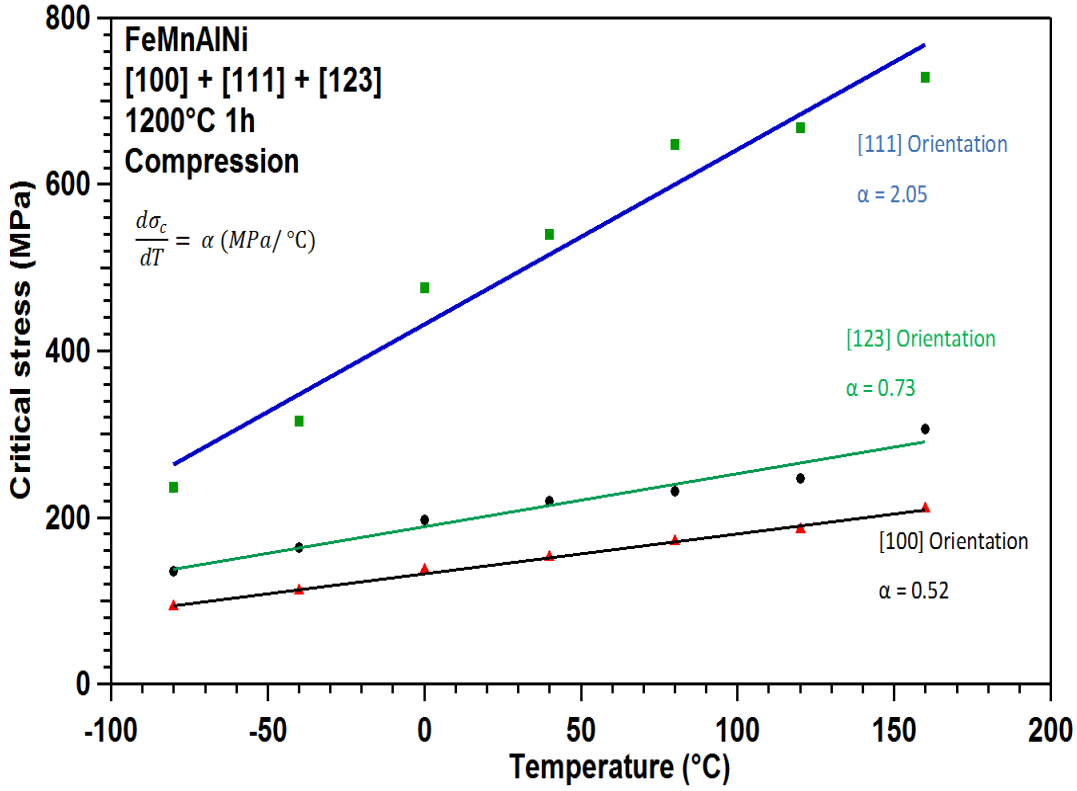

Figure 6.7 Orientation and temperature dependence of the critical stress for stress-induced martensitic transformation under compression in the solution-treated $Fe_{43.5}Mn_{34}Al_{15}Ni_{7.5}$ single crystals with the [100], [111] and [123] orientations.

6.3 Effect of Aging on Superelasticity in Single Crystal Oriented in [111], [123] and [100] Directions in Compression

6.3.1 Stress-Temperature Phase Diagram

The stress-strain response of constant strain compressive test for FeMnAlNi [123] and [111] oriented single crystals aged at 200°C for 3 hours are shown in Figure 6.8. The selection of this aging condition is due to possess the highest superelastic strain in compression based on the previous single crystals with the [100] orientation studies. From the results, the stress-strain curve in the [111] orientation shows the plateau region when the test temperature is above 120°C. The stress-strain response for the [100] orientation have been shown in the previous chapter. Compare to solution-treated samples, the critical stress in all orientations increases after aging. The result indicates that the transformation temperatures tend to decrease after aging. Moreover, the stress hysteresis in the solution-treated single crystals with the [100] and [123] orientations is wider than it in the aged single crystals. The reason is related to the stored elastic energy and dissipation energy. For the aged sample, the contribution of stored elastic energy would increase due to shear precipitate stress field, which decrease the necessary overheating and thus the stress hysteresis decrease. In the [111] orientation, the stress hysteresis is larger than that in solution heat treatment sample due to formation of dislocations.

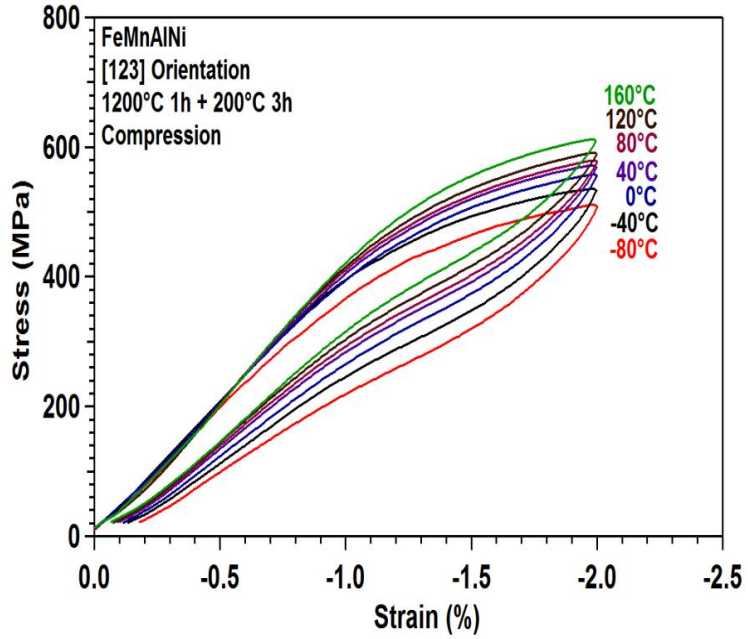

(a)

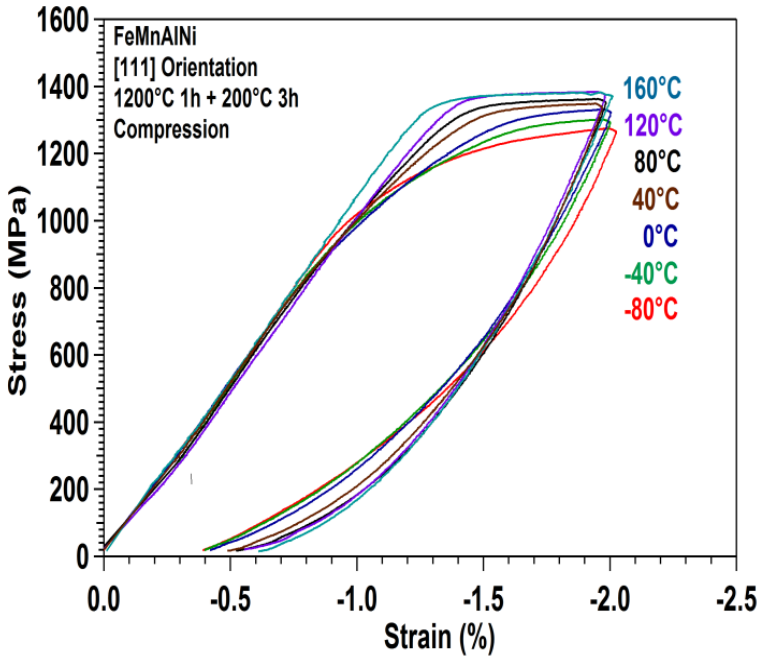

(b)

Figure 6.8 Stress vs. strain responses of the $Fe_{43.5}Mn_{34}Al_{15}Ni_{7.5}$ single crystals aged at 200°C for 3 hours under constant compressive strain: (a) [123] orientation and (b) [111] orientation

The slope of Clausius-Clapeyron line in aged FeMnAlNi single crystals for the [100], [123] and [111] orientations are shown in Figure 6.9. The critical stress in the [111] orientation decreases when the test temperatures are above M_d (125°C). Because the critical stress for slip is higher than the critical stress for slip, the dislocations generate and cause the plastic deformation. The slopes of Clausius-Clapeyron curve are 0.38 MPa/°C and 0.58 MPa/°C from -80°C to 160°C for the [100] and [123] orientations, respectively. For the [111] orientations, the slope is about 1.25 MPa/°C from -80 to 120°C.

From above results, the ratio of the Clausius-Clapeyron line for the [100] and [111] orientations aged samples is around 3.3 ($\alpha_{[111]} / \alpha_{[100]}$). For the solution-treated samples, the ratio of the Clausius-Clapeyron curve for the [100] and [111] orientations is about 4 ($\alpha_{[111]} / \alpha_{[100]}$). The difference of the ratio of the slope for the aged samples is lower than it for the solution-treated samples. The result indicates the orientation dependence of the Clausius-Clapeyron slope is decreased by aging heat treatment. On the other hand, the solution-treated samples exhibit the strong orientation dependence of the Clausius-Clapeyron slope. The similar results are also reported in NiTi alloys [143].

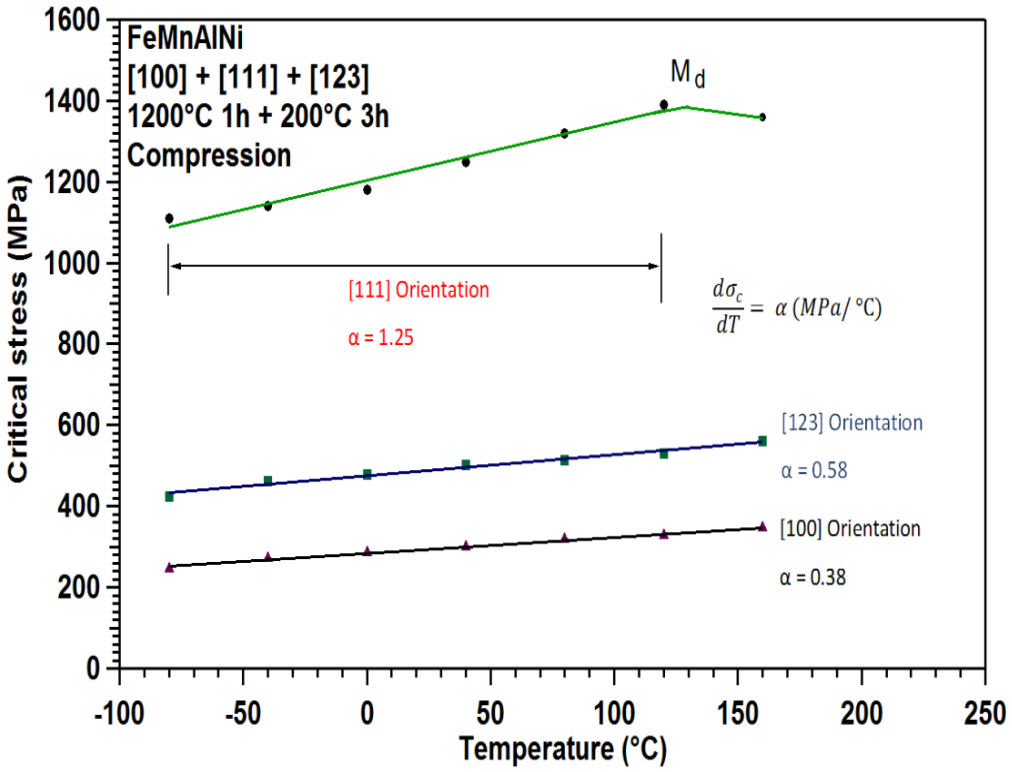

Figure 6.9 Stress-temperature phase diagram in the $Fe_{43.5}Mn_{34}Al_{15}Ni_{7.5}$ [100], [111] and [123] oriented single crystals aged at 200°C for 3 hours under compression test.

6.3.2 Recoverable Strain and Stress Hysteresis

The stress-strain responses of incremental strain compressive test for $Fe_{43.5}Mn_{34}Al_{15}Ni_{7.5}$ single crystals with the [123] and [111] orientation aged at 200°C for 3 hours are shown in Figure 6.10a and b. The inceremtnal strain test results of the single crystals with the [100] orientation aged at 200°C for 3 hours have been displayed in the previous chapter. For the [111] orientation, the plateau region appear after 2% applied strain. Martensite yielding occurred near 1400 MPa and 1500 MPa in the [111] and [123] orinetations, respectively. The strain hardneing of martensite with incrasing applied strain is due to plastic deformation and generation of dislocations. In the [100]

orientation, the slope of the stress-strain curves remains low during the plateau region of the transformation, but increase sharply upward slope near the 10% applied strain, which indicates the completion of martensitic transformation. The reason is that the martensite variant-variant interaction becomes intense near the complete transformation. In the [123] orientation, we can see competition of transformation near 9% applied strain which means the transformation strain will be completed.

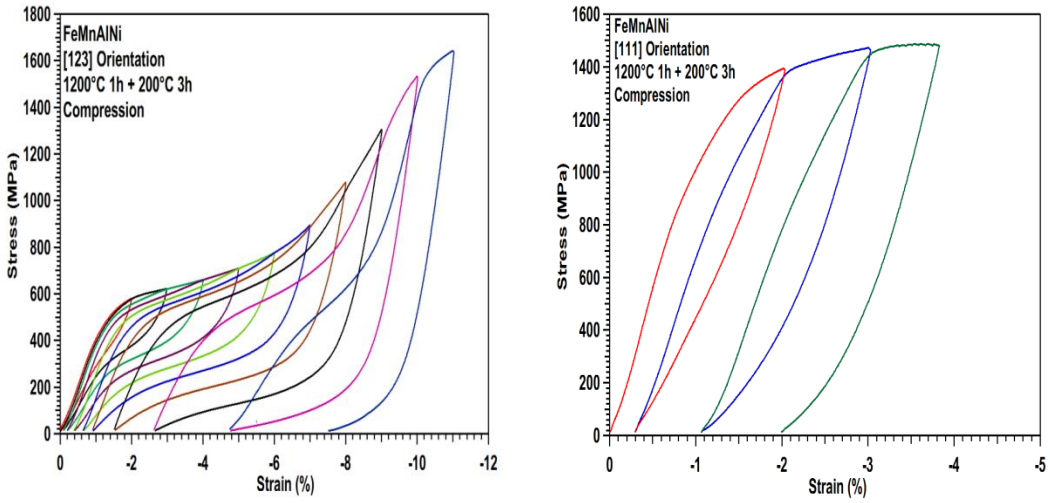

(a) (b)

Figure 6.10 Stress vs. strain responses of the $Fe_{43.5}Mn_{34}Al_{15}Ni_{7.5}$ single crystals aged at 200°C for 3 hours under incremental compressive strain test at room temperature: (a) [123] orientation and (b) [111] orientation.

The recoverable strain and irrecoveralbe strain as a function of applied strain in different orientaitons is summaried in Figure 6.11. The maximum and minimum recoverable strains are in the [100] and [111] orientations, respectively. The maximum recoverable strains are 8.2%, 6.4% and 1.9% in the [100], [123] and [111] orientations, respectively. Table 6.1 summaries the theoretical calculation of transformation strain and experimental recoverable strain in compression. From the results, the [100] orientation shows the higher recoverable strain than that in [111] and [123] orientations.

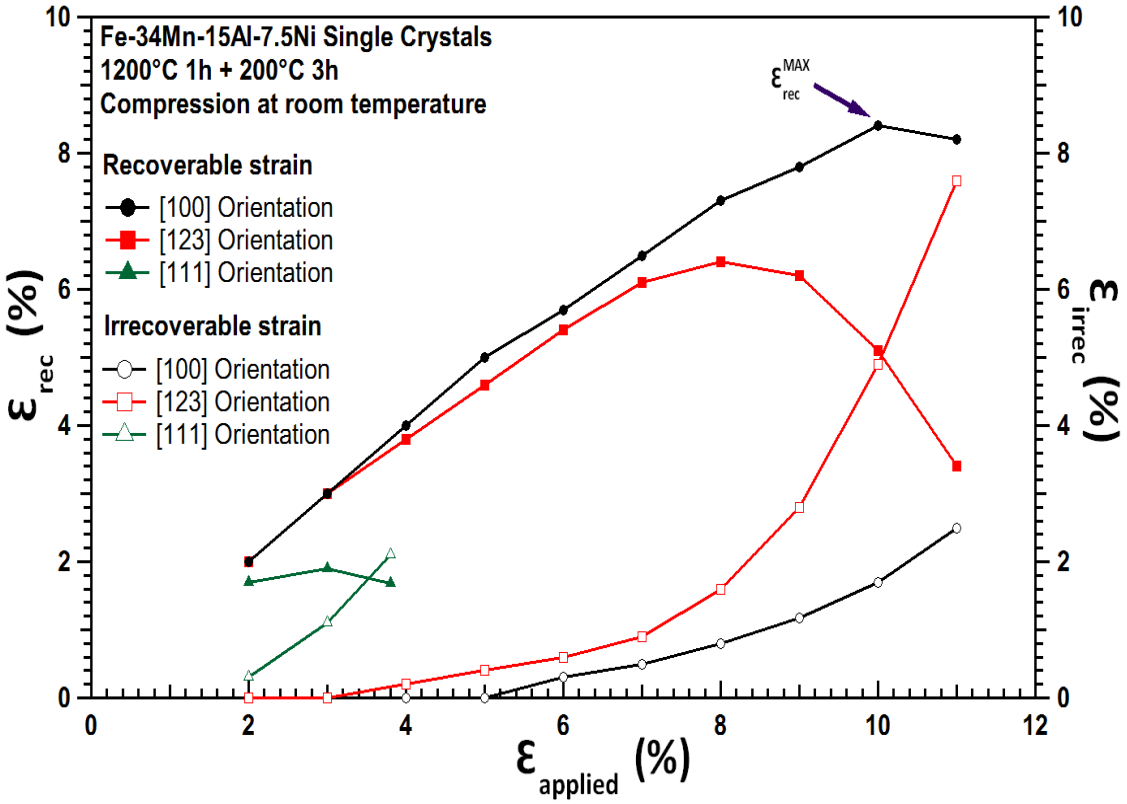

Figure 6.11 Recoverable strain and irrecoverable strain as a function of applied strain in the $Fe_{43.5}Mn_{34}Al_{15}Ni_{7.5}$ single crystals with the [111], [123] and [100] orientations under compression test at room temperature.

Table 6.1 Theoretical CVP formation strains, detwinning strains, maximum experimental recoverable strain in compression.

	CVP strain (Compression)	Detwinning strain (Compression)	Experiment Max. recoverable strain
[001]	10.5%	10.5%	8.2%
[111]	2.2%	0.5%	1.9%
[123]	7.0%	9.0%	6.4%

Figure 6.12 summaries the stress hysteresis as a function of applied compressive strain for the single crystals with the [111], [123] and [100] orientations. The stress hysteresis values were extracted from the incremental strain test, shown in Figure 5.8c and 6.10. From the results, the stress hysteresis increases with increasing the applied strain for all orientations under compression. The stress hysteresis grows rapidly with increasing applied strain in the [111] orientation due to generation of dislocations. Moreover, the wide stress hysteresis in the [111] orientation is attributed to the high internal frictional resistance between the austenite-martensite interface. The dislocations increase the frictional dissipation between austenite and martensite interface and leads to large stress hysteresis growth for the [111] orientation. The [100] orientation single crystals shows the small increase in the stress hysteresis, which suggests the [100] orientation is more favorable for the suppression of energy dissipation.

Table 6.2 summaries the stress hysteresis in the solution-treated and aged FeMnAlNi single crystals with the [100], [111] and [123] orientations. The values of stress hysteresis in the [100] and [123] orientations are extracted from the 4% applied strain. Because the solution-treated single crystals with the [111] orientation can only reach 2.2% strain, the stress hysteresis is determined from the 2% applied strain.

Comparison of incremental strain results for both solution-treated and aged samples with the [100] and [123] orientations, the stress hysteresis loop in the solution treated samples is wider than it in the aged samples. The stress hysteresis is related to the stored elastic energy and dissipation energy. For the aged sample, the precipitates assist the reverse transformation and decrease the frictional resistance between the austenite-martensite interfaces. Reduce the resistance of the interfacial motion will narrow the stress hysteresis loop. Moreover, the precipitates strengthen the austenite matrix to resist plastic deformation, which causes the relaxation of stored elastic energy. For the [111] orientations, the critical stress in the aged sample is larger than it in the solution-treated sample due to precipitation. When the critical stress is higher than the critical stress for slip, the plastic deformation occurs and amplifies the stress hysteresis loop.

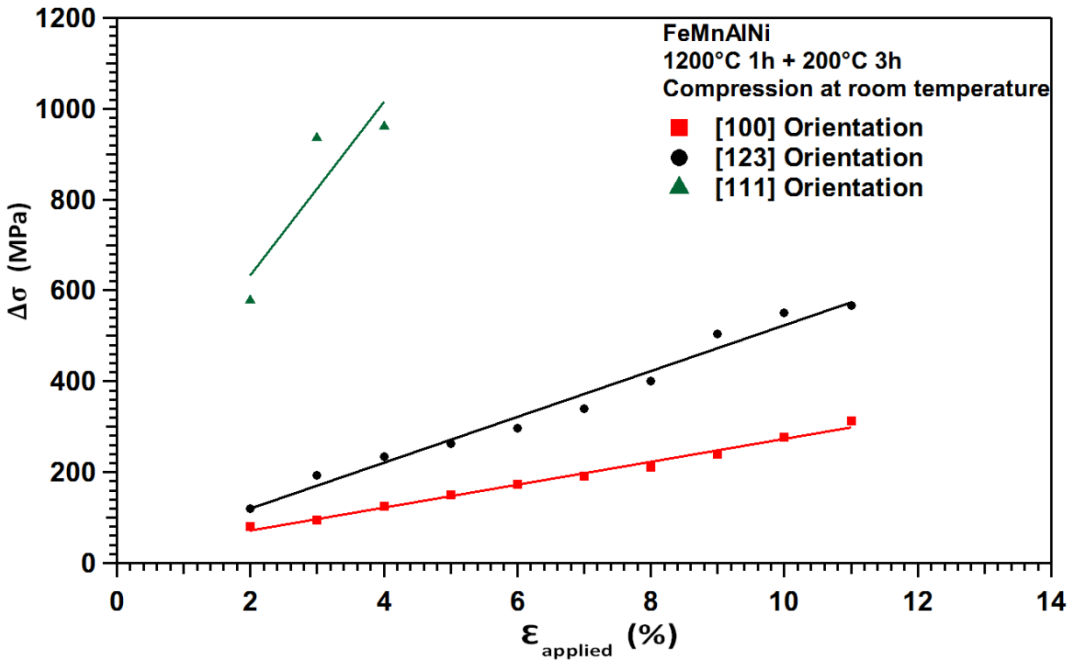

Figure 6.12 Stress hysteresis for the single crystals with the [111], [123] and [100] orientations. Stress hysteresis is determined from the incremental compressive strain test at room temperature shown in Figure 5.8c and 6.10.

Table 6.2 Summary of the stress hysteresis in the solution-treated and aged samples from incremental strain test under compression. The stress hysteresis is measured from the 4% applied strain.

	Solution-treated samples	**Aged samples**
[100]	150 MPa	125 MPa
[123]	285 MPa	234 MPa
[111]	400 MPa	570 MPa

6.4 Superelastic Response in the [123] Oriented FeMnAlNi Single Crystals under Tension

Based on the effect of aging on superelasticity in single crystal with the [100] orientation results, the large superelastic or recoverable strain is obtained in 200°C-3h sample. The similar results are also found in the single crystal with [123] orientation under compression test, shown in Appendix A. Figure 6.13a and b show the tensile stress-strain response for the $Fe_{43.5}Mn_{34}Al_{15}Ni_{7.5}$ single crystals oriented along the [123] direction aged at 200°C for 3 hours and 6 hours under incremental strain test at room temperature. The recoverable strain and irrecoverable strain as a function of applied strain in tension is summarized in Figure 6.14. From the result, the large recoverable strain is obtained in 200°C-3h sample. Both samples are fracture during the 9% applied strain, which is closed to the theoretical calculation of CVP strain (9%). The slope of stress-temperature curve for FeMnAlNi single crystals with the [123] orientation in both tension and compression are shown in Appendix B.

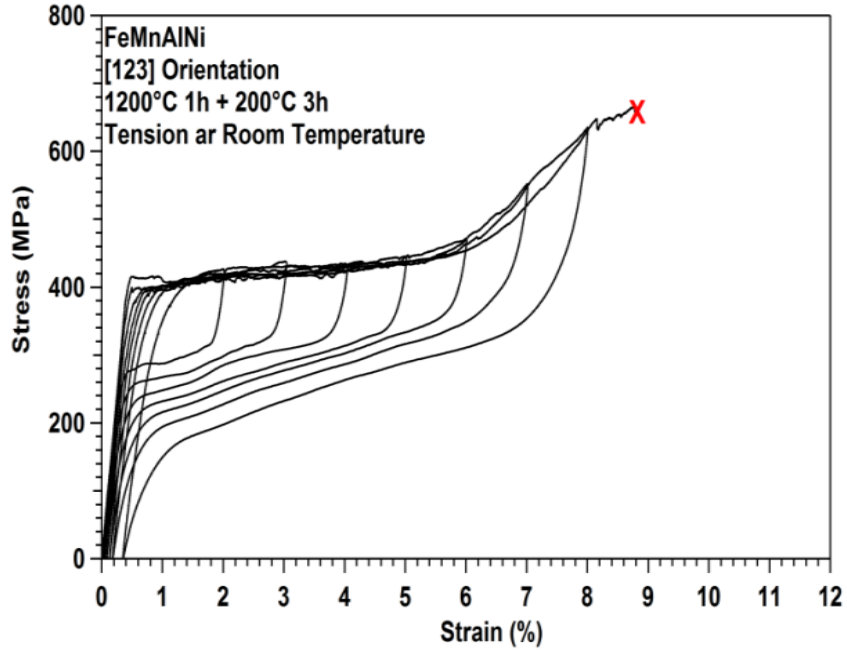

(a)

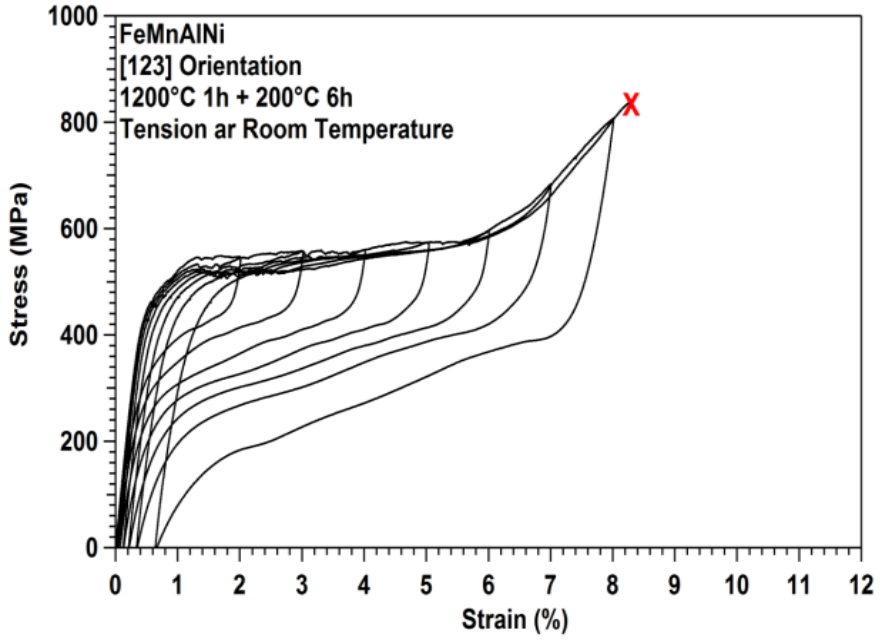

(b)

Figure 6.13 Incremental tensile strain test at room temperature in the $Fe_{43.5}Mn_{34}Al_{15}Ni_{7.5}$ single crystals oriented in [123] direction aged at 200°C for (a) 3 hours and (b) 6 hours.

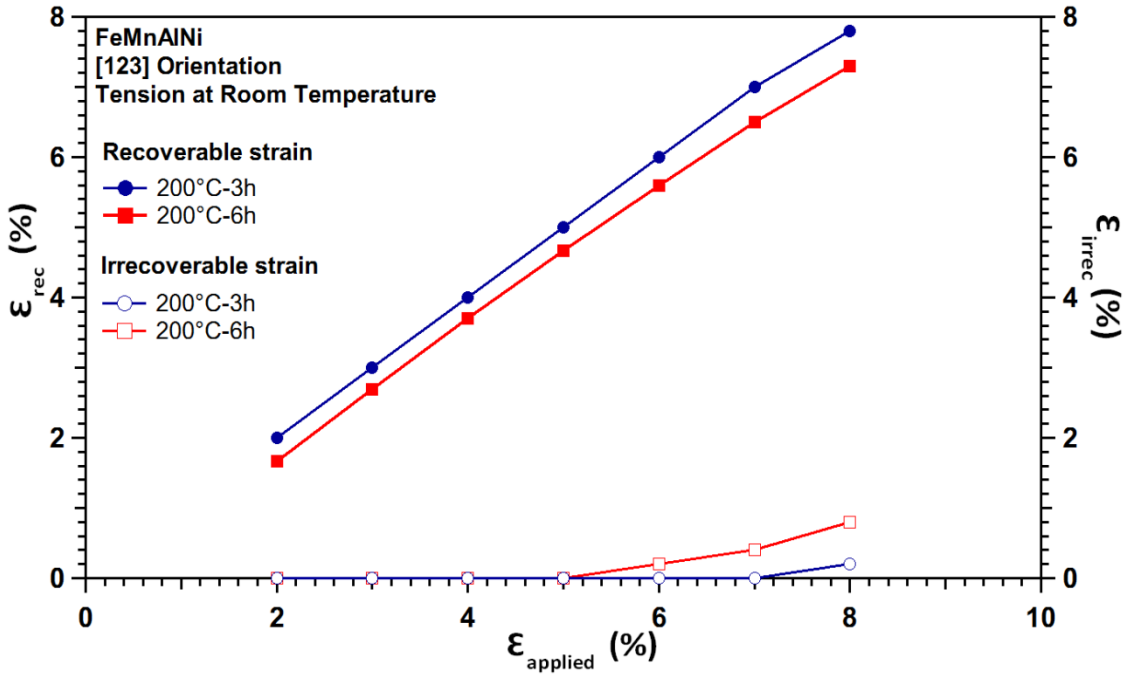

Figure 6.14 Recoverable strain and irrecoverable strain as a function of applied strain in the $Fe_{43.5}Mn_{34}Al_{15}Ni_{7.5}$ single crystals with the [123] orientations under tension test at room temperature.

From above superelastic result, the maximum recoverable strain in the [123] orientation is about 7.8%. When aging time increases to 6 hours, the maximum recoverable strain slightly decrease. Compare the incremental strain tensile results in the aged single crystals with the [100] and [123] orientations, we can observe difference of the superelastic results between the [100] and [123] orientations. Figure 6.15 displays the recoverable strains as a function of applied strain in the aged single crystals with the [100] and [123] orientations. From the results, the recoverable strain in [123] orientation is larger than that in [100] orientation. In the section 6.1, we use two different methods to calculate theoretical transformation strains. One is assume the martensite is fully detwinned and formed a single variant. The other is assumed the martensite is internally

twinning and forming the CVP strain. From the experimental results, the fracture strains for the tension sample oriented in the [123] and [100] directions are about 9% and 24%, respectively. The fracture strain values are closed to the calculation of CVP strain in the [123] orientation, which transformation strain is approximately to 9%. The result suggests the martensite is internal twinning in the [123] orientation and can form the CVP strain. In contrast to the [123] orientation, the fracture strain in the [100] is about 24% and closed to the calculation of detwinning strain. The result suggests the deformation mechanism in the [100] orientation is the detwinning strain, which form a single martensite variant. Therefore, CVP formation strain in the [123] orientation can easily accommodate the tension deformation. As a result, the tension sample in the [123] orientation shows fully recoverable strain. On the contrary, only one martensite variant accommodates the tensile deformation in the [100] orientation and the high density of dislocations generate at the austenite-martensite interface and austenite matrix. The dislocations cause the large irrecoverable strain and wide stress hysteresis loop.

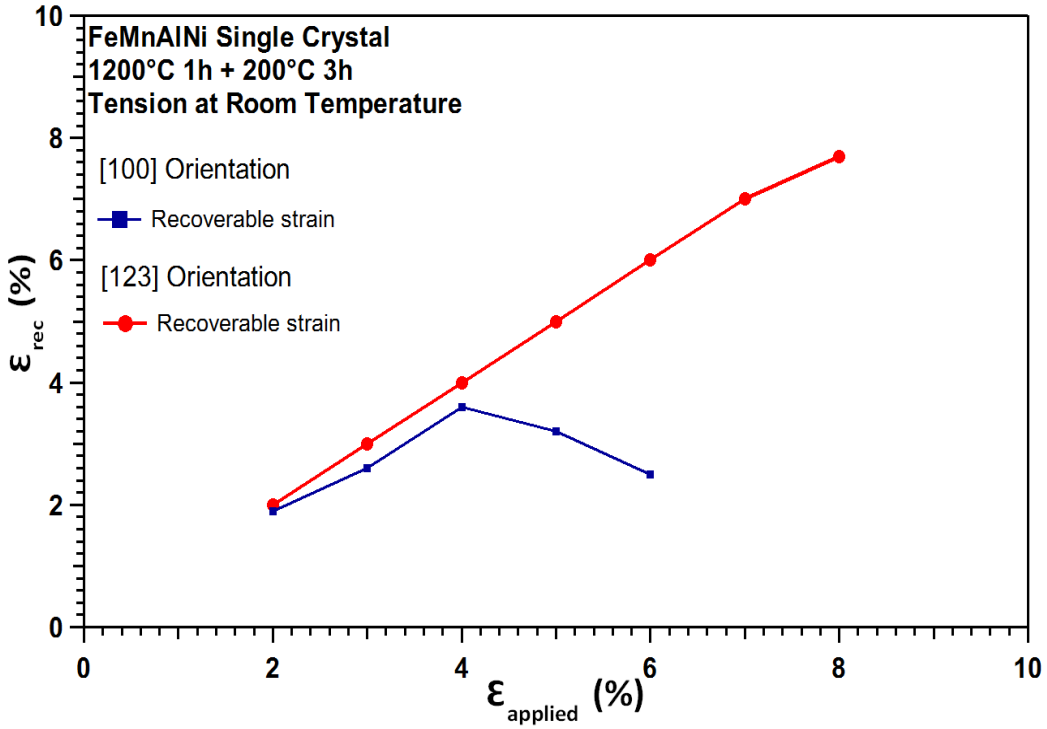

Figure 6.15 Recoverable strain as a function of applied strain in the $Fe_{43.5}Mn_{34}Al_{15}Ni_{7.5}$ single crystals with the [100] and [123] orientations aged at 200°C for 3 hours under tension test at room temperature.

6.5 Conclusions

In this study, the effect of the orientations on the stress-temperature phase diagram and superelastic strain were investigated in $Fe_{43.5}Mn_{34}Al_{15}Ni_{7.5}$ singe crystals with the [100], [111] and [123] orientations under both compression and tension. The results demonstrated that the recoverable strain, critical stress, stress hysteresis and the slope of the Clausius-Clapeyron line are strong function of crystallographic orientation. Theoretical transformation strain, detwinning strain and RSSFs were calculated based on

the energy minimization theory and lattice deformation theory. The main conclusions are listed as follows:

(1) The different slopes in the [100], [111] and [123] orientations are related to the transformation strain. For the solution-treated sample, the [100] orientation has the smallest slope of stress-temperature curve than that in the [123] and [111] orientations. The maximum transformation strain in the [100] orientation corresponds to the smallest Clausius-Clapeyron slope. In other words, the minimum transformation strain in the [111] orientation results in the largest slope of CC curve. The different critical stress for stress-induced martensitic transformation in the [100], [111] and [123] orientations are related to the RSSF. The critical stress for stress-induced martensitic transformation in the [100] orientation is lower than it in the [111] and [123] orientations because the largest RSSF is in the [100] orientation.

(2) The maximum recoverable strains in aged single crystals with the [100], [123] and [111] orientations are 8.2%, 6.4% and 1.9%, respectively. Aging heat treatment reduces the orientation dependence of the Clausius-Clapeyron slope. On the contrary, solution-treated samples exhibit the strong orientation dependence of the Clausius-Clapeyron slope.

(3) The difference of the recoverable strain in both [100] and [123] oriented aged samples is related to numbers of martensite variants. The martensitic

transformation in the [100] orientation under tension is more favor to the detwinning mechanism, which forms a single martensite variant. The tensile deformation cannot be easily accommodated by one martensite variant. As a result, the high density of parallel and hairpin-shaped dislocations generate at the austenite-martensite interface and in austenite matrix. The dislocations enlarge the stress hysteresis loop and decrease the recoverability. In contrast to the [100] orientation, multiple martensite variants can activate in the [123] orientation and the tensile deformation mechanism in the [123] orientations is the CVP deformation. Formation of CVP strain can easily accommodate the tensile deformation and decrease the density of dislocations generate at the austenite-martensite interface and in the austenite matrix.

CHAPTER VII

EFFECT OF MICROSTRUCTURE ON SUPERELASTICITY IN FeMnAlNi ALLOYS UNDER TENSION

The first part of this chapter is focused on thermomechanical processing on the polycrystalline sheet. This study is to investigate the effect of thermomechanical processing on the microstructure and hardness of the polycrystals alloy sheet. The different phases with various shapes, which appear in $Fe_{43.5}Mn_{34}Al_{15}Ni_{7.5}$ polycrystals alloys after thermomechanical processing, is examined by OM, WDS, XRD and hardness tests. Based on the experimental results, the thermomechanical processing will be selected to proceed on the polycrystals sheet for the second part of study. The second focus in this chapter is to investigate the effect of grain size on superelastic properties such as superelastic strain, critical stress for stress-induced martensitic transformation and ductility. The various grain sizes in the tensile samples are obtained by the cyclic heat treatment. The superelastic properties were performed by the incremental strain tensile test at room temperature.

7.1 Microstructural Characterization and Microhardness in FeMnAlNi Alloys

For the microstructural characterization (optical microscopy and composition analysis) and microhardness test, the cylindrical sample with the 3.175 cm diameter by 5 mm thickness was solution-treated at 1200°C for 1 hour to homogenize the samples and followed by quenching into ice water. The small disc samples were cut from the solution-treated cylindrical sample and subsequently heat treated at various temperatures (800°C, 900°C, 1000°C, 1100°C, 1150°C) for 1 hour followed by quenching into water.

7.1.1 Microstructure and Composition of fcc Phases

Figure 7.1a shows the optical microscopy of the FeMnAlNi alloys solution heat treated at 1200°C for 1 hour. We observe both the fcc martensite and bcc austenite at room temperature in the solution-treated sample because the austenite finish temperature is higher than room temperature (SQUID profile for the solution-treated sample is shown in Appendix C). In order to study the various phases in different temperatures, solution-treated samples are heat treated at with different temperatures (800°C, 900°C, 1000°C, 1100°C and 1150°C) and show in Figure 7.1b-f. From the results, various shapes of these second phases are seen in bcc austenite. These second phases grow along the grain boundaries (grain-boundary allotriomorphs), out from grain boundaries (Widmanstattn sideplates) and inside the grains (intragranular phase) [104-108]. These fcc second phases has also observed in FeMnAlNC alloys [104-108].

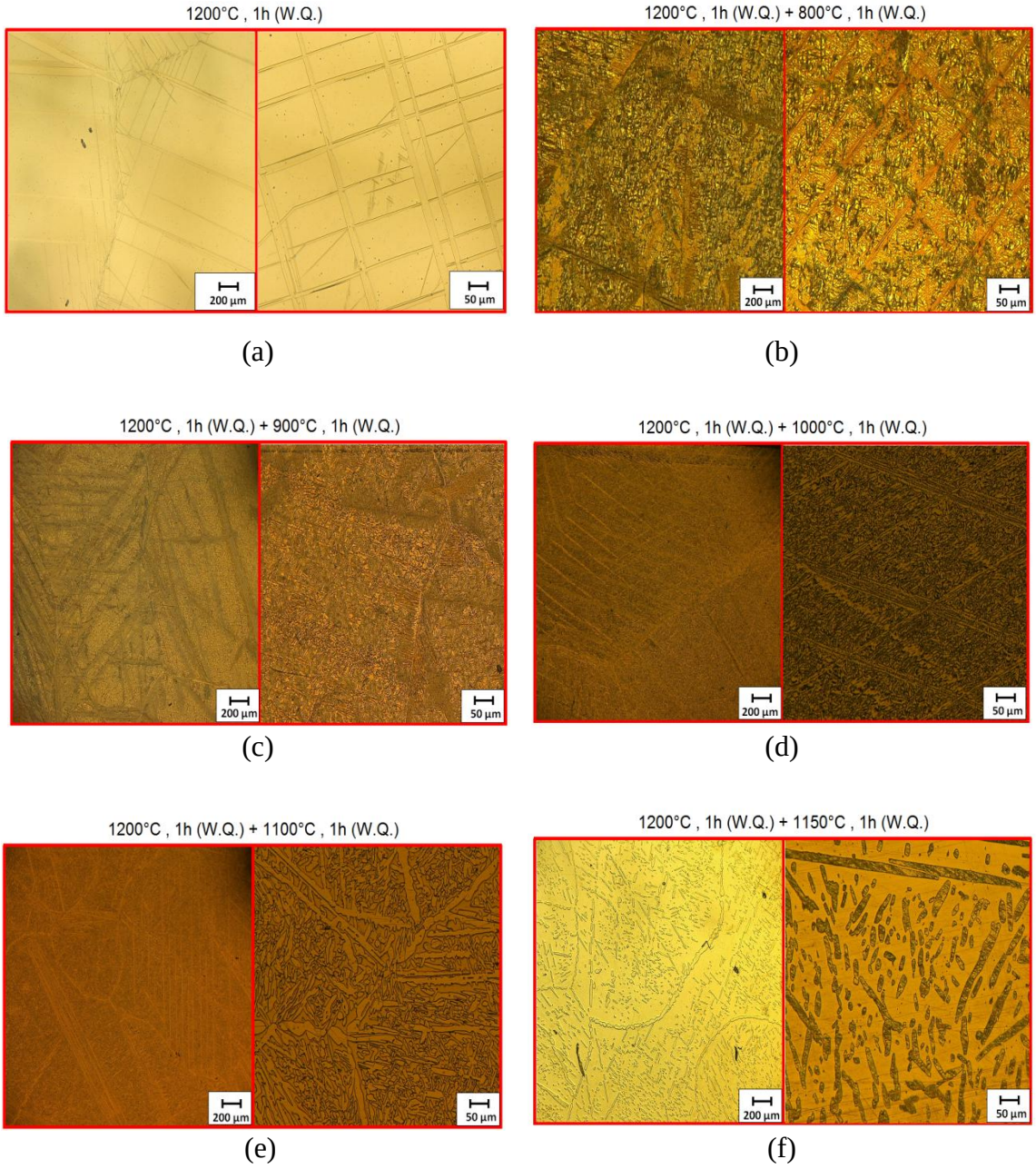

Figure 7.1 The FeMnAlNi alloy were solution heat treated at 1200°C for 1 hour and then heat treated at (a) 800°C, (b) 900°C, (c) 1000°C, (d) 1100°C and (e) 1150°C for 1 hour.

The room temperature BSE images of the solution-treated FeMnAlNi alloys heat-treated at 800°C, 900°C, 1000°C, 1100°C and 1150°C for 1 hour ARE shown in Figure 7.2. The numbers in the figures indicates the position for composition analysis. Because the large volume fraction of fcc second phases are in 1200°C , 1h + 800°C , 1h, 1200°C , 1h + 900°C , 1h and 1200°C , 1h + 1000°C , 1h samples and are difficult to observe the austenite phases from the low magnification of BSE images, the high magnification of BSE images are used for showing the austenite phase in these three samples.

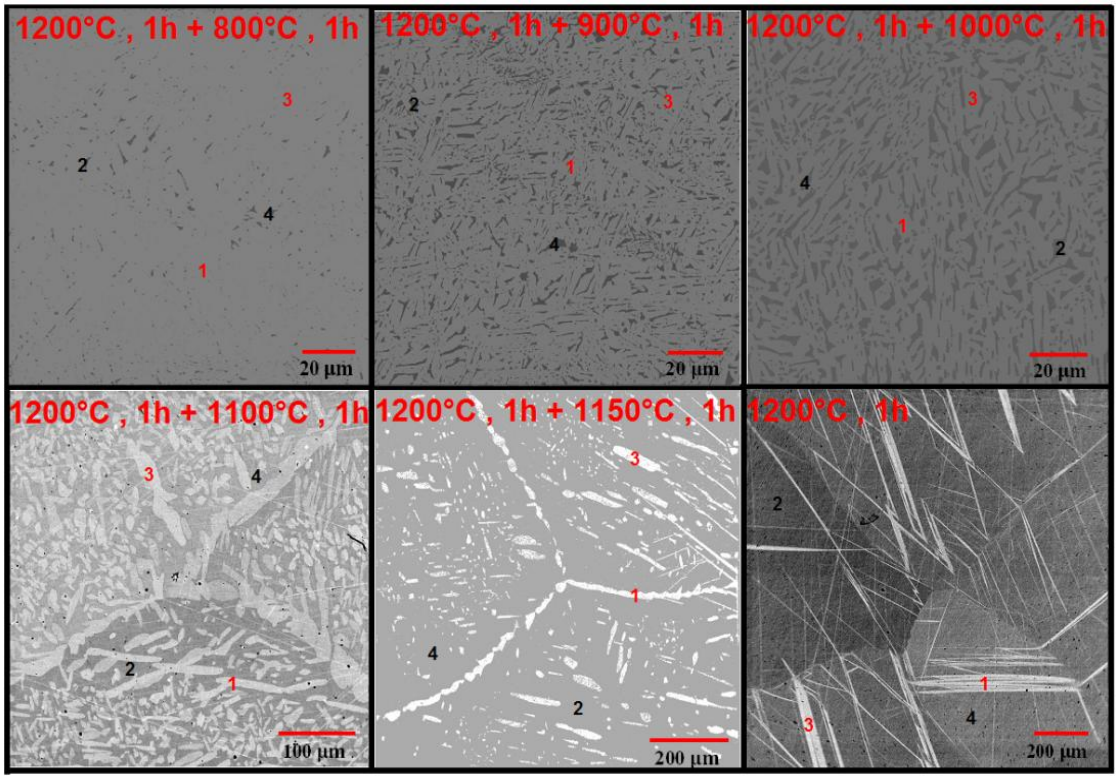

Figure 7.2 SEM images of FeMnAlNi alloys were solution heat treated at 1200°C for 1 hour and then heat treated at (a) 800°C for 1 hour, (b) 900°C for 1 hour, (c) 1000°C for 1 hour, (d) 1100°C for 1 hour, (e) 1150°C for 1 hour. Numbers 1 and 3 are analyzed on the fcc phases and numbers 2 and 4 are analyzed on the bcc phases.

Table 7.1 shows the WDS analysis results of FeMnAlNi alloy in different heat treatment conditions. The Numbers (1 and 3) and the numbers (2 and 4) in Figure 7.2 represent that the composition analysis are taken from the austenite matrix and the fcc second phases or fcc martensite, respectively. The composition analysis of these fcc phases is summarized in Figure 7.3.

Table 7.1 The composition analysis of FeMnAlNi alloy in different heat-treated conditions. Numbers 1 and 3 are analyzed on the fcc phases and numbers 2 and 4 are analyzed on the bcc phases.

Sample conditions		Fe (at%)	Mn (at%)	Al (at%)	Ni (at%)
1200°C,1h + 800°C,1h	**#1**	43.36	34.29	14.69	7.66
	#2	43.36	33.76	15.19	7.7
	#3	44.46	35.39	14.59	7.56
	#4	43.31	33.79	15.12	7.68
1200°C,1h + 900°C,1h	**#1**	46.51	35.37	13.18	4.94
	#2	29.52	22.75	27.49	20.24
	#3	45.74	35.55	13.33	5.39
	#4	30.86	23.31	26.76	19.08
1200°C,1h + 1000°C,1h	**#1**	44.24	35.51	13.59	6.67
	#2	38.95	30.08	19.51	11.47
	#3	44.41	35.58	13.58	6.64
	#4	37.76	29.04	20.73	12.47
1200°C,1h + 1100°C,1h	**#1**	44.28	35.34	13.36	7.02
	#2	42.42	32.82	16.65	8.11
	#3	44.23	35.37	13.36	7.05
	#4	42.26	32.7	16.69	8.15
1200°C,1h + 1150°C,1h	**#1**	44.78	35.24	12.91	7.08
	#2	43.09	33.53	15.65	7.73
	#3	44.69	35.37	12.89	7.05
	#4	43	33.54	15.73	7.73
1200°C,1h	**#1**	43.37	33.9	15.26	7.47
	#2	43.14	34.86	15.32	7.48
	#3	43.33	34.85	15.3	7.52
	#4	43.38	33.86	15.28	7.48
Nominal composition		43.5	34	15	7.5

From the results, the fcc second phases (800°C, 900°C, 1000°C, 1100°C and 1150°C) have high Fe and Mn contents and less Ni and Al contents compare to nominal composition of FeMnAlNi. The composition of fcc martensite phase in the solution-treated FeMnAlNi alloy is the same as nominal composition. In the previous effect of aging heat treatment on superelasticity study (chapter 5), the bcc precipitates are enriched in Ni and Al, while depleted in Fe and Mn.

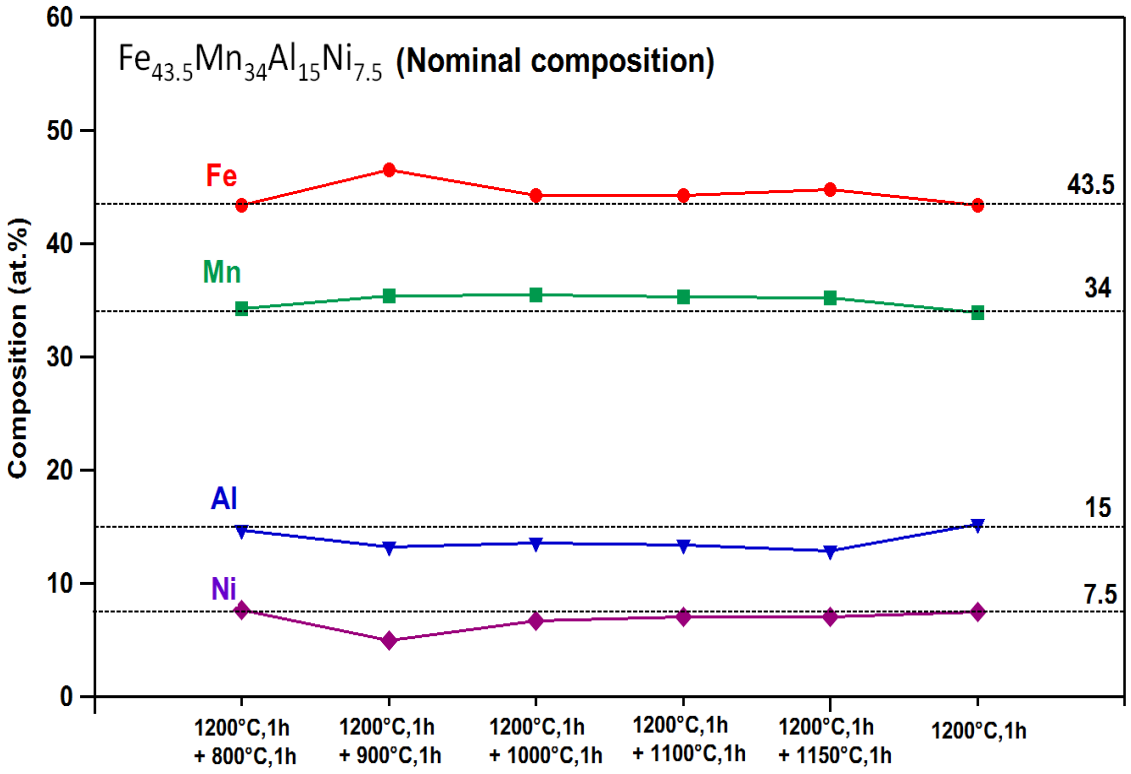

Figure 7.3 The composition of fcc phases for the solution-treated FeMnAlNi alloy heat treated at 800°C, 900°C, 1000°C, 1100°C, 1150°C for 1 hour.

7.1.2 Vickers Microhardness

Figure 7.4 shows the microhardness of FeMnAlNi alloys in different heat treating conditions. From the results, the highest hardness value is in the solution-treated samples because the most of phases is the austenite. The hardness values decrease after the solution-treated samples are heat-treated at 800°C, 900°C, 1000°C, 1100°C and 1150°C for 1 hour. The hardness value in 900°C is smallest than those in the solution-treated samples and another heat-treated samples.

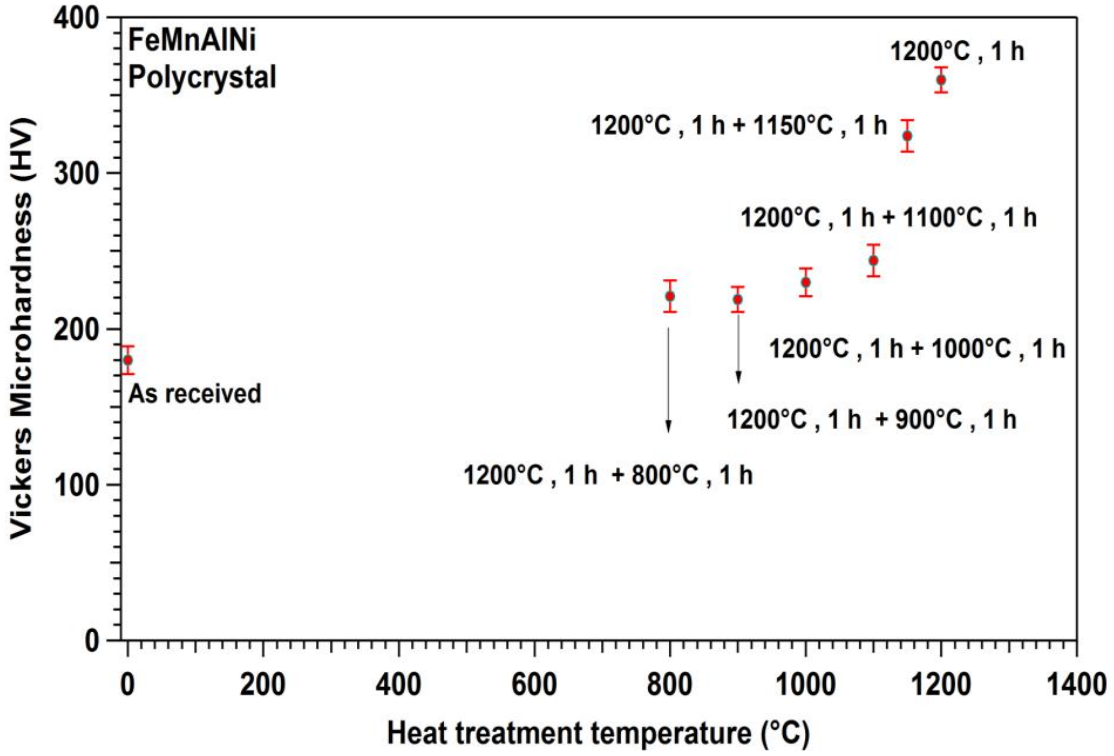

Figure 7.4 Vickers Microhardness in $Fe_{43.5}Mn_{34}Al_{15}Ni_{7.5}$ alloys for as received samples and the samples heat treated at different temperatures.

7.2 Thermomechanical Processing in FeMnAlNi Alloys

7.2.1 Hot-Rolled + Cold-Rolled Experiment

Based on the heat treatment studies, heat treatment temperatures below 1200°C are not high enough for homogenized the samples and inhomogeneous sample is difficult for the hot-rolled experiment. In NiTi SMAs, the ingot was heat treated at 900°C to homogenize the sample for hot-rolled experiment [1]. As a result, the test temperature 1200°C was selected for the hot-rolled test.

Figure 7.5 is a schematic displaying thermomechanical processing of experiment 1 and the OM images inside the figure are (a) as cast (b) hot-rolled (c) hot-rolled + cold-rolled. The polycrystals ingot with the dimension 15×48×10 mm (length × width × height) is hot rolled to 4.2 mm in thickness, an approximately 47% reduction in thickness. Then, the hot-rolled sheet was cold rolled 76% to 1 mm thickness. However, the cracks generate along the grain boundaries and inside the grains after the cold-rolled experiment. Figure 7.6 shows the optical microscopy of FeMnAlNi hot-rolled alloy sheet. Various shapes of fcc phases (γ) are seen in bcc austenite regions (α). The grain-boundary allotriomorphs (GBAs) are generated along the grain boundaries. The Widmanstattn sideplates (WS) generally have an arrow, fishbone, or feather shapes grow out from the grain boundary region. The diamond or leaf shapes are seen in the interior of bcc grains, which is intragranular phase (IP). These second phases increase the hardness of FeMnAlNi alloy sheet and cause the cracks after the cold-rolled.

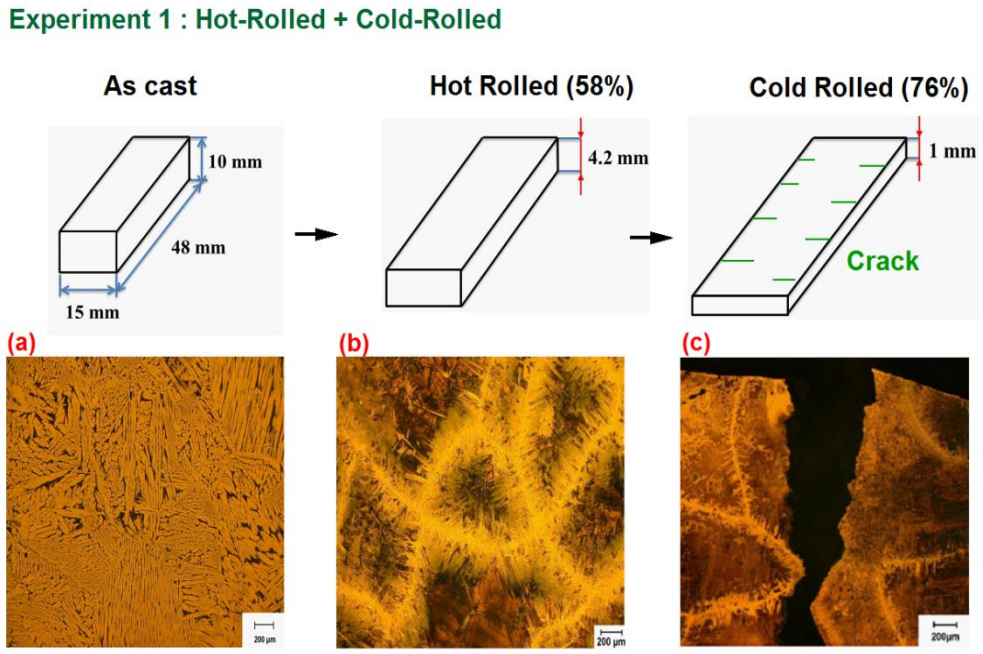

Figure 7.5 A schematic showing the thermomechanical process of the experiment 1. Inside the figure is the OM images of (a) as cast (b) hot-rolled and (c) hot-rolled + cold-rolled.

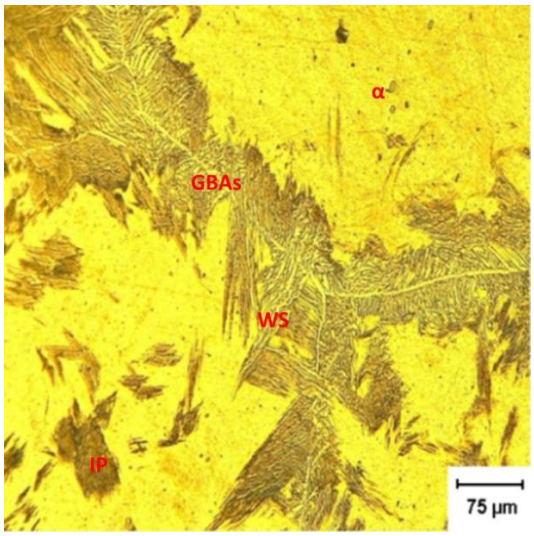

Figure 7.6 Microstructure of the hot-rolled FeMnAlNi sheet showing the various fcc phases.

7.2.2 Hot-Rolled + Solution Heat Treatment + Cold-Rolled Experiment

Based on the experiment 1 result, the fcc second phases generate along or grow from the grain boundaries after the hot-rolled experiment. These fcc phases increase the hardness values of the sheet and cause the cracks along the grain boundaries or inside the grains after the cold-rolled experiment. In the experiment 2, the hot-rolled sheet was first homogenized at 1200°C for 1 hour and quenched into water to remove these second phases from the grain boundaries and grains. Then, the homogeneous sheet was cold rolled to 1 mm in thickness at a thickness reduction ratio of 76%. Figure 7.7 is a schematic displaying thermomechanical processing of the experiment 2 and the OM images inside the figure are (a) hot-rolled + 1200°C,1h. (b) hot-rolled + 1200°C, 1h + cold-rolled. However, the grain boundary cracking occurs after the cold-rolled experiment. We believe since the major phase is the austenite phase after the solution heat treatment, the cold rolled of austenite phase is difficult.

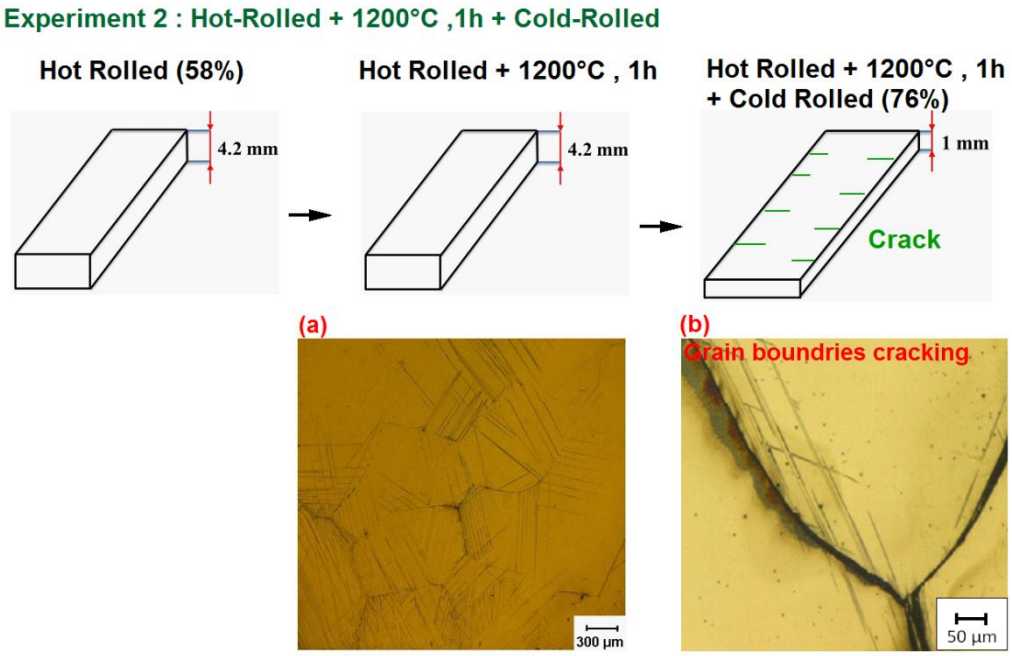

Figure 7.7 A schematic showing the thermomechanical processing of the experiment 2. Inside the figure is the OM images of (a) hot-rolled + 1200°C , 1h and (b) grain boundaries rupture after the cold-rolled test.

7.2.3 Hot-Rolled + Annealing Heat Treatment + Cold-Rolled Experiment

Based on the experiment 2 results, the sheet with the single austenite phase is difficult for the cold-rolled experiment. In order to obtain the cold-rolled ability, the hot-rolled sheet was annealed at 900°C for 1 hour and quenched into water to obtain the duel phases where bcc phase is mixed with the fcc phase. Then, the annealing sheet was cold-rolled (76%) to 1 mm in thickness. No cracks generate in the sheet after the cold-rolled experiment. Figure 7.8 is a schematic displaying thermomechanical processing of the experiment 3 and the OM images inside the figure are (a) hot-rolled + 900°C , 1h. (b) hot-rolled + 900°C , 1h + cold-rolled.

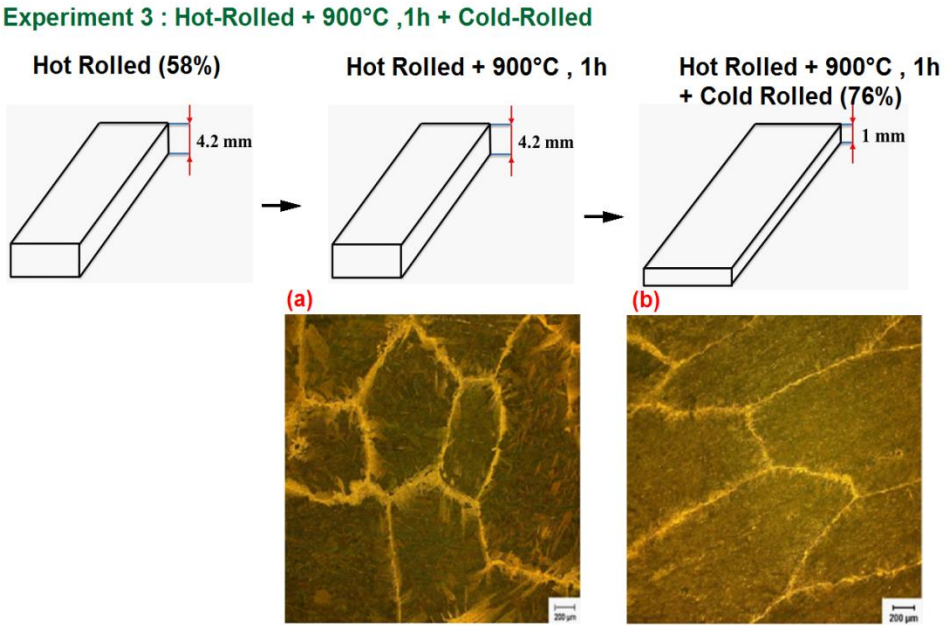

Figure 7.8 A schematic showing the thermomechanical process of the experiment 3. Inside the figure is the OM images of (a) hot-rolled + 900°C , 1h and (b) hot-rolled + 900°C , 1h + cold-rolled.

The 900°C was selected for the annealing heat treatment temperature is based on the hardness results. From the previous hardness results, the hardness values in 900°C is smallest than those in another heat treatment conditions (800°C, 1000°C, 1100°C, 1150°C and 1200°C). Figure 7.9 shows the microhardness values of as cast, hot-rolled, hot-rolled + 1200°C , 1h and hot-rolled + 900°C , 1h. From the results, the hardness value of hot-rolled sheet was decreased after annealed at 900°C for 1 hour. Therefore, the small hardness value of annealing sheet reduces the formation of cracks after the cold-rolled experiment.

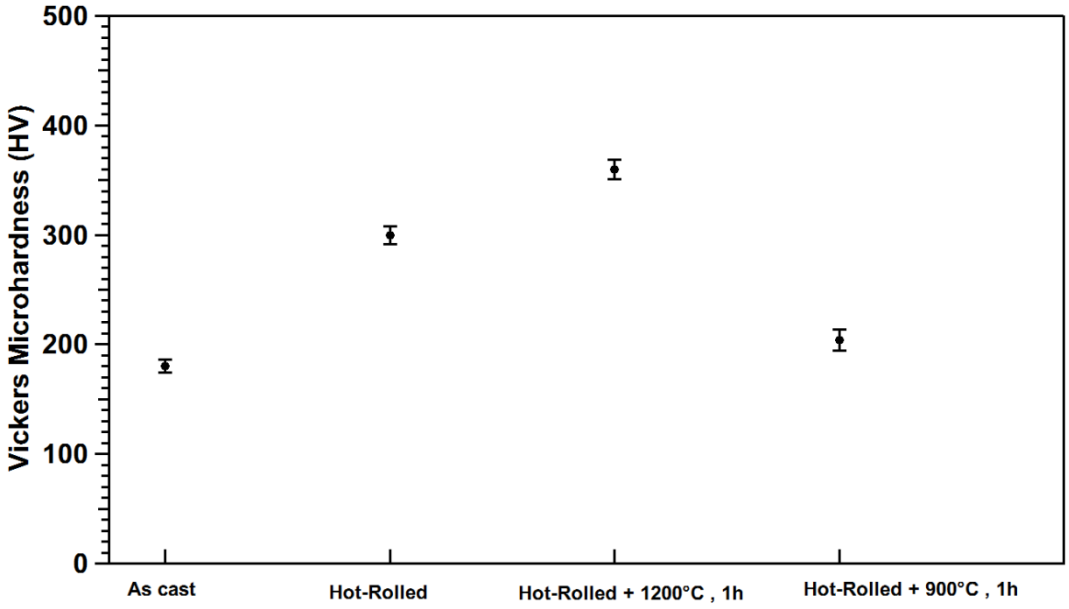

Figure 7.9 Microhardness of FeMnAlNi alloys sheet in different thermomechanical processing conditions. (a) as cast (b) hot-rolled (c) hot-rolled + 1200°C , 1h and (d) hot-rolled + 900°C , 1h.

Figure 7.10 shows the XRD patterns taken from the FeMnAlNi alloy sheets (a) as cast (b) hot-rolled (c) hot-rolled + anneal heat treatment (900°C , 1h) (d) hot-rolled + anneal heat treatment (900°C , 1h) + cold-rolled. From the XRD results, the major phases in the as-received sample are the fcc phases. The fcc peaks are in (110), (200) (220) and (311). The bcc peak is in (110). The lattice parameters of the bcc and fcc phases are determined as $a_{bcc} = 2.879nm$ and $a_{fcc} = 3.652nm$, respectively. The intensity of bcc peaks in the hot-rolled samples increase in the (110), (200) and (211). The lattice parameters for hot-rolled samples are $a_{bcc} = 2.878nm$ and $a_{fcc} = 3.651nm$. After annealing heat treatment, the intensity of f.c.c. (111) peaks increase. The intensity of bcc peaks decrease after the cold-rolled test due to deformation induced martensitic

transformation. This means most of the austenite phase transforms to the martensite phases after large deformation. The lattice parameters for hot-rolled+900°C , 1h + cold-rolled sample are $a_{bcc} = 2.907nm$ and $a_{fcc} = 3.649nm$.

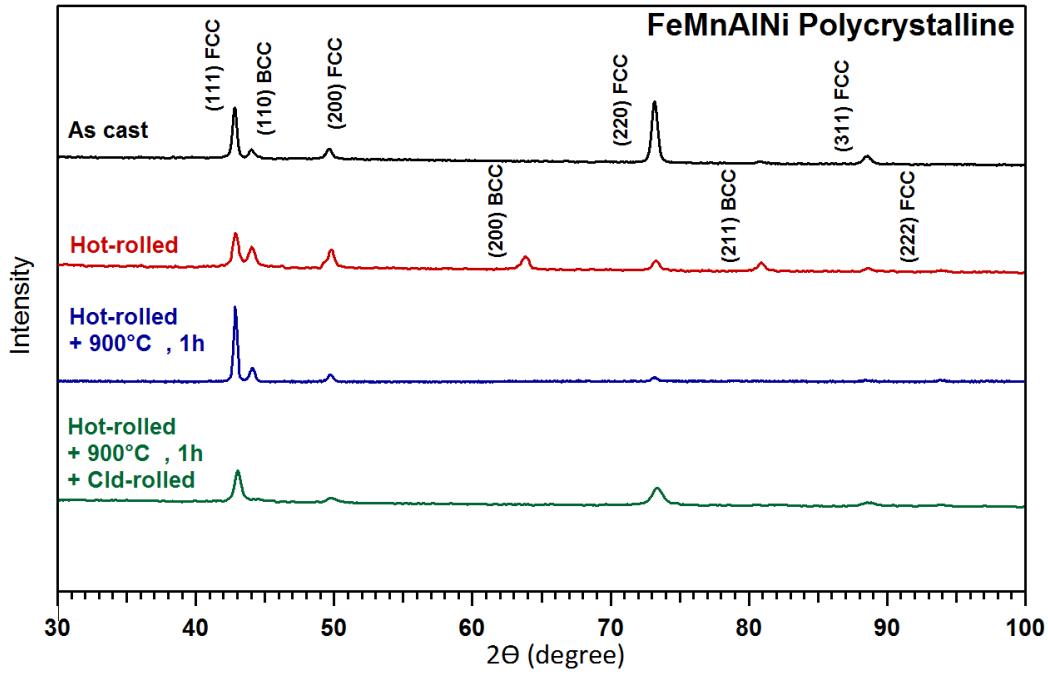

Figure 7.10 XRD patterns taken from FeMnAlNi alloy sheet (a) as cast (b) hot-rolled (c) hot-rolled + 900°C , 1h and (d) hot-rolled + 900°C , 1h + cold-rolled.

7.3 Effect of Grain Size on Superelasticity in the FeMnAlNi Alloys

In this study, the tensile samples are cut from the cold-rolled sheet. For the grain growth, the tensile samples are heat-treated at 1200°C for 0.5 hours and followed by air cooling (AC) to room temperature. Because the fcc second phases generate in the samples after the air cooling process, the solution heat treatment is used to remove the second phases from the samples. Based on the effect of aging study (chapter 5), the samples aged at 200°C for 3 hours show the large superelastic strain at room temperature. As a result, the polycrystals are aged at 200°C for 3 hours to obtain the better superelastic properties.

The thermomechanical processing of $Fe_{43.5}Mn_{34}Al_{15}Ni_{7.5}$ (at.%) polycrystals sheet can summary as follows: (1) hot-rolled (HR) at 1200°C to 4.2 mm in thickness, (2) annealing heat treatment (AHT) at 900°C for 1 hour in the fcc + bcc two-phases region, (3) cold-rolled (CR) to 1 mm in thickness with a reduction ratio of 76%. (4) cyclic heat treatment at 1200°C for 0.5 hours and followed by air cooling (AC) to room temperature for the grain growth, (5) solution heat treated (SHT) at 1200°C for 1 hour and follow by quench into water, and (6) aging or precipitation heat treatment (PHT) at 200°C for 3 hours and quenching into water. Figure 7.11 shows the schematic illusion of the thermomechanical process of FeMnAlNi polycrystalline sheet. The tensile samples with the gauge dimension 1.5 mm × 3 mm × 8 mm were cut from the cold-rolled sheet. Furthermore, the large grains size can be obtained by repeating the heat treated at 1200°C for 0.5h followed by air cooling to room temperature.

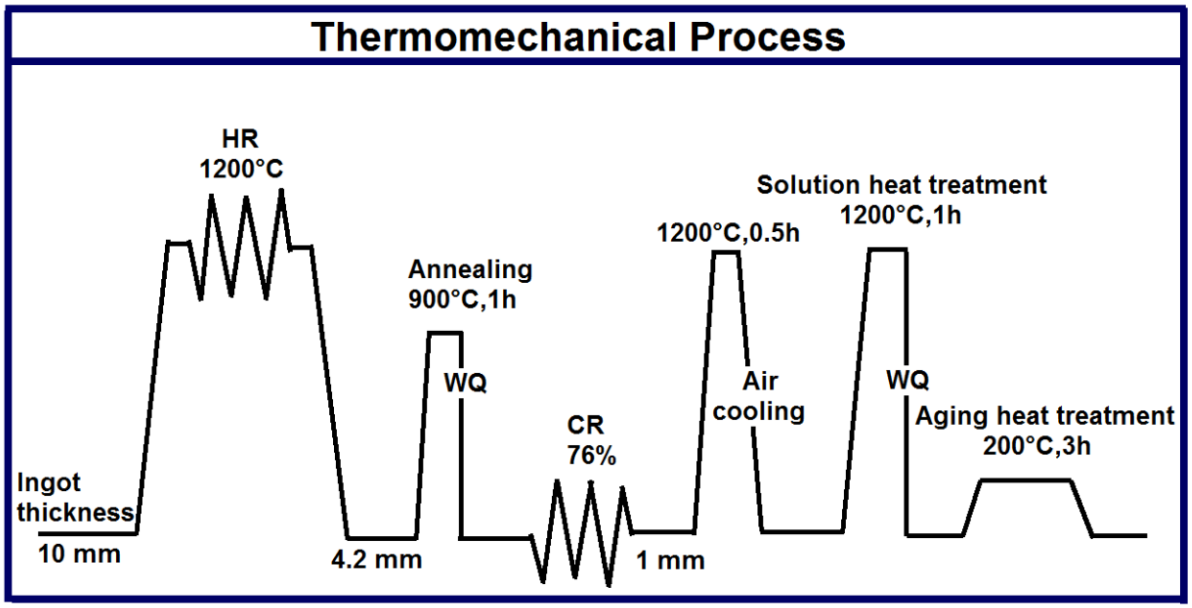

Figure 7.11 Schematic illustration of the thermomechanical processing in FeMnAlNi alloys sheet.

The microstructure of the $Fe_{43.5}Mn_{34}Al_{15}Ni_{7.5}$ tensile samples after two times air cooling process (2AC), 5AC and 10AC are shown in Figure 7.12a, b and c. The OM images are taken at the gauge section of tensile sample. From the OM result, the grain is continued to grow with cyclic the heat treatment processes. The large grain size around 6mm is obtained in the 10AC sample. The reason is that the subgrain structure was formed through cyclic heat treatment process or bcc-fcc phase transformation. With increasing the cyclic heat treatment process, the subgrains start to engulf the neighboring grains and form the large grains [144,145]. This phenomenon is reported by Omori et al. [144] in the Cu-based SMAs and named abnormal grain growth (AGG). No subgrains were observed without cyclic heat treatment [144]. It should be note that the fcc second phases generate along the grain boundaries or inside the austenite bcc grains after the air

cooling processes. These second phases are named as Widmanstatten side plate and grain boundary allotriomorphs, respectively [104-108]. Because the fcc second phases do not transform with the matrix during the martensitic transformation, they will suppress the recoverable strain during the reverse martensitic transformation. In order to remove these fcc second phases, the tensile samples after the air cooling process are solution heat treated at 1200°C for 1 hour. The tensile samples after the solution-treated are shown in Figure 7.12d, e and f. The grain size in three different heat treatment samples is 2 mm in 2AC+SHT samples, 5 mm in 5AC+SHT and 6 mm in 10AC+SHT samples. There are no second phases along the grain boundaries or inside the grains after the solution heat treatment. Most of the phase is the austenite phase.

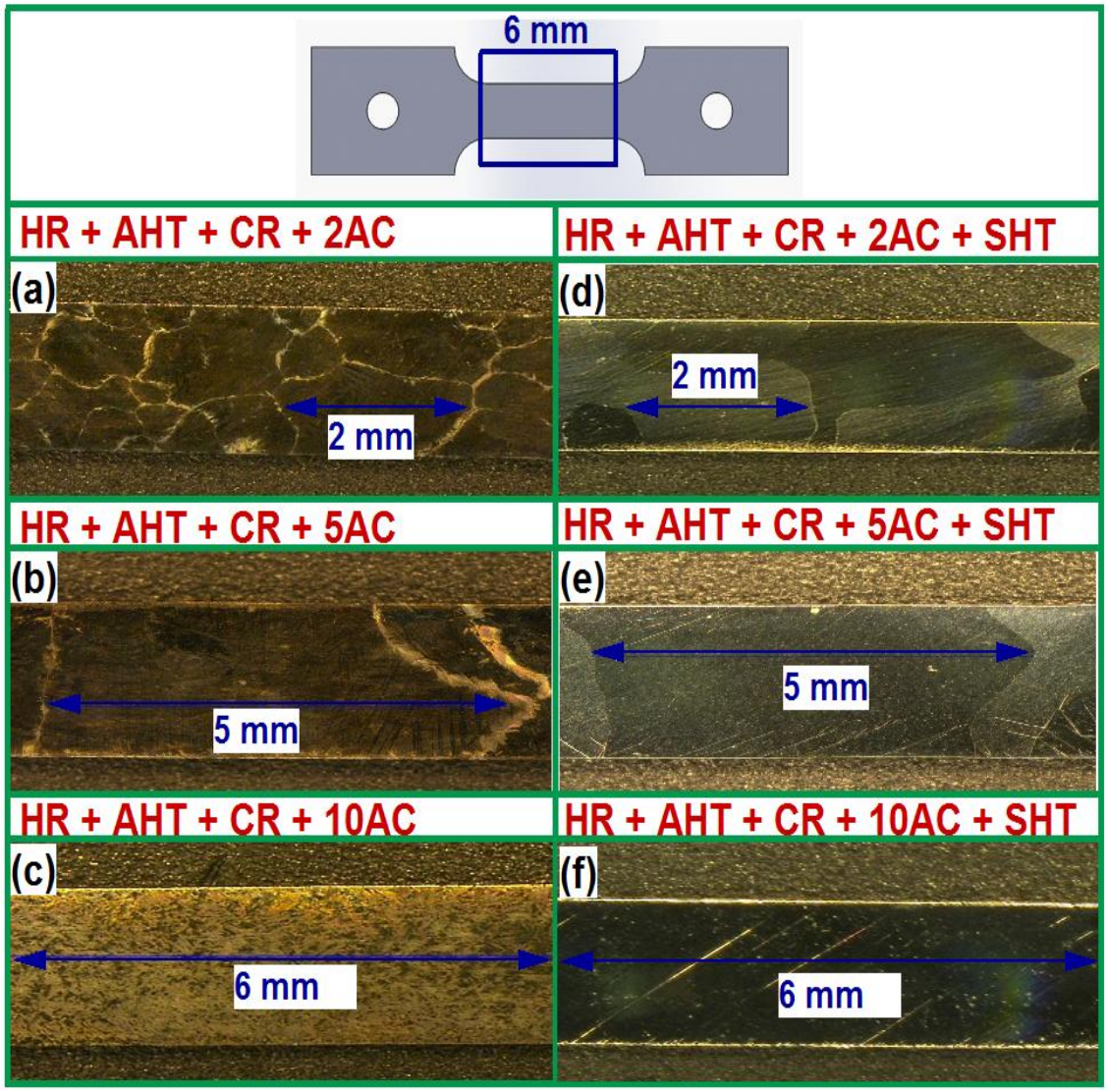

Figure 7.12 Optical microscopy of tensile samples in different thermomechanical processing (a) HR+AHT+CR+2AC, (b) HR+AHT+CR+5AC (c) HR+AHT+CR+10AC, (d) HR+AHT+CR+2AC+SHT, (e) HR+AHT+CR+5AC+SHT and (f) HR+AHT+CR+10AC+SHT.

The RD, TD and ND are represented rolling direction, transverse direction and normal direction of the FeMnAlNi sheet. The tension samples were cut from the rolling direction. Figure 7.13 shows the inverse pole figures for the tension sample in different heat treatment conditions.

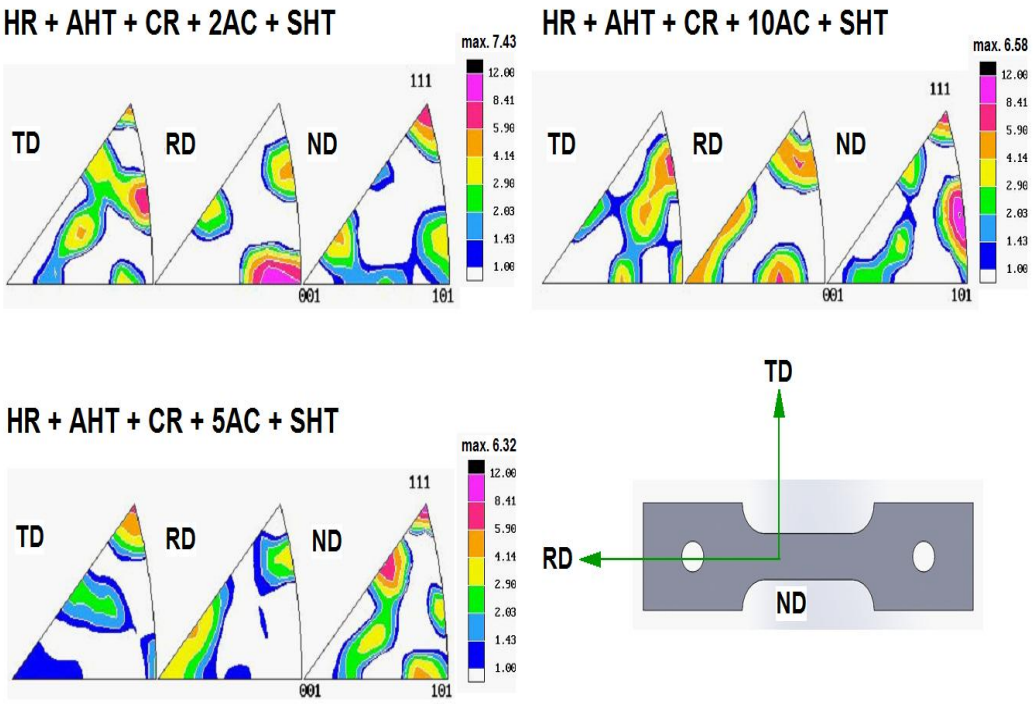

Figure 7.13 Inverse pole figures for the FeMnAlNi tensile samples in different thermomechanical processing conditions.

The superelastic properties are evaluated by incremental tensile strain testing at room temperature. The limit strain increases (1%, 2% ….) until the sample fracture. Figure 7.14a and b show the tensile stress-strain curves in FeMnAlNi with d=2 mm and d=5 mm, respectively. The relationship between superelastic strain and applied strain in 2AC+SHT+PHT and 5AC+SHT+PHT samples are summarized in Figure 7.14c. Table 7.2 shows the grain size (d), critical stress (σ_c), fracture stress (σ_f), superelastic strain (ε_{SE}), and tensile elongation (ε_{el}) in FMAN alloy. From the results, the critical stress for stress-induced martensitic transformation (σ_c) is high (around 740 MPa) in the tension sample (2AC+SHT+PHT) with the grain size around 2 mm and maximum superelastic strain ($\varepsilon_{Max.}$) is small (1%). The ductility is around 4%. On the other hand, the tensile sample (5AC+SHT+PHT) with d=5 mm exhibits the lower σ_c of 240 MPa, better ductility before fracture (9%) and maximum superelastic strain about 3%. The results indicate the critical stress decreases and superelastic strain and ductility improve with increasing the grain size in FeMnAlNi alloy.

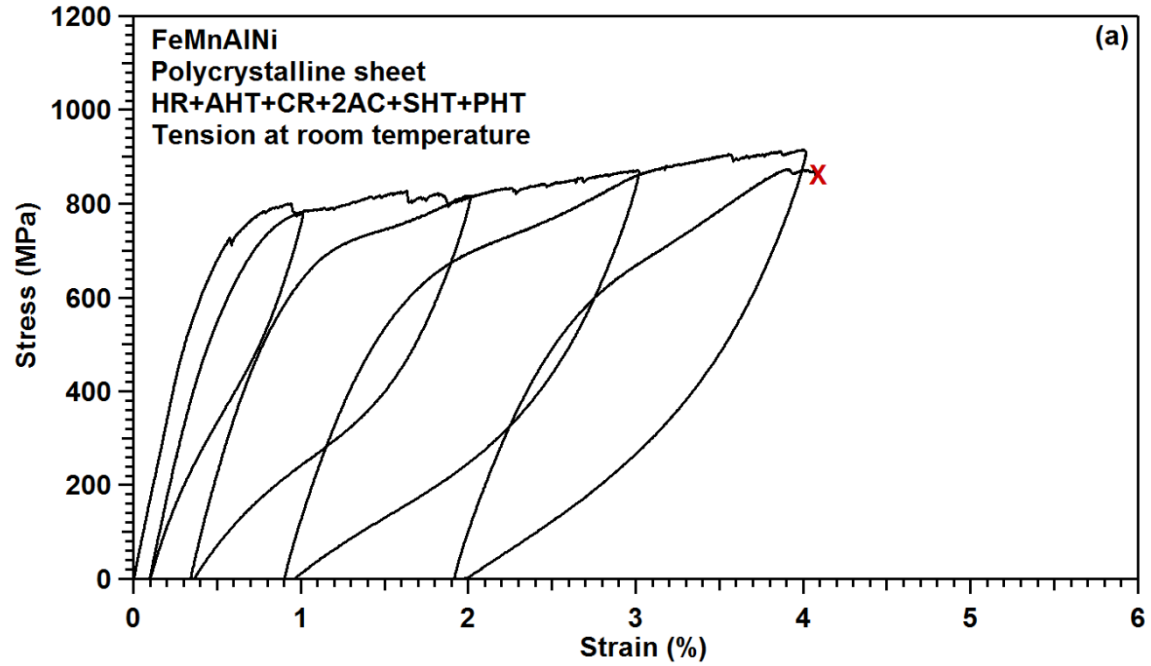

(a)

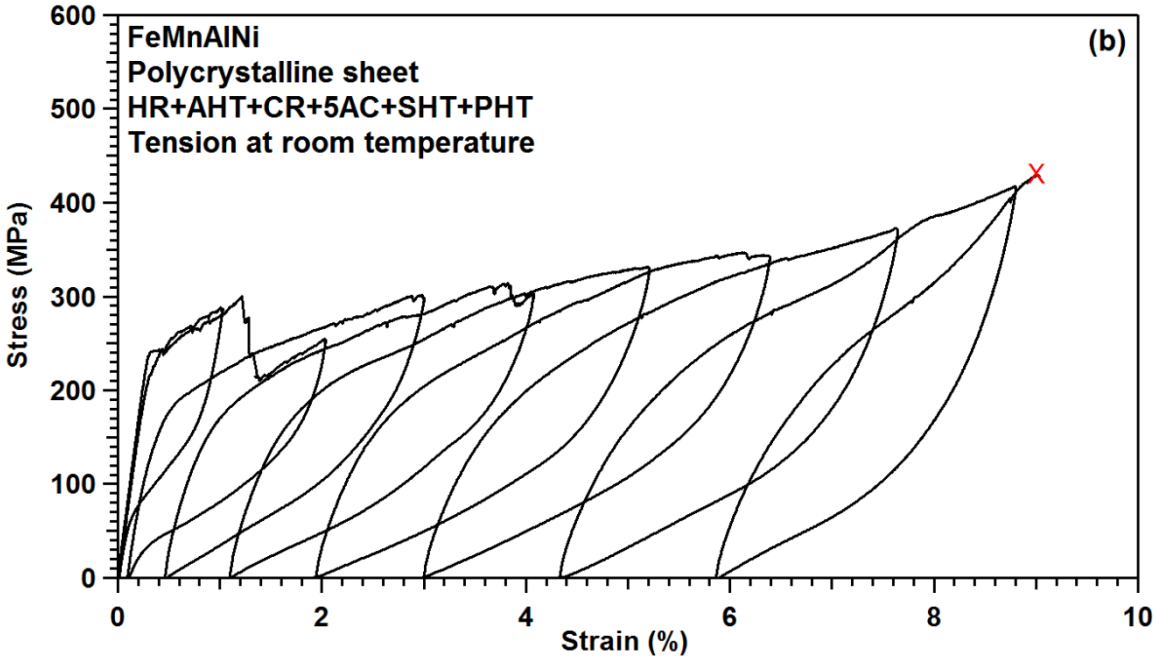

(b)

Figure 7.14 Tensile stress-strain responses of FeMnAlNi alloy sheet with different thermomechanical processes (a) HR+AHT+CR+2AC+SHT+PHT and (b) HR+AHT+CR+5AC+SHT+PHT. (c) Superelastic strain as a function of applied strain.

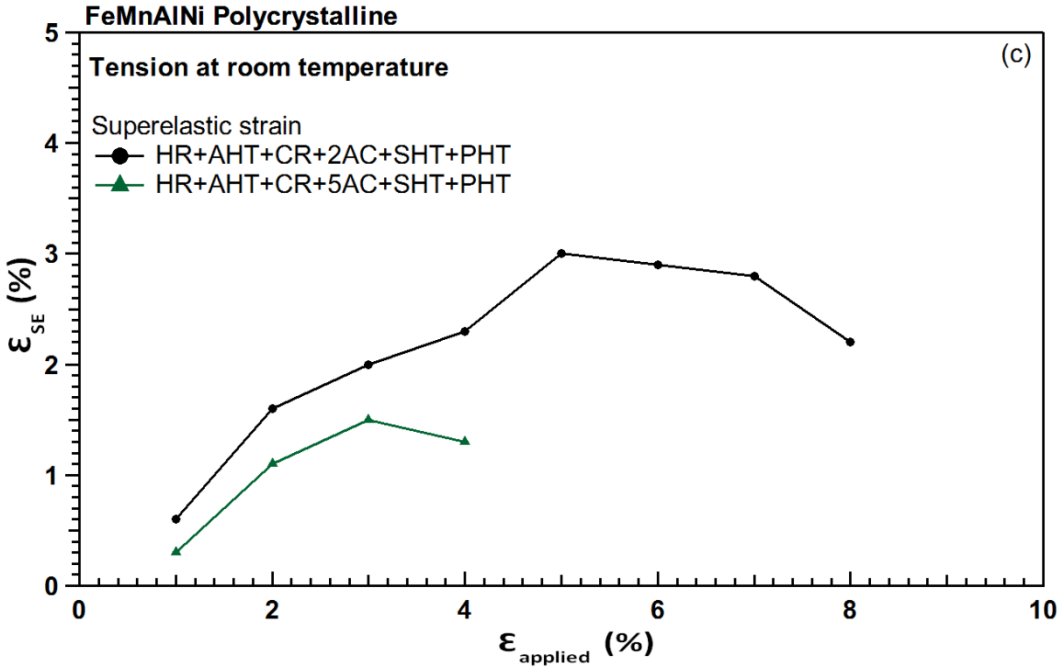

(c)

Figure 7.14 Continued

Table 7.2 Grain size (d), critical stress (σ_c), fracture stress (σ_f), superelastic strain (ε_{SE}), tensile elongation (ε_{el}) in FMAN alloy.

Sample condition	d (mm)	σ_c (MPa)	σ_F (MPa)	ε_{max} (%)	ε_{el} (%)
HR+AHT+CR+ 2AC+SHT+PHT	2	730	890	1	4
HR+AHT+CR+ 5AC+SHT+PHT	5	240	430	3	9

In polycrystals, the numerical calculation of superelastic properties such as superelastic strain and critical stress for stress-induced martensitic transformation are obtained by using two simulation models, one is Taylor model [146,147] and the other is Sachs models [148]. In the Taylor model, the grain constraint effect in the stress-induced martensitic transformation is considered. As a result, the model is generated the large

critical stress and small superelastic strain. On the contrary, in the Sachs model, the effect of grain constraints is ignored and less grain constraints results in large superelastic strain and small critical stress.

Figure 7.15 illustrates the different grain size in the gauge section of the tension samples. The small grains are formed in the 2AC+SHT+PHT samples. The small grain size causes the large boundary constraint from the surrounding grains due to the incompatibility at grain boundaries. Therefore, the large critical stress and small superelastic strain is obtained. For the 5AC+SHT+PHT samples, when the grain size becomes large, the grain boundary constraint decreases and each grain can almost be independently transformed to the martensite phase with less grain boundary constraint during the superelastic test. Therefore, the stress-strain response in the 5AC+SHT+PHT sample shows the smaller critical stress and larger superelastic strain than those in 2AC+SHT+PHT sample.

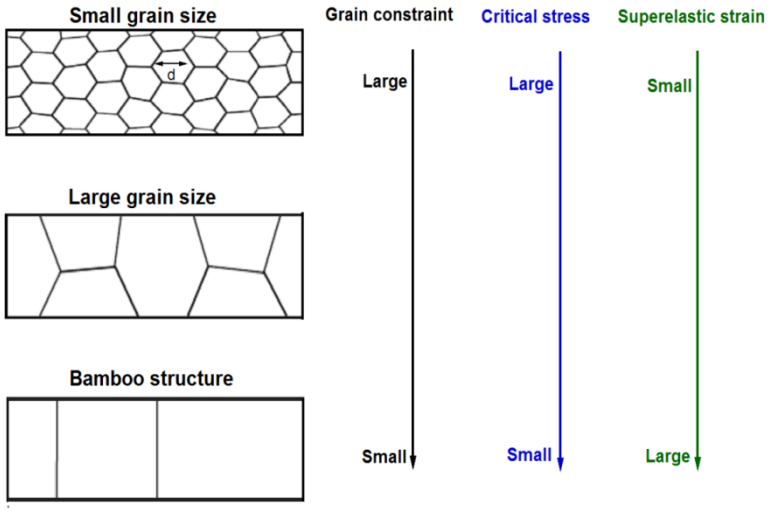

Figure 7.15 Schematic illustrations of the grain boundary constraint in the tension samples with various grain sizes.

7.4 Conclusions

The thermomechanical processing and effect of microstructure on superelasticity was investigated on the FeMnAlNi sheet. The main conclusions are listed as followed.

1. Hot-rolled sheet has the high hardness values due to formation of large volume fraction of fcc second phases. As a result, the cracks appear after cold rolled experiment. In order to obtain the cold-workability, the hot-rolled sheet was annealed at 900°C for 1h to obtain the duel phases (fcc + bcc). Therefore, the cold-rolled on the sheet is practical.
2. For the grain growth process, the sample was heated treatment at 1200°C for 0.5 hour followed by air cooling to room temperature. The large grain size can obtain by repetition of this process for 5 times.
3. The stress-strain responses such as critical stress, ductility and recoverable strain influence by the grain size. The large grain size decreases the number of grain boundary constraint from the surrounding grains. Reducing the grain boundary constraint improves recoverable strain and ductility. On the other hand, the small grains cause the large grain constraint between neighboring grains due to incompatibility of transformation strain at grain boundary, resulting in large critical stress and small recoverable strain and ductility.

CHAPTER VIII

SUMMARY OF THE RESULTS AND CONCLUSIONS

The present study investigated the microstructure and superelastic response in $Fe_{43.5}Mn_{34}Al_{15}Ni_{7.5}$ single crystals and polycrystals. The following conclusions can be drawn from the study on $Fe_{43.5}Mn_{34}Al_{15}Ni_{7.5}$ single crystal:

1. In constant strain superelastic tests at various temperatures in both tension and compression, the superelastic responses of the single crystals aged at 200°C for 15 minutes show low values of stress-temperature slope under tension (0.54 MPa °C $^{-1}$) and compression (0.41 MPa °C $^{-1}$) over a wide temperature window between -80 °C and 160 °C.
2. In the incremental strain superelastic experiments at room temperature, the irrecoverable strain in both compression and tension is the retained martensite. The retained martensite cannot be easily recovered by heating significantly above austenite finish temperature due to pinning by dislocations. The TEM investigations of the compression samples show a mixture of austenite and martensite phases with relatively smooth phase interfaces. No hairpin-shaped or parallel dislocations are observed in the austenite matrix and austenite-martensite interface. On the other hand, the sample deformed under tension is almost fully martensitic, high density of straight parallel dislocations and hairpin-shaped dislocations are visible at the

austenite-martensite boundaries and in austenite matrix, respectively. These dislocations may be responsible for the reduction in recoverability by pinning the martensite phase.

3. The difference in the number of active martensite variants also contributes to the difference in the superelastic responses under tension and compression. In compression, two martensite variants are able to accommodate the transformation strain arising from the phase transformation. In contrast to compression, only one variant provide the transformation strain in tension accommodate the tension deformation. Therefore, high density of dislocations is generated and will limit the recoverability and amplify the hysteresis. The difference in stress hysteresis and shape of the stress-strain curves are also related to this difference in the number of active variants during the transformation.
4. Increasing the aging times at 200°C increases the size and volume fraction of B2 precipitates. Compare to aging temperature of 200°C, aging temperature of 300°C significantly influences the precipitate size than the precipitate volume fraction. The precipitate size in 300°C-1h aged sample is larger than that in 200°C-1h aged sample and the volume fraction of precipitate in both aging condition is similar, which suggests the change in the high hardness of aging temperature at 300°C is related to change in the size of precipitates. The precipitates are enriched in Ni and Al, while depleted in Fe and Mn.

5. In the stress-temperature phase diagram under both tension and compression, the critical stress increases as aging time increases at aging temperature of 200°C, which suggests the transformation temperatures tend to decreases with increasing the aging times.
6. Optimal superelastic properties (7.2% superelastic strain) are found for samples aged at 200°C for 3 hours with precipitate size around 6-10 nm, which represents a balance between sufficient precipitation hardening and avoidance of loss of coherency or excessive embrittlement. On the contrary, large precipitate size around 25-30 nm was formed in 300°C-1h sample and results in small superelastic strain in the samples.
7. The difference of aging effect on the superelastic properties of FeMnAlNi single crystal in both tension and compression is related to the difference of the martensite variant selection. In compression, two variants can easily accommodate the compressive deformation. Increasing the size of precipitates results in reduction of the stress hysteresis and improvement of the recoverable strain. In tension, one variant is difficult to accommodate the deformation. As a result, increasing the size of precipitates leads to more obstacles for the martensitic transformation, and thus large frictional energy generates during the martensitic transformation and causes the poor recoverable strain and large stress hysteresis.

8. Orientation is strongly affected the superelastic responses such as the stress-temperature slope, critical stress and transformation strain. For the solution-treated samples with the [100], [123] and [111] orientations under compression test, the [100] orientation has the smallest slope of stress-temperature curve than that in the [123] and [111] orientations, which is corresponding to the maximum transformation strain in the [100] orientation. The critical stress for stress-induced martensitic transformation in the [111] orientation is larger than it in the [100] and [123] orientations because the smallest RSSF is in the [111] orientation. The maximum recoverable strains in aged single crystals with the [100], [123] and [111] orientations are 8.2%, 6.4% and 1.9%, respectively. Aging heat treatment reduces the orientation dependence of the slope of Clausius-Clapeyron curve.
9. For [123] orientation, the single crystals aged at 200°C for 3 hours show the large recoverable strain around 7.8% under tension test at room temperature. The difference of tensile stress-strain response in single crystals with the [100] and [123] orientations aged at 200°C for 3 hours is related to the martensite variant selection. Only one martensite variant can accommodate the tension deformation in the [100] orientation. As a result, the high density of straight parallel dislocations and hairpin-shaped dislocations are generated at the austenite-martensite boundaries and in austenite matrix, respectively. These dislocations may be responsible for the reduction in recoverability by pinning the martensite phase. For the [123] orientation, multiple martensite

variants can easily accommodate the tensile deformation and reduce the formation of high density of dislocations. As a consequence, the tensile sample in the [123] orientation shows the perfect recoverable strain up to 7.8%.

The following conclusions can be drawn from the study on $Fe_{43.5}Mn_{34}Al_{15}Ni_{7.5}$ alloy:

1. FeMnAlNi alloy after thermomechanical processing show different various shapes of fcc phases: (1) grain-boundary allotriomorphs (GBAs), (2) Widmanstattn sideplates (WS), and (3) the intragranular phase (IP). These second phases are enriched in Fe and Mn contents.
2. The thermomechanical process of $Fe_{43.5}Mn_{34}Al_{15}Ni_{7.5}$ (at.%) polycrystals sheet can summary as follows: (1) hot-rolled (HR) at 1200°C to 4.2 mm in thickness, (2) annealing heat treatment (AHT) at 900°C for 1 hour in the fcc + bcc two-phases region, (3) cold-rolled (CR) to 1 mm in thickness with a reduction ratio of 76%, (4) cyclic heat treatment at 1200°C for 0.5 hours and followed by air cooling (AC) to room temperature for grain growth, (5) solution heat treated (SHT) at 1200°C for 1 hour and follow by quench into water to remove the fcc second phases, and (6) aging or precipitation heat treatment (PHT) at 200°C for 3 hours and quenching into water to obtain the superelastic properties.
3. The 3% superelastic strain is obtained in the tensile sample with the grain size around 5 mm in the gauge section of samples. The large grain size

decrease the critical stress and improve superelastic strain due to reduction of grain boundary constraints from surrounding grains during the superelastic test.

CHAPTER IX

FUTURE WORK

Future directions for the FeMnAlNi single crystals and polycrystals studies are suggested as follow:

9.1 Recommendations on FeMnAlNi Single Crystals Studies

9.1.1 Deformation Mechanism of Martensite in FeMnAlNi Single Crystals with the [100] Orientation under Tension

In the chapter 4, we characterize the superelastic response in the [100] orientation under both tension and compression. The high density of parallel dislocations generates at the austenite-martensite interface in the tensile sample; however, the austenite-martensite interface in the compression sample does not show high density of dislocations. We believe the formation of different types of twin planes in both tension and compression is contributed to the irrecoverable strain. In the future study, the microstructural characterization of martensite in different percent of tensile deformation is investigated by TEM. The tensile samples are deformed 8%, 16% and 24%. This study is to understand which martensite twin planes are contributed to the recoverable strain and which twin planes cause the irrecoverable strain. The similar concept can find in the NiTi study [149].

9.1.2 Martensite Variants Selection in FeMnAlNi Single Crystals with the [123] Orientation under Tension

From the effect of orientations on superelasticity results, the FeMnAlNi aged samples with the [123] orientation aged sample with the [123] orientation shows perfect recoverable strain. In contrast to [123] orientation, the poor recoverable strain is observed in the [100] orientation. We believe the reason might come from the numbers of martensite variant activation and formation of different twinning planes between [100] and [123] orientations. In the [123] orientation, we expect to observe the formation of multiple martensite variants in the tensile sample. Moreover, the formation of martensite plates between [100] and [123] orientations might have different twin planes. The twin planes are related to the recoverability. For the experiment work, the aged sample with the [123] orientation shows perfect recoverability and the volume fraction of martensite might not enough for the TEM investigation. The solution-treated sample will have more irrecoverable strain than it in aged sample. As a result, the sample is deformed 4 or 5% to obtain more martensite plates for the TEM investigation.

9.2 Recommendations on FeMnAlNi Polycrystals Studies

The superelastic properties can be drastically improved by controlling microstructural factors such as grain size and texture. Based on the previous polycrystalline study, the large grain size will decrease the grain constraint and improve the superelastic strain. However, there is no strong texture in the polycrystals samples based on the XRD results. As a result, the tensile sample shows only 3.5% superelastic

strain at room temperature. The development of the texture is other method for improving the superelastic strain. In the future study, we will investigate the effect of texture on superelasticity. The specimens will cut along the rolling directions (RD), 45◦ from RD and transverse direction to investigate the effect of texture (RD, TD, the angle of 45° from RD) on the superelastic properties at room temperature.

9.3 Recommendations on FeMnAlNi Polycrystals Wire Studies

9.3.1 Effect of Aging on Superelasticity

The first stage of this study is to obtain the large grain size in the texture wires by thermomechanical processing. The large grain size can increase the recoverable strain and reduce the critical stress for stress-induced martensitic transformation based on the previous polycrystals studies. The next stage is to investigate the effects of aging heat treatment at 200°C on the superelastic properties such as critical stress, stress-temperature phase diagram and recoverable strain under tension test at room temperature.

9.3.2 Cyclic Loading and Fatigue Life

The wires will subjected to cyclic tensile loading at room temperature with the strain amplitudes of 2 or 3% strain. This study will investigate the fatigue life and cyclic stability on the recoverability, stress hysteresis and critical stress.

REFERENCES

1 Maki T. In: Otsuka K, Wayman CM, editors. Shape Memory Materials. Cambridge: Cambridge University Press; 1998.

2 Ma J, Karaman I, Noebe RD. International Material Reviews 2010;55:257.

3 Miyazaki S, Otsuka K. Iron Steel Inst Jpn Int 1989;29:353.

4 Buehler WJ, Gilfrich JV, Wiley RC. Appl Phys1963;34:1475.

5 Kauffman G, Mayo I. Chem Educator 1997;2:1

6 Wu MH, Schetky LM. Industrial Applications for Shape Memory Alloys 2000:171

7 Zider RB, Krumme JF. Eyeglass Frame Including Shape Memory Elements In:US Patents 4772112. Menlo Park, California, USA: CVI/Beta Ventures, Inc.;1988.

8 Hautcoeur A, Eberthardt A. Eyeglass Frame with Very High Recoverable. Deformability. In: US Patents 5640217. Fergaflex, Inc., Montreal, Canada;1997.

9 Furuya Y. Design and Material Evaluation of Shape Memory Composites. Intell; Mater Syst Struct 1996;7:321.

10 Leo DJ, Weddle C, Naganathan G, Buckley SJ. Vehicular Applications of Smart Material Systems. 1998:106.

11 Stoeckel D. Shape Memory Actuators for Automotive Applications. Mater Des. 1990;11:302.

12 Bill C, Massey K, Abdullah EJ. Wing Morphing Control with Shape Memory Alloy Actuators. J Intell Mater Syst Struct 2013;24:879.

13 Hartl DJ, Lagoudas DC. Aerospace Applications of Shape Memory Alloys. Proc Leo DJ, Inst Mech Eng, Part G: J Aerospace Eng. 2007;221:535.

14 Humbeeck JV. Non-Medical Applications of Shape Memory Alloys. Mater Sci Eng, A 1999:134.

15 Schetky L. Shape Memory Alloy Applications In Space Systems Mater Des 1991;12:29.

16 Dunne DP, Wayman CM. Metall. Trans., 1973;4:137.

17 Oshima R. Scr. Metall., 1981;15:829.

18 Maki T, Kobayashi K, Minato M, Tamura I. Scr. Metall., 1984;18:1105.

19 Sato A, Chishima E, Soma K, Mori T. Acta Metall. 1982;30:1177.

20 Kajiwara S, Baruji A, Kikuchi T, Shinya N. Proc. SPIE. 2003;5053:250.

21 Baruji A, Kikuchi T, Kajiwara S, Shinya N. Material Science, Forum 2002;403:394.

22 Ando K, Omori T, Ohnuma I, Kainuma R, Ishida K. Applied Physics Letters 2009;95:212504.

23 Sehitoglu H, Efstathiou C, Maier HJ, Chumlyakov YI. Mech Mater 2006;38:538.

24 Tanaka Y, Himuro Y, Kainuma R, Sutou Y, Omori T, Ishida K. Science 2010;327:1488.

25 Omori T, Ando K, Okano M, Xu X, Tanaka Y, Ohnuma I, Kainuma R, Ishida K. Science 2011;333:68.

26 Otsuka K, Ren X. Progress in Materials Science 2005;50:511.

27 Hamilton RF, Sehitoglu H, Efstathiou C, Maier HJ, Chumlyakov Y. Acta Mater, 2006;54:587.

28 Gall K, Sehitoglu H, Chumlyakov Y, Kireeva I. Acta Mater. 1999;47:1203.

29 Gall K, Sehitoglu H, Chumlyakov Y, Zuev YL, Karaman I. Scripta Mater 1998;39:699.

30 Sehitoglu H, Karaman I, Zhang XY, Viswanath A, Chumlyakov YI, Maier HJ. Acta Mater, 2001;49: 3621.

31 Zhang J, Cai W, Ren X, Otsuka K, Asai M. Mater Trans 1999;40:1367.

32 Miyazaki S, Hmi YO, Otsuka K, Suzuki Y. J Phys 1982;43:C4-255.

33 Saburi T, Tatsumi T, Neno S, J Phys 1982;43:C4-261.

34 Kahlil-Allafi J, Dlouhy A, Eggler G. Acta Mater. 2002;50:4255.

35 Fan GL, Chen W, Yang S, Zhu JH, Ren XB, Otsuka K. Acta Mater. 2004;52:4351.

36 Michutta J, Somsen C, Yawny A, Dlouhy A, Eggler G. Acta Mater. 2006;54:3525.

37 Sehitoglu H, Efstathiou C, Maier HJ, Chumlyakov YI. Magn Mater 2005;292:89.

38 Sehitoglu H, Karaman I, Zhang XY, Chumlyakov YI, Maier HJ. Scripta Mater. 2001;44: 779

39 Ma J, Kockar B, Evirgen A, Karaman I, Luo ZP, Sehitoglu H, Efstathiou C, Maier HJ, Chumlyakov YI. Acta Mater 2012;60:2186.

40 Ma J, Hornbuckle BC, Karaman I, Thompson GB, Luo ZP, Chumlyakov YI. Acta Mater 2013;61:3445.

41 Gall K, Sehitoglu H, Maier HJ, Jacobus K. Metall. Mater. Trans 1998;29A:765.

42 Gall K, Sehitoglu H, Chumlyakov YI, Kireeva IV. Maier HJ. J. Eng. Mat. Tech. 1999;1A:121.

43 Gall K, Sehitoglu H, Chumlyakov YI, Kireeva IV, Maier HJ. J. Eng. Mat. Tech. 1999;1B:121.

44 Gall K, Sehitoglu H. International Journal of Plasticity 1999;15:69

45 Sehitoglu H, Jun J, Zhang X, Karaman I, Chumlyakov YI, Maier HJ, Gall K. Acta Mater 2001;49:3609.

46 Gall K, Sehitoglu, Chumlyakov YI, Kireeva IV. Acta Mater 1999;47:1203.

47 Panchenko EY, Chumlyakov YI, Kireeve IV, Ovsyannikov AV, Sehitoglu H, Karaman I, Maier HJ. The Physics of Metals and Metallography, 2008;6:577.

48 Saburi T, Yoshida M, Nenno S. Scr Matell 1984;50:363.

49 Ahadi A, Sun QP. Applied Physics Letters 2013;103:021902.

50 Ahadi A, Sun QP. Acta Mater. 2014;76:186.

51 Dvorak I, Hawbolt EB. Metall Trans 1975;6A:95

52 White SM, Cook JM, Stobbs WM. J De Phys 1982;C4:779

53 Sure GN, Brown LC. Metall Trans A 1984;15:1613

54 Kainuma R, Takahashi S, Ishida K. J Phys IV 1995;C8:961.

55 Kainuma R, Takahashi S, Ishida K. Metall Mater Trans A 1996;27:2187.

56 Sutou Y, Koeda N, Omori T, Kainuma R, Ishida K. Acta Materialia 2009;57:5759

57 Sutou Y, Omiri T, Kainuma R, Ishida K. Acta Materialia, 2013;61:3842.

58 Sutou Y, Omori T, Yamauchi K, Ono N, Kainuma R, Ishida K. Acta Mater. 2005;53:4121.

59 Ueland SM, Schuh CA. Acta Materialia 2012;60:282.

60 Omori T, Okano M, Kainuma R. APL Materials 2013;1;032103.

61 Kaufman L, Cohen M. Proy. Met. Phys., 1957;7:169.

62 Kurdjumov GV, Khandros LG. Dokl. Nauk SSSR. 1949;66:211.

63 Otsuka K, Shimizu K. Scr. Metall. 1970;4:467.

64 Kessler H, Pitsch W. Acta Metull., 1967;15: 401.

65 Gall K, Sehitoglu H. Intl J Plast 1999;15:69.

66 Niclaeys C, Ben Zineb T, Arbab-Chirani S, Patoor E. Intl J Plast 2002;18:1619.

67 Hamilton RF, Sehitoglu H, Efstathiou C, Maier HJ. Acta Mater, 2007;55:4867.

68 Patoor E, Eberhardt A, Berveiller M. Micromechanical Modelling of Superelasticity in Shape Memory Alloys. In: Pitman Research Notes in Mathematics Series, 1993;296:38.

69 Hamilton RF, Sehitoglu H, Chumlyakov YI, Maier HJ. Acta Mater, 2004;52:3383.

70 Funakubo H. Shape Memory Alloys, Amsterdam: Gordon & Breach Publishing Group 1987.

71 Wollants P, Bonte MD, Roos JR, Metallkd Z. Metall., 1979;70:113.

72 Maki T, Kobayashi K, Minato M, Tamura I. Scripta Metall., 1984;18:1105.

73 Zhu W, Liu EK, Feng L, Tang XD, Chen JL, Wu GH. Liu HY. Meng FB, Luo HZ. Appl Phys Lett., 2009;95:222512.

74 Chumlyakov YI, Kireeva I, Panchenko EY, Timofeeva EE, Kretinina I, Kuts O, Karaman I, Maier HJ. Adv. Mater. Res., 2014;1013:15–22.

75 Krooß P, Somsen C, Niendorf T, Schaper M, Karaman I, Chumlyakov YI, Eggeler G, Maier HJ. Acta Mater., 2014;79:126.

76 Krooß P, Holzweissig MJ, Niendorf T, Somsen C, Schaper M, Chumlyakov YI, Maier HJ. Scr. Mater., 2014;81:28.

77 Chumlyakov YI, Kireeva IV, Poklonov VV, Pobedennaya ZV, Karaman I. Tech. Phys. Lett.,2014; 40:747.

78 Chumlyakov YI, Kireeva IV, Kretinina IV, Keinikh KS, Kuts OA, Kirillov VA, Karaman I, Maier HJ. Russ. Phys. J., 2013;56:920.

79 Krooß P, Maier HJ, Karaman I, Chumlyakov YI, Niendorf T. Funct. Mater. Lett., 2012;05:1250045.

80 Evirgen A, Ma J, Karaman I, Luo ZP, Chumlyakov YI. Scr. Mater., 2012;67 : 475.

81 Kireeva I, Chumlyakov YI, Kirillov V, Kretinina I, Danil'son Y, Karaman I, Cesari E. Russ. Phys. J., 2011;53:1103.

82 Kireeva I, Chumlyakov YI, Kirillov V, Karaman I, Cesari E. Tech. Phys. Lett., 2011;37:487.

83 Chumlyakov YI, Kireeva IV, Poklonov VV, Pobedennaya ZV, Karaman I. Technical Physics Letters, 2014;40:747.

84 Tseng LW, Ma J, Karaman I, Wang SJ, Chumlyakov YI. Scripta Materialia 2015;101:1.

85 Tanaka T, Abe S, Sutou Y, Omori T, Ishida K, Kainuma R. Abstract of 2010 spring meeting of the Japan Institute of Metals in Tokyo.

86 Turabi A, Karaca H, Tobe H, Li P, Basaran B, Chumlyakov YI. Abstract of TMS 2013 Annual Meeting & Exhibition.

87 Geng Y, Lee D, Xu X, Makoto N, Jin X, Omori T, Kainuma R. Alloys and Compounds 2015;628:287.

88 Omori T, Abe S, Tanaka Y, Lee DY, Ishida K, Kainuma K. Scripta Materialia 2013;69:812.

89 Lee D, Omori T, Kainuma R. Alloys and Compounds 2014;120:617.

90 Hornbogen E, Mayer WM. Acta Metall. 1967;15:584.

91 Hornbogen E, Mayer WM. Z. Metallk. 1967;58:967.

92 Maki T, Kobayashi K, Tamura IJ. De Phys. 1982;C4:541.

93 Kokorin VV, Gunko LP, Shevchenko OM. Scripta Mater., 1993;38:35.

94 Gaunt P, Christian JW. Acta Metall., 1959;7:559.

95 Jost N, Escher K, Donner P, Sade M, Halter K, Hornbogen E. 1990;6:639.

96 Jost N. Metall. 1990;44:17.

97 Kloss HZ. Metal., 1996;3:175.

98 Ran Q. A Comprehensive Compendium of Evaluated Constitutional Data and Phase Diagrams, 1992;5:250.

99 Liu XJ, Hao SM. Scripta Metall. Mater., 1993;28:611.

100 Liu XJ, Hao SM. CALPHAD, 1993;17:79.

101 Liu XJ, Hao SM, Xu LY, Guo YF, Chen H. Metall. Mater. Trans. A, 1996;27A: 2429.

102 Umino R, Liu XJ, Sutou Y, Wang CP, Ohnuma I, Kainuma R, Ishida K. Journal of Phase Equilibria and Diffusion 2006;27:54.

103 Zhang YT, Li XY, Li DZ, Li YY. AIP Conference Proceedings 2008;986: 132.

104 Hwang KH, Wan CM, Byrne JG. Scr. Metall. Mater. 1990;24:979.

105 Hwang KH, Wan CM, Byrne JG. Mater. Sci. Eng. A 1991;132:161.

106 Hwang KH, Chen SK, Yang WS, Wu TB, Wan CM, Byrne JG, Scripta Metallurgical 1990:24:495.

107 Cheng WC, Liu CF, Lai YF. Scr. Mater. 2003;48:295.

108 Cheng WC. Metallurgical and Materials Transactions A. 2005;36A:1737.

109 Omori T. Nagasako M, Okano M, Endo K, Kainuma R. Appl Phys Lett., 2012;101:231907.

110 Gall K, Sehitoglu H, Chumlyakov YI. Kireeva IV. Acta Materialia, 1999;47:1203.

111 Nishiyama Z. Martensitic transformation, Materail Science Series 1978;6:338.

112 Saburi I, Nenno S. Proc Int Conf Solid-Solid Phase Transf. Pittsburg; 1981:1455.

113 Baker I, Wu H, Wu X, Miller MK, Munroe PR. Materials Characterization 2011;62:952.

114 Baker I, Zheng RK, Saxey DW, Kuwano S, Wittmann MW, Loudis JA, Prasad KS, Liu Z, Marceau R, Munroe PR, Ringer SP. Intermetallics 2009;17:886.

115 Thompson K, Lawrence D, Larson DJ, Olson JD, Kelly TF, Gorman B. Ultramicroscopy 2007;107:131.

116 Giannuzzi LA. Microsc Microanal 2006;12:1260.

117 Hellman OC, Vandenbroucke JA, Rusing J, Isheim D, Seidman DN. Microsc Microanal 2000;6:437.

118 Dadda J, Maier HJ, Karaman I, Karaca HE, Chumlyakov YI. Scripta Materialia, 2006;55:663

119 Picornell C, Pons J, Cesari E. Acta Materialia, 2001;49:4221.

120 Karaca HE, Karaman I, Brewer A, Basaran B, Chumlyakov YI, Maier HJ. Scripta Materialia, 2008;58:815.

121 Sehitoglu H, Karaman I, Anderson R, Zhang X, Gall K, Maier HJ, Chumlyakov YI. Acta Materialia, 2000;48:3311.

122 Hamilton RF, Sehitoglu H, Efstathiou C, Maier HJ, Chumlyakov YI. Acta Materialia, 2006;54:587.

123 Kajiwara S. Materials Science and Engineering A, 1999;273: 67.

124 Kikuchi T, Kajiwara S. Materials Transactions, JIM, 1993;34: 907.

125 Kajiwara S, Owen WS. Scripta Metall. 1977;11:137.

126 Salje EKH, Zhang H, Idrissi H, Schryvers D, Carpenter MA, Moya X, Planes A. Physical Review 2009;B80:134114.

127 Muller I, Xu H. Acta metal. Mater. 1991;39:263.

128 Blavette D, Caron P, Khan T. In: Reichman S, Duhl DN, Maurer G, Antolovich S, Lund C, editors. Superalloys 1988. Warrendale, PA: The Mineral, Metals and Materials Society; 1988.

129 Maki T, Wayman CM. Acta Metall. 1977;25:695.

130 Hornbogen E. Acta Metall 1985;33:595.

131 Bhattacharya K. Microstructure of Martensite: Why It Forms and How It Gives Rise to the Shape-Memory Effects, 1st ed., Oxford University Press, New York, NY, 2003;29:141809.

132 Ball JM, James RD. Arch Rat Mech Anal 1987;100:13.

133 James RD, Hane KF. Acta Mater 2000;48:197.

134 Ball JM, James RD. Arch. Rat. Mech. Anal. 1987:100:13.

135 James RD, Hane KF. Acta Mater. 2000:48:197.

136 Ball JM. Materials Science & Engineering A 2004;378:61.

137 Sehitoglu H, Karaman I, Anderson R, Zhang X, Gall K, Maier HJ, Chumlyakov YI. Acta Mater. 2000;48:3311.

138 Zhang XY, Brinson LC, Sun QP. Smart Mater. Struct., 2000;9:571961.

139 Shaw JA, Kyriakides S. J. Mech. Phys. Solid., 1995;43:1243.

140 Chakravorty S, Wayman CM. Metall. Trans. A, 1976;7:569.

141 Karaca HE, Karaman I, Chumlyakov YI, Lagoudas DC, Zhang X. Scripta Mater. 2004;51:261.

142 Dadda J, Maier HJ, Niklasch D, Karaman I, Karaca HE, Chumlyaknov YI. The Minerals, Metal & Materials Society and ASM international 2008;39A:2026.

143 Gall K, Sehitoglu H, Chumlyakov YI. Kireeva IV. Maier HJ, Transaction of The ASME 1999;28:121.

144 Omori T, Kusama T, Kawata S, Sutou Y, Ohnuma I, Sutou Y, Araki Y, Ishida K, Kainuma R. Science 2013;27:1500.

145 Ciulik J, Taleff EM. Scripta Metall. 2009;61: 895.

146 Taylor GI. J. Inst. Met. 1938;62:307.

147 Kocks UF. Metall Trans 1970;1:1121.

148 Sachs GZ. Ver. Dtsch. Ing. 1928;72:734.

149 Zhang JX, Sato M, Ishida A. Acta Mater. 2006;54:1185.

APPENDIX A

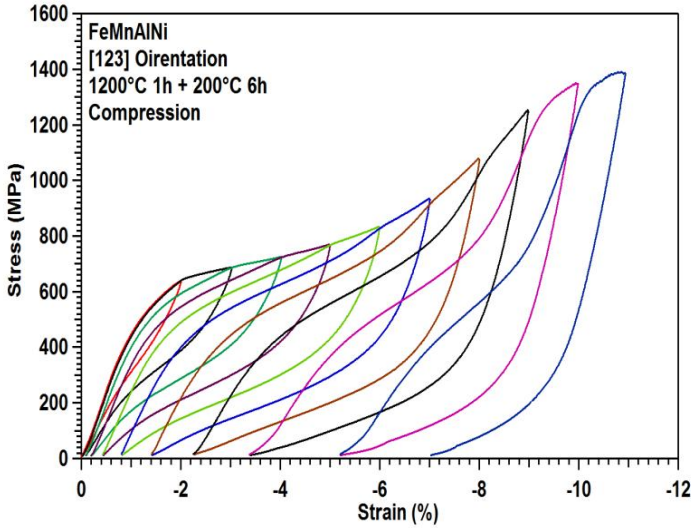

Figure A.1 Incremental strain superelastic test in $Fe_{43.5}Mn_{34}Al_{15}Ni_{7.5}$ [123] single crystal specimens solution heat treated at 1200°C for 1 hour and aged at 200°C for 6h under (a) compression. The experiments were conducted at room temperature.

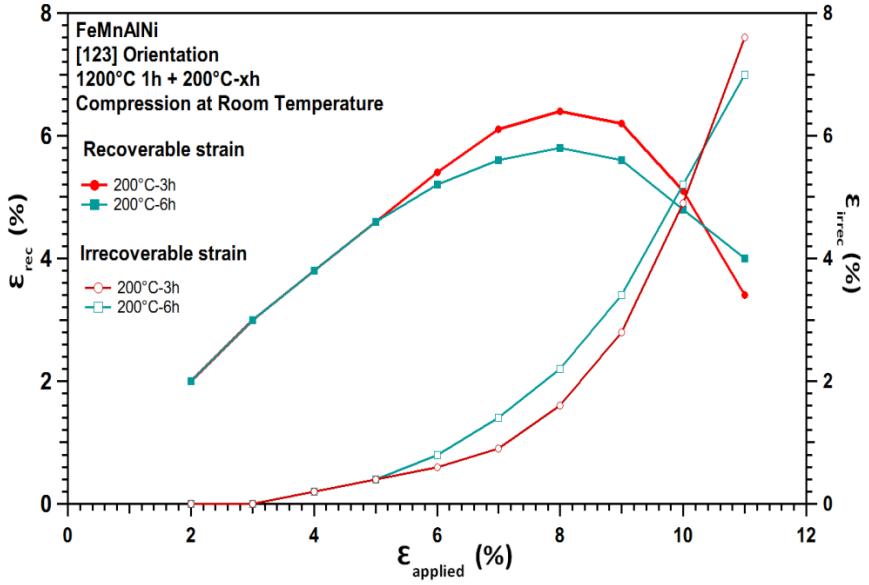

Figure A.2 Recoverable strain and irrecoverable strain as a function of applied strain in the $Fe_{43.5}Mn_{34}Al_{15}Ni_{7.5}$ single crystals with the [123] orientations aged at 200°C for 3 and 6 hours under compression test at room temperature.

APPENDIX B

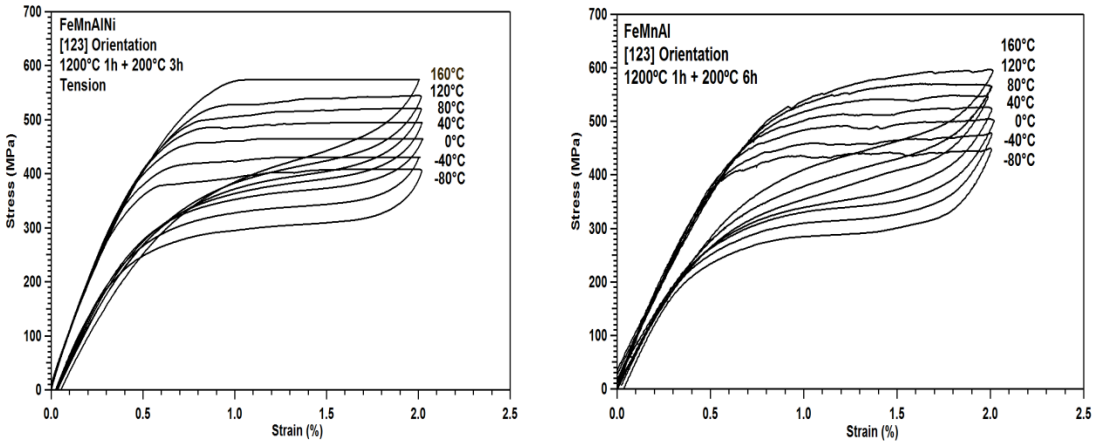

(a) (b)

Figure B.1 Constant tensile strain test at different temperatures in the $Fe_{43.5}Mn_{34}Al_{15}Ni_{7.5}$ single crystals oriented in [123] direction aged at 200°C (a) 3 hours and (b) 6 hours.

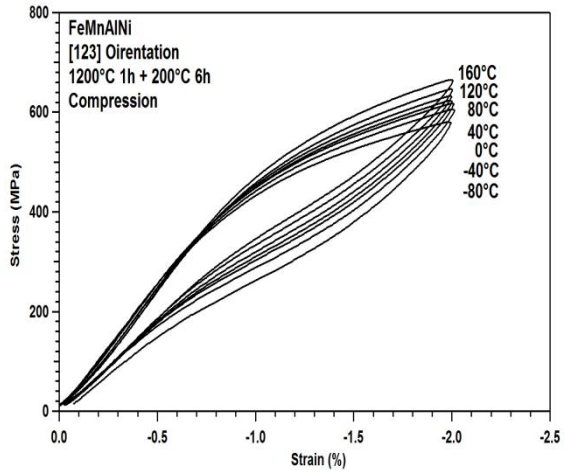

Figure B.2 Constant compressive strain test at different temperatures in the $Fe_{43.5}Mn_{34}Al_{15}Ni_{7.5}$ single crystals oriented in [123] direction aged at 200°C for 6hours.

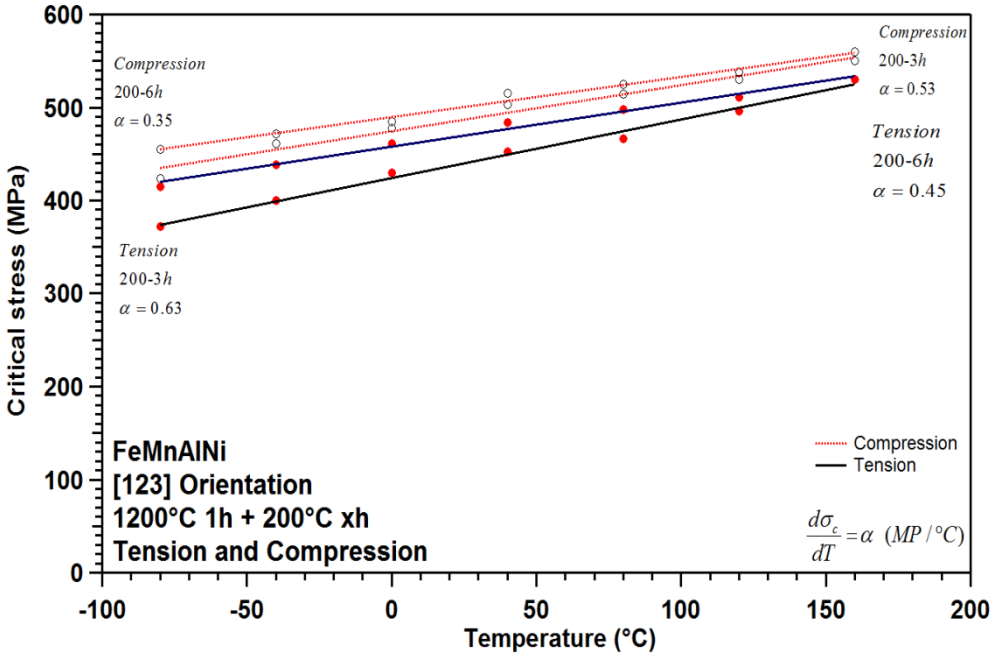

Figure B.3 Stress-temperature phase diagram in the $Fe_{43.5}Mn_{34}Al_{15}Ni_{7.5}$ single crystals with the [123] direction in different aging conditions under tension and compression.

APPENDIX C

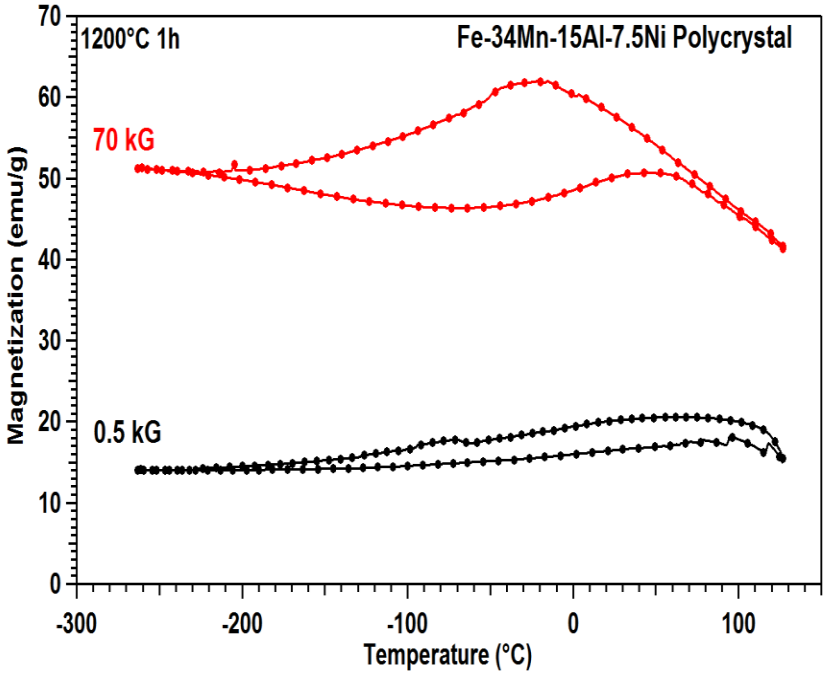

Figure C.1 Thermomagnetization of FeMnAlNi alloy solution heat treatment at 1200°C for 1 hour.